UNIVERSITÀ
DEGLI STUDI
DI PADOVA

UNIVERSITA’ DEGLI STUDI DI PADOVA
Dipartimento di Ingegneria Industriale DII

Dipartimento di ingegneria industriale
Corso di Laurea Magistrale in Ingegneria Aerospaziale
Curriculum Aeronautico

White mica as filler for nanocomposites

Relatore
Roberta Bertani

Nicholas Berton 1242568

Anno Accademico 2021/2022

Ringraziamenti

A conclusione di questa mia tesi, vorrei ringraziare tutte le persone che mi sono state vicine in questi anni difficili e questo lungo percorso che finalmente giunge al termine anche grazie al fatto di non essere mai stato solo.

Per primi i miei genitori Greta e Remo, che mi hanno sempre assecondato fidandosi delle mie scelte e che sono sempre stati pronti a darmi consiglio nel momento del bisogno.

Ringrazio tutti gli altri componenti della mia famiglia, di cui sono orgoglioso di far parte. Cito i nonni Ada, Gildo e Ivana, le zie Serena e Silvia e i cugini Giada, Matilde e Mattia, ma la lista sarebbe ben più lunga.

Un grosso ringraziamento va alla mia ragazza Sara che mi ha aiutato a rialzarmi nei momenti più bui e che ha reso più belle le vittorie più importanti, condividendo con me questo difficile percorso, sopportandoci l'un l'altro.

Ringrazio inoltre anche la sua famiglia, che per me in questi anni è stata come una seconda casa.

Ringrazio tutti i miei amici, che mi hanno sempre supportato e con cui ho condiviso mille e più avventure.

Ringrazio la prof. Bertani che mi ha permesso di vivere un'esperienza fantastica, da cui ho appreso molto. La ringrazio inoltre ancora per la sua pazienza e la sua disponibilità che non è mai mancata.

Ringrazio Greta, che mi ha aiutato moltissimo con questa tesi, fornendomi un aiuto essenziale per affrontare l'analisi dei dati raccolti dalle prove.

Un particolare ringraziamento è dovuto anche al prof. Naletto, con cui ho affrontato l'ultimo esame di questo percorso.

Con queste ultime righe, inoltre, vorrei dedicare questa tesi a mia nonna Ivana, che in questo momento sta combattendo una battaglia importante, forza nonna!

Index

Figure's index

Table's index

LO SCOPO DELLA TESI

Lo scopo di questa tesi è di produrre e analizzare le proprietà di alcuni campioni di materiale nanocomposito, costituito da una matrice epossidica caricata con una particolare mica. Verranno prodotti 5 set di campioni, 3 con mica 10 e 2 con mica 45, con diverse cariche di filler (1,3,5% e 1,5%) e per ogni set saranno prodotti campioni di 2 diversi formati (tensile e CT). Sottoporremo poi i campioni a test meccanici per studiarne diverse proprietà, in particolare il modulo elastico e la resistenza a trazione per il test di trazione e i parametri K_{Ic} e G_0 per il test di frattura, verificando quale sia l'effetto su queste proprietà di diverse cariche e dimensioni di filler. Inoltre, attraverso analisi con diverse tecniche microscopiche verificheremo lo stato di esfoliazione e dispersione della mica nella matrice.

ABSTRACT

In this work we study the behavior of two types of micas, when employed in nanocomposites The minerals were given to the University of Padova by Veneta Mineraria, a mining company headquartered here, in the province of Padua. As matrix we use a commercial epoxy resin (two-part), used in the automotive industry, for example by Automobili Lamborghini in various elements of their cars. There is not a lot of literature on these particular materials and that's why we decided to study them. We expect that the presence of micas platelet, if correctly dispersed (we will investigate later this topic) will increase the mechanical properties taken into account, such as the elastic modulus, the tensile strength and the fracture toughness. In the end we present some actual and future application of this nanocomposite in different fields, such as the automotive and the biomedical.

SOMMARIO

In questa tesi studiamo il comportamento di alcune miche quando usate come filler in un materiale composito. I minerali sono stati donati all'Università di Padova da Veneta Mineraria, una società di estrazione mineraria con sede nella provincia di Padova. La matrice del composito è costituita da una resina epossidica commerciale bicomponente, utilizzata comunemente nel settore automotive, ad esempio da Automobili Lamborghini, in varie parti delle sue vetture. Non c'è molta bibliografia su questi particolari minerali e proprio per questo abbiamo scelto di studiarli. Ci aspettiamo che la presenza della mica, se correttamente dispersa nella matrice (aspetto che approfondiamo nella trattazione), migliorerà le proprietà meccaniche studiate, ovvero il modulo elastico, la resistenza alla trazione e la resistenza alla frattura. In fine sono presentate alcune applicazioni, attuali e future di questi nanocompositi in diversi settori, come ad esempio l'automotive e il biomedico.

CHAPTER 1

Introduction

1.1 Nanocomposites

From the dawn of the composite materials era, a constant improvement in materials technologies led to the development of many new materials with better and better properties, with the possibility to create components with unique and ultra-specialized characteristics. Composite materials get born from the fusion of two, or more, different standard materials, maintaining the distinction of phases but exhibiting the synergy of one, with properties generally better than the originals. Usually, a composite is mainly formed by two phases: the reinforcement and the matrix. The reinforcement is the material that simply sustain most of the load conferring stiffness to the composite, while the matrix has many different tasks: to transfer the load to the reinforcement, to keep the reinforcement together and protecting them from the environment. By the way we must take into account the presence of other phases: the interphase that is the region that connect the matrix and reinforcement, and that could be physically and chemically different from the original composites' constitutive materials, and the voids, typically the main "imperfection factor" of these materials.

In a nanocomposite the reinforcement is usually called filler and one or more of these nano-reinforcements are introduced into the matrix to enhance not only its mechanical properties but more commonly various other characteristics such as thermal, tribological, optical, electrical properties and so on. The filler is typically in the form of particulate, flakes or micro-fibers with 1, 2 or 3 dimensions in the micro or nano scale. A nanocomposite typically consists of a single nanoscale filler while, on the other hand, if it contains more than one is called hybrid nanocomposite.

The field of nanotechnology is one of the most popular areas for current research and development, in virtually all technical disciplines. To be fair nanotechnology is not new to polymer science as many studies before the era of nanotechnology concerned the implementation of objects in the nanoscale, but until recently, they were not specifically referred to as nanotechnology.

1.2 Matrixes

It is necessary to go a little more into details talking about composite's constituents starting with the matrix. In this discussion we'll be focusing on epoxies, which are the matrix we will utilize in our experiment as well as they are among the most common material used in this application. Epoxy resins are a class of thermosetting polymers generally known as the most performant resins on the market. These materials can provide different properties to our artifact and find wide use in various manufacturing areas such as coatings, adhesives, and many other extremely various applications. Once cured, they are resistant to chemical attacks and they resist to corrosion, as well as they guarantee amazing mechanical and thermal properties, in comparison with other resins. On the other hand, epoxy resins, once cured, are quite brittle and have poor crack and impact strength in addition to a low fracture toughness. Many attempts have been made to improve their weakness, but by now none has been completely successful despite a few improvements. Epoxy resins have a glassy behavior at room temperature and so diluents are usually needed to permit the optimal impregnation of reinforcements. The viscosity of an epoxy resin without diluent can vary a lot, and that's why these commercial resins are commonly in the form of di-epoxide, namely molecules consisting of a linear CH chain with the epoxy groups collocated at the end that permit the bonding during polymerization. The presence of annular complexes can enhance the mechanical and thermal stress resistance of the resin.

The resin employed in the experiment is the Elantas Elan-Tech® EC157 (component A) with the hardener Elantas Elan-Tech® W 152 LR slow (component B).

1.3 Nano-Reinforcements

Nowadays several types of reinforcements are used in composites, differentiate by material, shape and dimension. Mineral clays are for sure one of the most attractive nano-reinforcement. Consisting of characteristic silicates layers, they perfectly combine the properties of both polymers and silicates. Polymer-clay nanocomposites showed excellent mechanical, fire retardant, diffusional barrier and ultraviolet light resistance properties with reference to the normal resin or with other more common composite material.

The main difference between the properties of conventional and nano composites is caused by clay platelet's exceptionally extended contact area. The observed improvement in quite every aspect of clay-polymer nanocomposite characteristics, has made them a promising candidate for various applications from commercial to super-niche fields. A major advantage of nanocomposite over the conventional consist in the amount of reinforcement necessary to see a significant increment of the material properties, that in the standard composites is always comparable with the volume fraction of the matrix, while with nanocomposite we can obtain, a significant growth of mechanical properties by adding a very small amount of nanoclay to the matrix, in the order of 1-3% of the total weight of the finite material. Toyota research group, in a pioneering project made possible to doubling the tensile modulus by in-situ polymerization of a little more than the 4% in weight of nano clay filler into nylon.

As we did for the matrix, we must focus a little bit more on the reinforcement we will use in this study, so it has to be clear to us what clays are. Is defined clay a class of material containing layered silicates incorporating various materials, like metal oxides and organic matter. Clays derive from the erosion of feldspar rocks over time, and so they generally contain varying amounts of iron, magnesium, alkali metals, alkaline earths and other cations. Clays are classified in many classes differentiate based on their chemical composition and crystalline structure. Natural clays are also simplistically divided into three groups in terms of ratios of alternating tetrahedral SiO_2 and octahedral sheets. We have Kaolinite (1:1 Ratio), Montmorillonite and Vermiculite (2:1 Ratio) and Chlorite (2:2 Ratio).

The Montmorillonite crystal structure is one of the most interesting and consequently more studied clay for nanocomposite application. It is composed of an octahedral allumina sheet situated between two tetrahedral silica sheets wherein the oxygen cations are in common between the octahedral sheet and the tetrahedral sheet. Montmorillonite is widely used in materials applications because of its high aspect ratio and high swelling property. The sheets of this material are commonly known as T-O-T sheets and the chemical formulation is expressed as $(Na,Ca)_{0.33}(Al,Mg)_2Si_4O_{10}(OH)_2.nH2O$. These layers complexes could have an aspect ratio from 100 to 1000 and a thickness in the order of some nanometers. These platelets are stacked in parallel, by Van Der Waals and weak electrostatic interactions and the gap between two sheets is called “Gallery” or simply “Interlayer”. In nanoclay, negative charges are naturally induced because of the naturally ionic substitution of some elements within the various layers, for example Al with Mg. These charges are neutralized by the cations present between layers, usually H, Na, K, Mg or Ca.

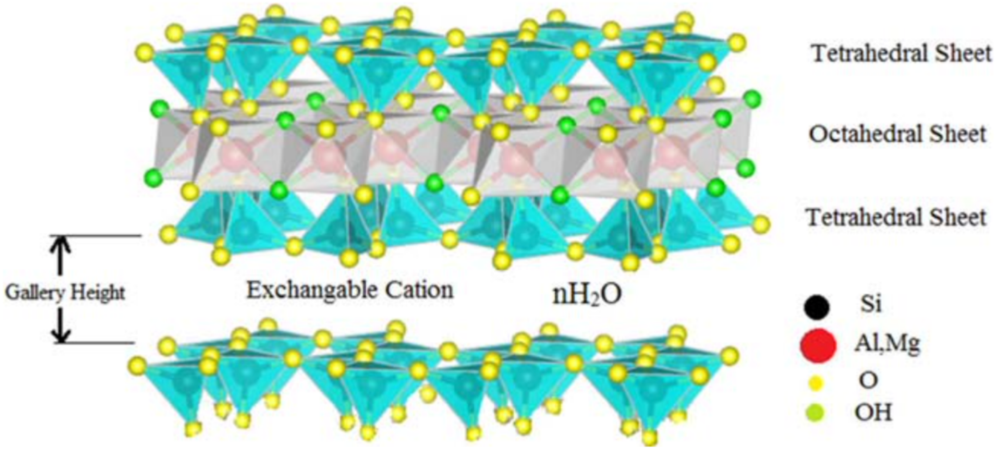

Figure 1 Characteristic tetrahedral and octahedral structures in nanoclays' sheets.

When we try to combine different materials, one of the key aspects is the affinity among the materials and how we put them together. Nanoclays can be incorporated into the matrix by several techniques, the most common are the in-situ polymerization, the solution method, the Sol-Gel templating and the melt mixing. The solution method utilizes a solvent in which the polymer is soluble. Once the nanoclay plates are exposed to the solution, the silicate layers are naturally separated enough for the mixture to penetrate into the galleries. The solution infiltrating can separate the plates more and more and eventually separate them completely. When the silicate layers are dispersed in the emulsion the solvent is left to evaporate. Then the polymerization starts by heating. In the Sol-Gel templating technique, the clay nanofiller is mixed in a solution containing polymer and silicate building blocks. In the process, polymers promote the nucleation of the Gel and so they get trapped in the nanoclay interlayer. Nanoclays can be also directly added in the melted polymers, without the aid of a solvent.

In the case the polymer is compatible (or better quasi-compatible) with the clay platelets surface, there is no need of performing complicated process and it will naturally penetrate in the nanoclay galleries. This is obviously the easiest method which also offers the highest production rate with the least costs, so it's the one we will follow in our study. It is easy to figure out that the dispersion of the filler in the matrix is a key aspect of these nanocomposites and so it's important to introduce a parameter that tell us about how good the dispersion process was: the degree of dispersion of the clay platelets into the polymer matrix. A low degree of the nanoclay dispersion in the polymers will lead to the aggregation of the platelets, forming structures similar to those present in conventional composites and preventing to the composite to benefit of the clay's presence.

Achieving a good dispersion is not a trivial task, since quite every nanoclay is incompatible with polymers since clays are generally hydrophilic while polymers are hydrophobic. There are some techniques with which we can alter the clay's behavior, improving affinity between the two materials. Some methods are based on physical absorption which, without altering the structure of nanoclay, permit to enhance chemical affinity. In the other hand between the absorbed molecules and the clay the attraction forces are very weak. With the chemical modifications of clays instead, we can obtain quite strong interaction forces.

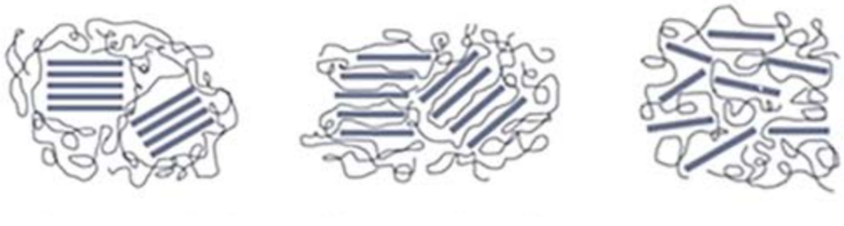

Figure 2 The three morphologies of nanoclay fillers, aggregated on the left, intercalated in the center and exfoliated on the right

Depending on the degree of dispersion, it is possible to recognize three different morphologies of dispersed nanoclays: Aggregated, Intercalated, and Exfoliated. The morphologies of nanoclay are influenced by various aspects such as the processing method, material, possible clay modification, chemical composition of the matrix, weight fraction of the constituent and the affinity between them. In standard particulate composites, clays are in the **aggregate** status, so they are stacked in plies parallel to each other without the intercalation of the polymer matrix into the galleries. In this state the material is not considered a nanocomposite because of the micro or bigger size scale of the aggregation of platelets, and never permitting to reach the full potential properties of the material. Even with a single polymer chain penetrated through the silicate layers, we can talk about an **intercalated** morphology, which involves the presence of interaction between clay and polymer. This leads to the creation of a new phase, in the nanoscale size, called interphase. Altering the spacing between the nanolayers not only can bring to a change of the clay's affinity with water, becoming hydrophobic, but also could improve the platelets dispersion in the polymer. The most performing, so the most interesting morphology, is the completely **exfoliated**, in which the plies of the stacking have been utterly separated, so we can reach the highest possible dispersion degree. The better mechanical performance, reached in this case are caused by the remarkable aspect ratios of the filler particles involving the maximum interaction possible among the two phases.

The development of nanocomposite needs a correct understanding of the mechanical behavior and of the properties, of the nanoclay filler. Most of the studies have focused on the manufacturing process and the characterizations of this nanomaterials, while not a lot of importance has been given to the development of models and consequential predictive methods and tools, able to simulate their mechanical properties. The creation of a reliable simulation technique of this nanomaterials is a crucial aspect to realize their potential applications. To be able to predict nanoclay reinforced polymers mechanical properties, it is necessary extracting the mechanical properties of isolated nanoclays. Gaining the access to a lone nanoplate, without utilizing an intermediate between clay and polymer is next to impossible, because of its size. Several experiments were made to obtain an estimation of the aggregated nanoclay mechanical properties. These techniques included compressibility, optical, acoustic and ultrasonic measurement and inelastic neutron scattering. An oversimplified approach would be the one to consider the properties of the single plate equal to the property measured in the aggregation (K.S. Alexandrov, 1961). The mechanical properties of these nanocomposites, instead, can be indirectly obtained by simple traction tests. Knowing the pure resin property, we can archive nanoplates property applying micromechanics laws (Z. Wang, 2001).

Table 1 Estimation of clay's elastic modulus

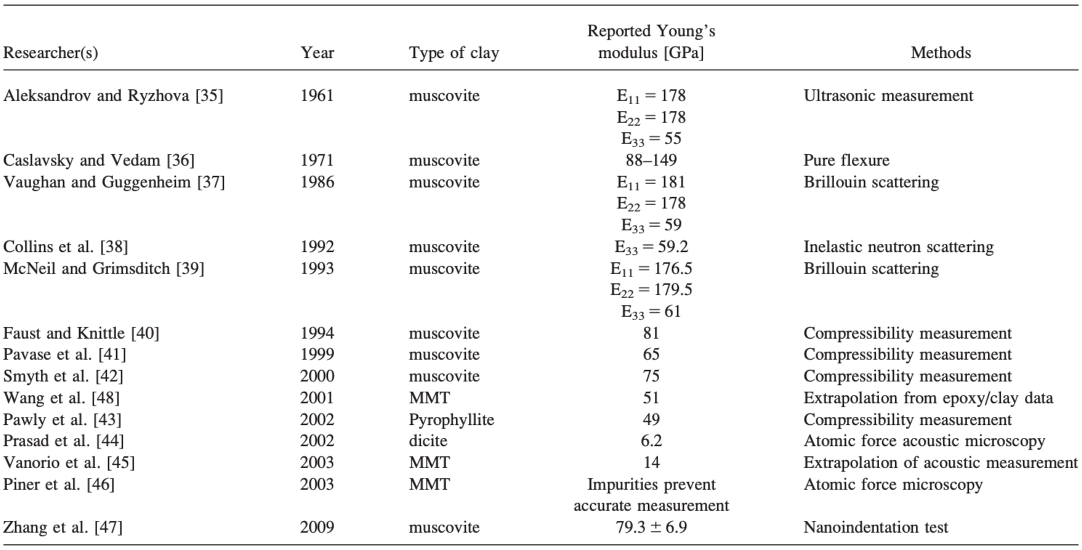

Researcher(s)	Year	Type of clay	Reported Young's modulus [GPa]	Methods
Aleksandrov and Ryzhova [35]	1961	muscovite	$E_{11} = 178$ $E_{22} = 178$ $E_{33} = 55$	Ultrasonic measurement
Caslavsky and Vedam [36]	1971	muscovite	88–149	Pure flexure
Vaughan and Guggenheim [37]	1986	muscovite	$E_{11} = 181$ $E_{22} = 178$ $E_{33} = 59$	Brillouin scattering
Collins et al. [38]	1992	muscovite	$E_{33} = 59.2$	Inelastic neutron scattering
McNeil and Grimsditch [39]	1993	muscovite	$E_{11} = 176.5$ $E_{22} = 179.5$ $E_{33} = 61$	Brillouin scattering
Faust and Knittle [40]	1994	muscovite	81	Compressibility measurement
Pavase et al. [41]	1999	muscovite	65	Compressibility measurement
Smyth et al. [42]	2000	muscovite	75	Compressibility measurement
Wang et al. [48]	2001	MMT	51	Extrapolation from epoxy/clay data
Pawly et al. [43]	2002	Pyrophyllite	49	Compressibility measurement
Prasad et al. [44]	2002	dicite	6.2	Atomic force acoustic microscopy
Vanorio et al. [45]	2003	MMT	14	Extrapolation of acoustic measurement
Piner et al. [46]	2003	MMT	Impurities prevent accurate measurement	Atomic force microscopy
Zhang et al. [47]	2009	muscovite	79.3 ± 6.9	Nanoindentation test

In the Table 1 above we can look at the value of the young modulus in the three (principal) direction 11, 22 and 33, in different minerals. The huge values difference among different direction of for the same material is mainly due to the direction of the galleries.

The inability to carry out direct trials on a single clay platelet, the behavior difference among the various clays morphologies, the not so reliable results acquired from the indirect tests, compared with scattered data obtained through experimental observations combined with the prohibitive costs of conducting experiments of object in the nanoscale are all aspects that suggested the development of computational modeling for the study of these nanomaterials. Nowadays the mechanical properties of the platelet nanostructure can be described through the use of different computational techniques, The main method are the atomistic modeling techniques, such as Molecular dynamics simulation and the Monte-Carlo technique or other methods that instead of relying on Newton's second law are based on the Schrodinger equation, for example the ab initio approach. Among the different techniques molecular dynamic simulations is the easiest to perform and the one which can provide a wider insight analysis to the behavior of nanomaterials. Almost all the studies made with molecular dynamic simulation permitted to interact with the system for a finite period, simulating the movements of the various atoms and molecules while analyzing the dynamic evolution of the interacting particles. To each atom is assigned a force field and the forces on the atoms are differentiated by the potential interatomic functions. The former method has been used successfully to simulate single platelets and platelets with water/cation interlayers (R.T. Cygan, 2004). An overview of the conducted simulations with this technique aiding to calculate nanoclay's elastic properties is shown in the following table 2.

Table 2 Estimation of clay's Young modulus through simulations.

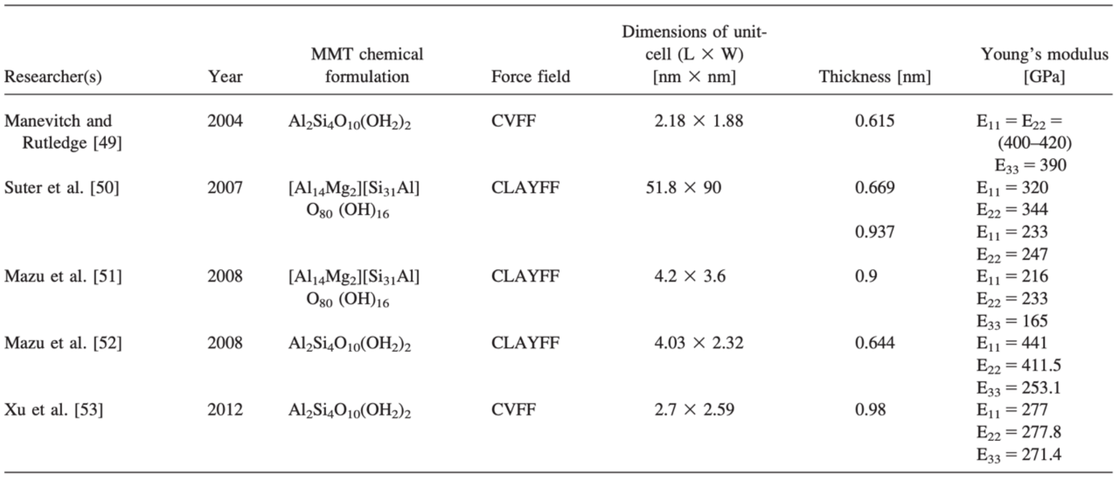

Researcher(s)	Year	MMT chemical formulation	Force field	Dimensions of unit-cell (L × W) [nm × nm]	Thickness [nm]	Young's modulus [GPa]
Manevitch and Rutledge [49]	2004	$Al_2Si_4O_{10}(OH_2)_2$	CVFF	2.18 × 1.88	0.615	$E_{11} = E_{22} =$ (400–420) $E_{33} = 390$
Suter et al. [50]	2007	$[Al_{14}Mg_2][Si_{31}Al]O_{80}(OH)_{16}$	CLAYFF	51.8 × 90	0.669	$E_{11} = 320$ $E_{22} = 344$
					0.937	$E_{11} = 233$ $E_{22} = 247$
Mazu et al. [51]	2008	$[Al_{14}Mg_2][Si_{31}Al]O_{80}(OH)_{16}$	CLAYFF	4.2 × 3.6	0.9	$E_{11} = 216$ $E_{22} = 233$ $E_{33} = 165$
Mazu et al. [52]	2008	$Al_2Si_4O_{10}(OH_2)_2$	CLAYFF	4.03 × 2.32	0.644	$E_{11} = 441$ $E_{22} = 411.5$ $E_{33} = 253.1$
Xu et al. [53]	2012	$Al_2Si_4O_{10}(OH_2)_2$	CVFF	2.7 × 2.59	0.98	$E_{11} = 277$ $E_{22} = 277.8$ $E_{33} = 271.4$

Beside to the chemical compositions, the differences in the predicted clay modulus through these simulations is mainly due to the dimensions of unit-cell used in the simulation. To give a numerical example of the elastic modulus obtained, Chen and Evans, relying on the reported values in literature for layered clay minerals proposed that the young's modulus of nanoclays platelets is in the range of 178–265 GPa, (B. Chen, 2004). It's to be taken into account that an atomistic modelling process became more and more complicated as the number of simulated atoms increase and because of that the analysis of big atomics systems involves the restriction of the process to very short time and small spatial scales. Another complication derives from the reliance of nanoplates young's modulus to their dimension, as it happens for carbon nanotube, a common aspect for object at nanoscale.

Alternatively, to MD simulations, we can use continuum-based techniques in which interactions between atoms are virtually substituted by a continuum bar or other elements based on the number of degrees of freedom we want to leave to the system. This method has been successfully used in the study of carbon nanotubes. The beneficial features of these techniques are mainly the much faster runtime and the absence of restrictive spatial limitations. Unlike with nanotubes, where these continuum-based techniques are used often (R. Rafiee, 2014), by now no one has really attempted to completely model nanoclay platelets as a continuum frame structure yet. With these methods in addition to the possibility to take in consideration the nanoclay typical lattice structure, we could utilize finite element modeling to perform analysis on different mechanical aspects. Molecular dynamic simulations are really time consuming, so the totality of the studies on nanoclay-polymer composites were only limited to calculate few mechanical properties. Is important to observe that in all these processes, the interphase has never been taken in consideration. It is known that like in most of the composite materials, and especially in the nanocomposite, such as CNT, the properties of the polymer penetrated into the interlayer, are different from the neat polymer (P.A. Tzika, 2000). The few studies that minded this aspect modeled this intermediate phase with finite element techniques as a continuum (M. Uhrig, 2015) but the real thickness and the properties of this small spatial region are still unknown. Secondly, the random dispersion of the filler and the possibility of secondary aggregation necessitate the implementation of stochastic FEM instead of deterministic approaches.

In addition to that, it is crucial to also determine the influence of the combination of different amount of the various filler's morphology. All three nanoclay's morphologies can be found in polymer matrix. Beyond the coexistence of all aggregated, intercalated and exfoliated particles, is also to be taken into consideration that the number of layers exfoliated from a singular aggregation may be very different region by regions, due to undetectable phenomena. Most of the studies on these materials assumed the presence of a single morphology (K. Hbaieb, 2007) while few studies considered the coexistence of intercalated and fully exfoliated clay platelets (A. Mesbah, 2009). In practice the large majority of the studies doesn't consider the aggregated morphology, assuming also fixed the number layers originated by the exfoliation process per aggregation.

1.4 Micas

Mica is the name used to refer to layered silicate minerals containing primally silicon, oxygen, potassium, aluminum. Mica basic unit consists of two sheets of silica tetrahedrons contraposed, with the tetrahedron vertexes pointing each other. The silica sheets are cross-linked with cations, aluminum in our case (muscovite), and with hydroxyl pairs to complete the cation coordination. Micas usually have excellent chemical stability, heat resistance, and are great heat insulators. Mica has been used in different fields such as aerospace, constructions, metallurgy, and electrical insulation. Has been proven, by few studies, that mica powder can be successfully employed in strengthening and toughening polymeric matrixes.

The preparation method for micas composites requires that the raw materials must be mixed and stirred in advance and then densely bonded to increase the strength through processes such as vacuum filtration and hot pressing. This results in a complicated process, which till now has limited the application of these composite materials for conventional applications. In this paper, we will use a particular mica given by Veneta Mineraria, a minerary company which own the largest deposit of this material ever discovered by now, located in Spain, in Caolines de Vimianzo near La Coruna.

Our Micas can be associated to the family of Muscovites, chemically described as $KAl_2[AlSi_3O_{10}(OH,F)_2]$, as we will see in the characterization. This mica is particularly common in metamorphic gneisses, schists and phyllites. In phyllites, a fine-grained rock, the muscovite occurs as microscopic grains (sericite) that gives rocks a silky luster. Muscovite is also present in some granitic rock and is common in granitic complex and within miarolitic druses. Much of the muscovite, present in igneous rocks, have been formed during, or immediately after the consolidation of magma.

1.5 Filler’s Characterization

In the following section we can take a look to the precise material we are going to employ in this work. For first we have mica10, the smaller particulate. In our case we can talk about nanocomposites, because while the plates have an average extension of about 10 microns, their thickness is in the order of some nanometer, that’s why they possess nano peculiar features. The material shows the characteristic plates morphology of a mica. 10 microns can be considered the maximum plate extension as there are plates way smaller. Here following, we have some ESEM images of our mica10 particulate.

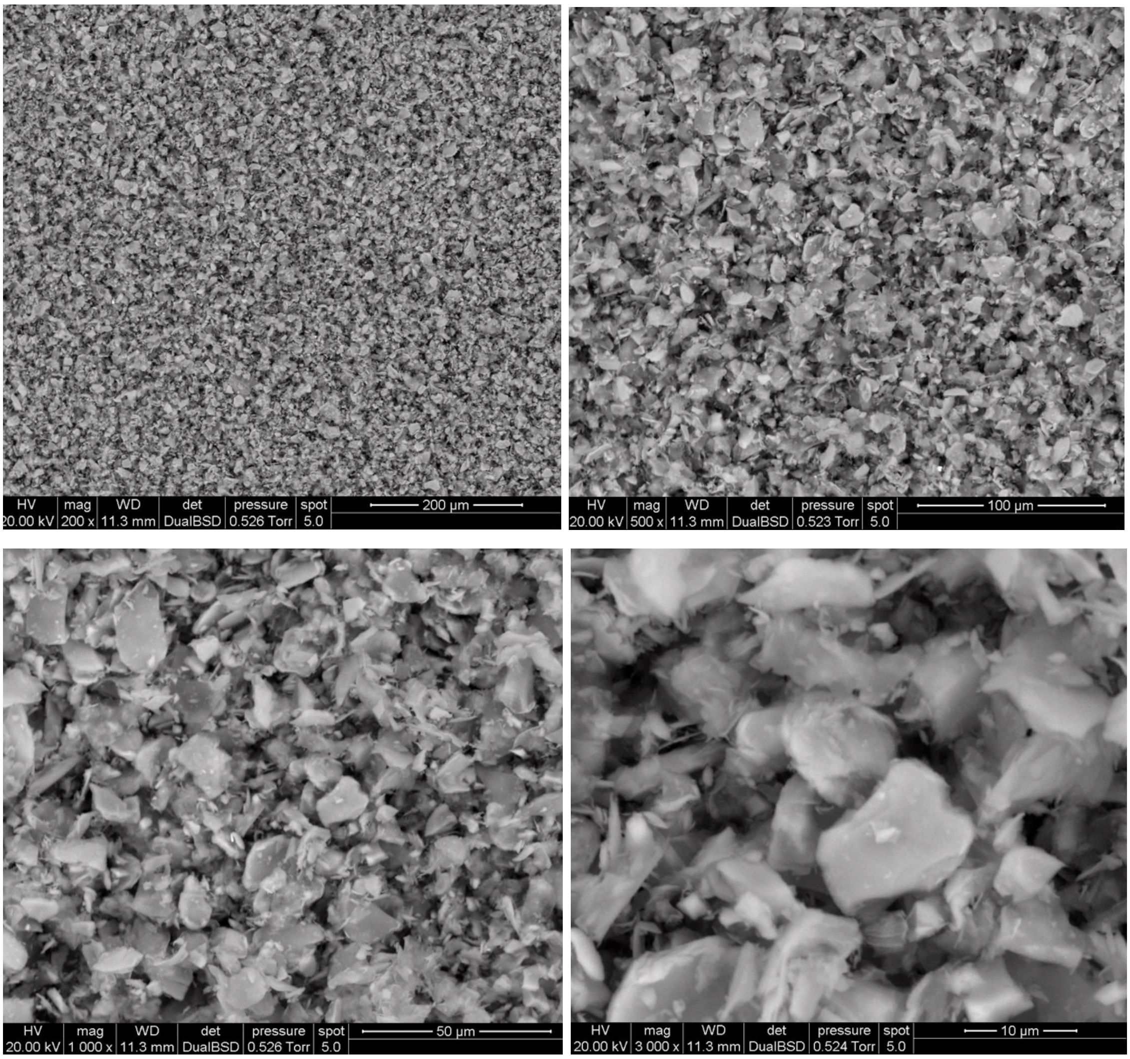

Figure 3 ESEM images of mica10 with increasing magnification.

Here the same analysis for MICA 45. As for the smaller mica, 45 indicates the maximum plate extension, as smaller plates are present in the mixture.

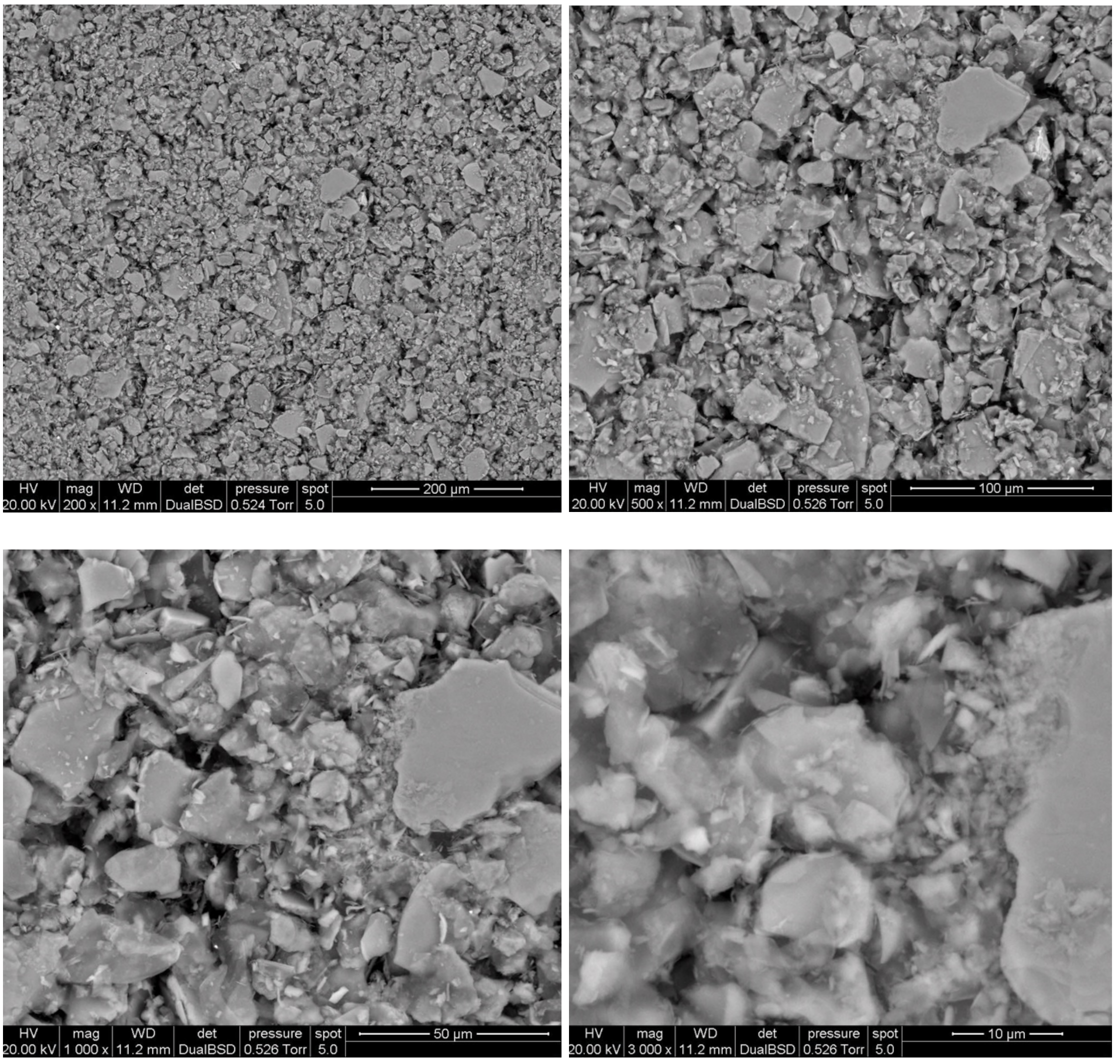

Figure 4 Mica45 ESEM images with increasing magnification.

Following we report some XRF determination performed during the ESEM analysis.

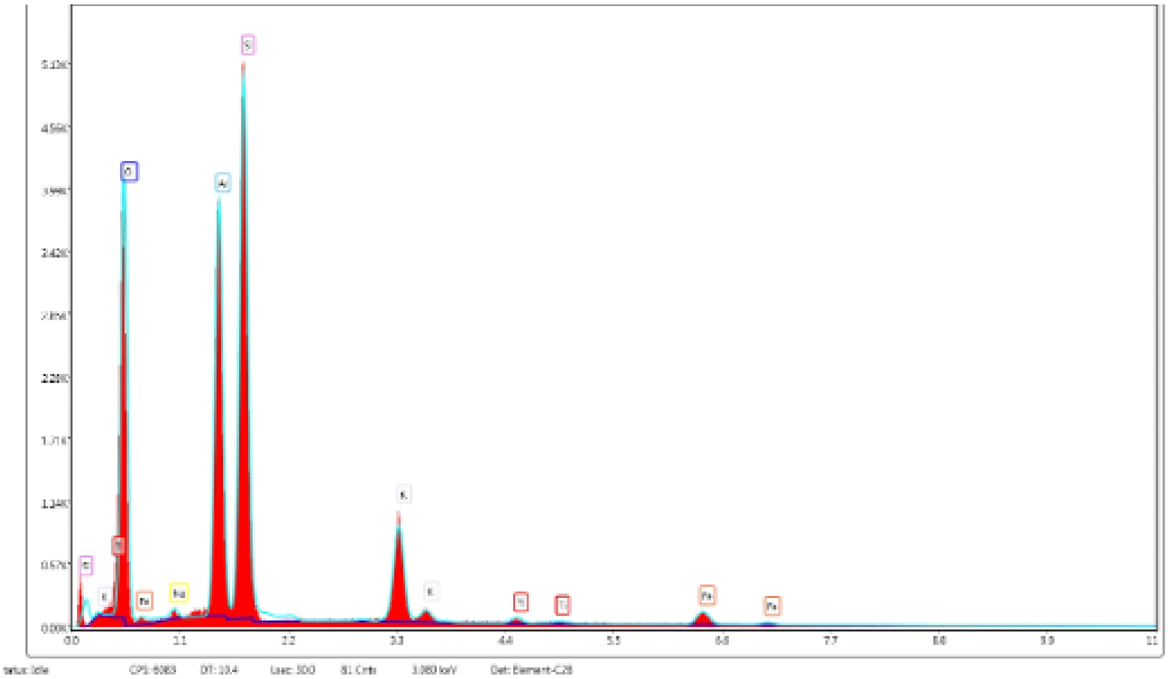

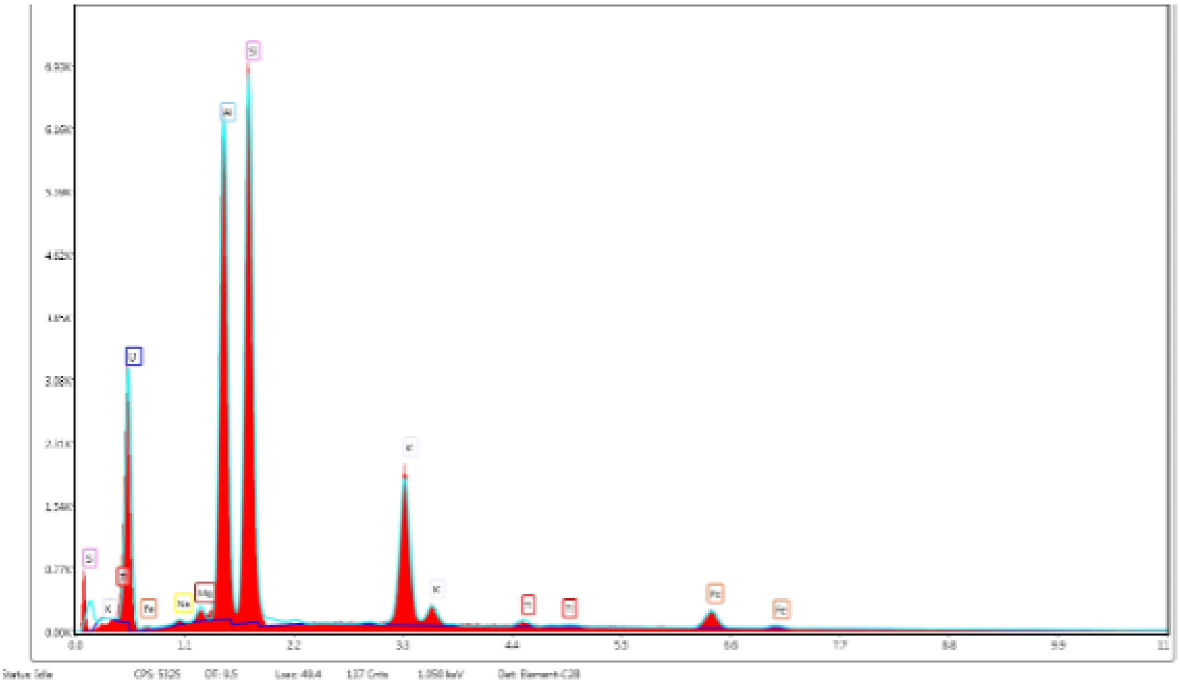

Table 3 (a,b) Element presence in weight and atomic percentage in the particulate (table 3a, left) and in a random single plate (table 3b, right)

Element	Weight %	Atomic %
Na	0.48	0.45
Al	17.47	13.73
Si	24.56	18.54
K	7.62	4.13
Ti	0.6	0.27
Fe	2.52	0.96
O	46.74	61.93

Element	Weight %	Atomic %
Na	0.32	0.3
Mg	0.64	0.57
Al	18.58	14.76
Si	21.91	16.72
K	9.6	5.26
Ti	0.61	0.27
Fe	2.76	1.06
O	45.58	61.06

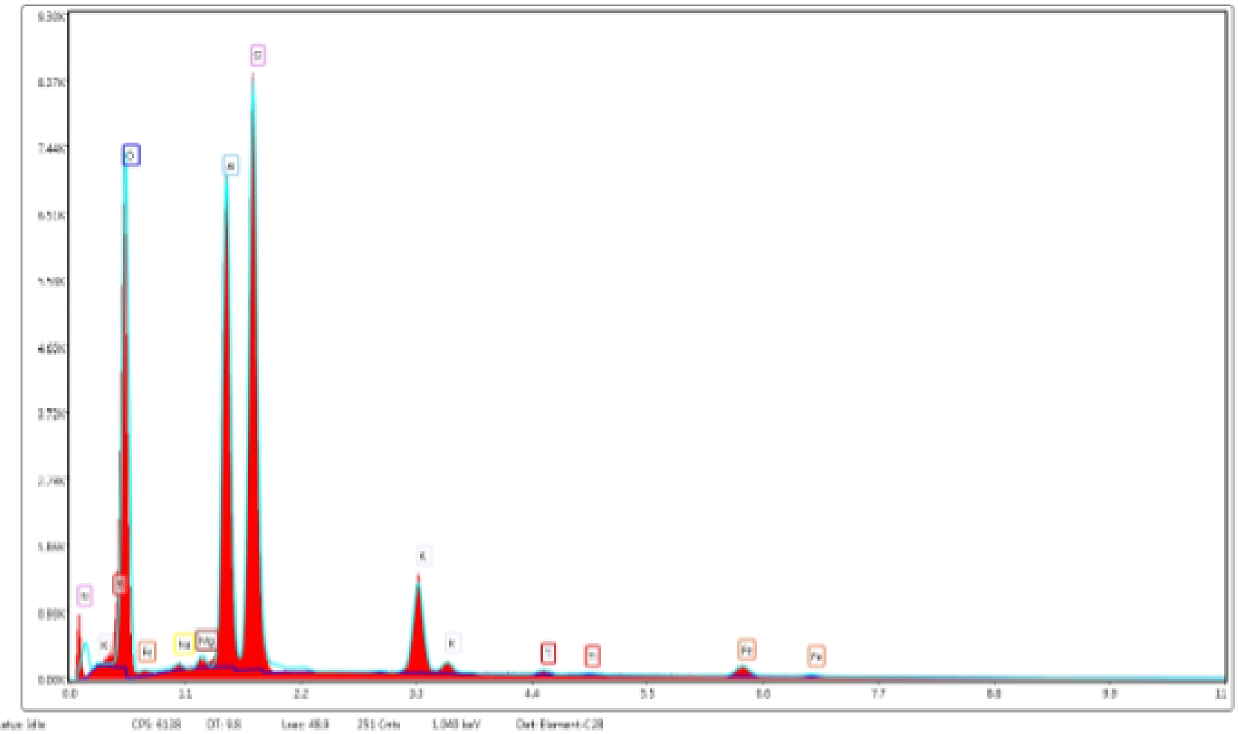

Figure 5 ESEM x-ray fluorescence analysis of mica particulate.

Table 4 Mica45 composition

Element	Weight %	Atomic %
Na	0.32	0.3
Mg	0.53	0.46
Al	18.72	14.55
Si	24.59	18.36
K	6.27	3.36
Ti	0.43	0.19
Fe	1.69	0.64
O	47.43	62.16

Here we show the XRD analysis of mica10.

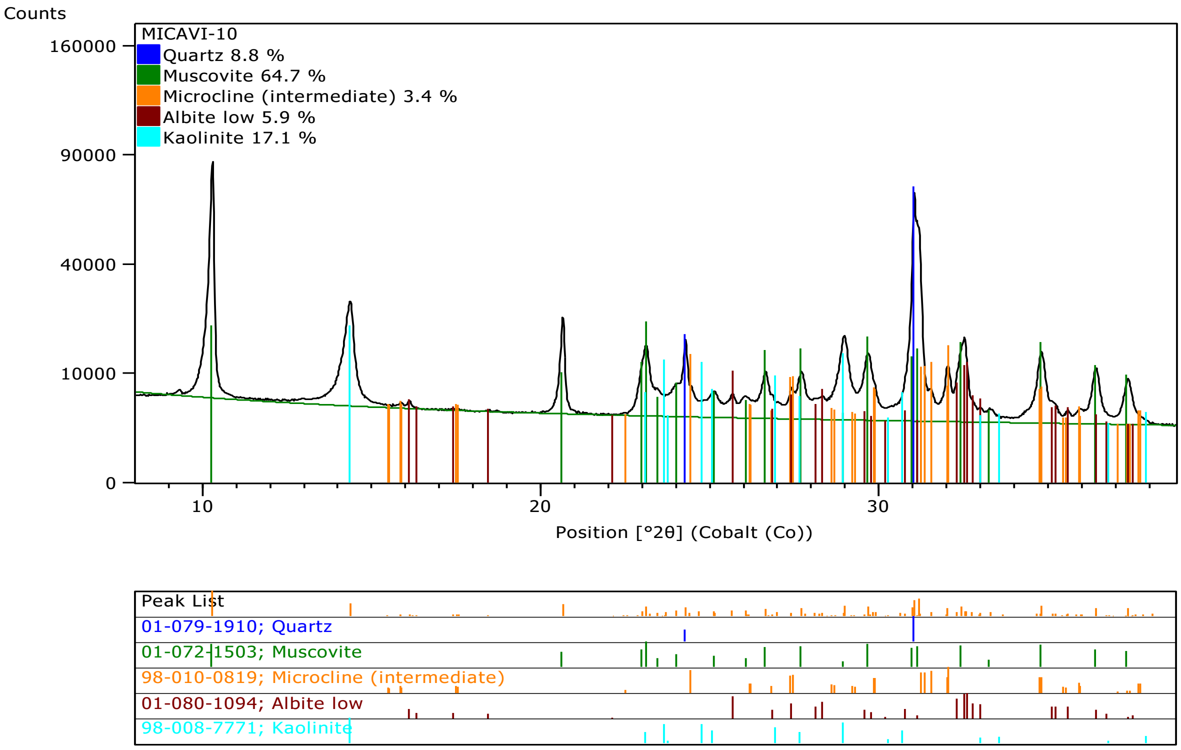

Figure 6 Mica10 XRD analysis.

We can observe that the mica10 particulate contains the following mineral species:

Quartz SiO_2.

Figure 7 Quartz crystals (left), Muscovite (right) with its characteristical shapes

Muscovite $KAl_2(Si_3Al)O_{10}(OH,F)_2$.

Microcline $KAlSi_3O_8$, it is an alkaline feldspar, that separate in parallel plates.

Figure 8 Microcline crystals.

Albite $NaAlSi_3O_8$, common tetra-silicate which crystalize in flat crystals.

Figure 9 Albite.

Kaolinite $Al_2Si_2O_5(OH)_4$, aluminum hydrosilicate whose crystalline lattice is composed of 2 sheets: one composed of tetrahedra containing an Si atom, the other of octahedra containing aluminum, similarly to muscovite.

Figure 10 Kaolinite.

CHAPTER 2

The experimental section

2.1 instrumentation and characterization results

Before describing the real experience in the laboratory, it is useful to spend some words on the instrumentation we used in the materials' analysis.

2.1.1 XRD

X-ray diffraction is a powerful, quite rapid, technique used mainly for phase identification of crystalline materials. Nowadays x-ray diffraction is the most common technique for studying crystalline structures and atomic spacing. In 1912, the german physicist Max von Laue discovered that crystalline substances behave like three-dimensional diffraction gratings for X-ray radiations, whose wavelength is similar to the spacing of the planes in a crystal lattice.

X-ray diffraction is based on constructive interference of monochromatic X-rays and a crystalline sample. The X-rays are generated in a cathode ray tube, filtered to obtain a monochromatic radiation, concentrated and directed toward the sample. With the interaction of the radiation and the sample, when conditions satisfy Bragg's law ($n\lambda=2d \sin \theta$), we obtain constructive interference. It is easy, employing this law, to relates the wavelength of the electromagnetic radiation to the diffraction angle that is correlated to the lattice spacing in the crystalline sample. The diffracted rays are then detected and processed. The conversion of the diffraction peaks to d-spacings, so the distance between planes of atoms, allows the identification of the mineral, since each mineral has his own set of unique d-spacings. Typically, this is achieved comparing the obtained d-spacings with standard d-spacing reference patterns. The X-ray diffractometer is mainly composed of three elements: the X-ray tube, the material holder, and the detector.

The X-ray radiation is obtained in the first section of the machine (from the right, in figure 7), the cathode ray tube, by heating a filament producing electrons which will be accelerated and driven toward the target with the aid of an applied voltage and bombarding the target material with electrons. When electrons have enough energy to dislodge inner shell electrons of the target material, X-ray radiations are produced. The target material is always a metal, such as Cu, Fe, Mo. A further filtration made with monochromators, is necessary to produce monochromatic X-rays useful for our purpose.

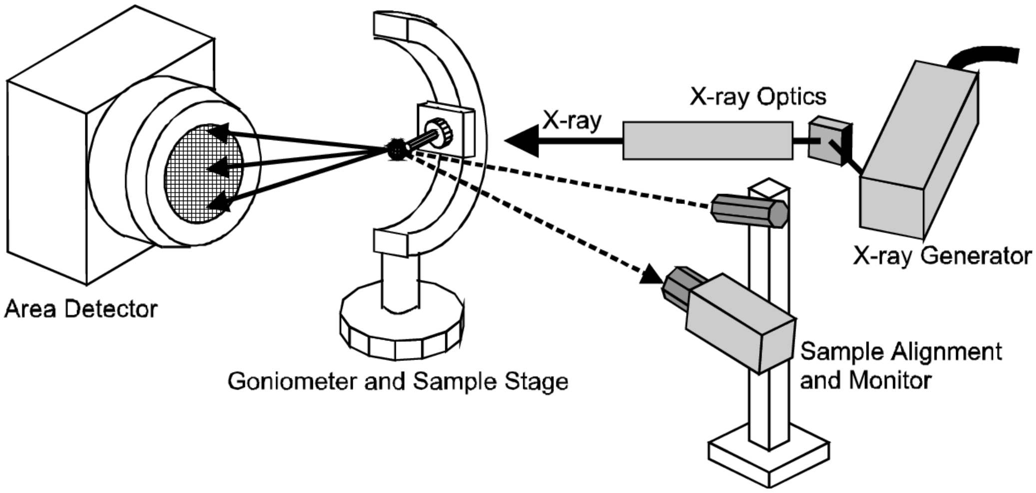

Figure 11 X-ray diffraction machines set-up.

X-rays are then focalized toward the sample, and when the characteristics of the X-rays impinging the sample satisfies the Bragg Equation, we have constructive interference, thus we obtain a peak in the intensity of the signal. The detector receives the radiation and eventually processes the signal, operating a count which is our output that can be directly sent to a computer.

2.1.2 SEM and ESEM

Scanning electron microscope, usually indicated with its acronym, SEM, is a scanning technique which employs a highly energetic electrons beam to produce a set of signals from the interaction between the radiation and the specimens. The signals provide different information, including the external morphology, the chemical composition, the crystalline structure and the different phases disposition in the sample. Data are collected over a small area of the sample's surface, generating an image that can be directly interpretated by the operator. The magnification archivable with this technique is up to 30,000X, with a spatial resolution of 50 to 100 nm.

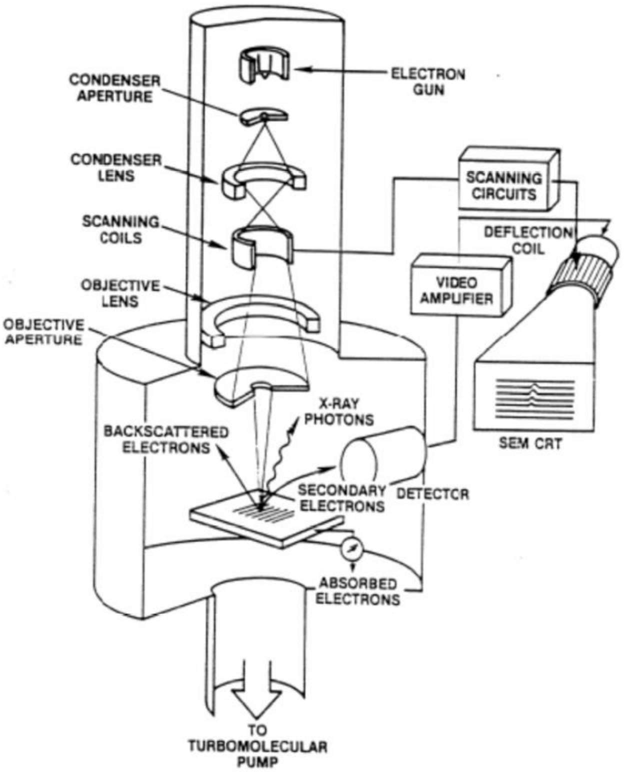

Figure 12 Schematic view of a SEM microscope

Going deeper into the description of the mechanism, the electrons are thermionically emitted from an electron gun fitted with a filament cathode, usually made of tungsten or lanthanum hexaboride. The accelerated electrons possess a discrete amount of kinetic energy, and this energy is dissipated as a variety of signals is produced by the collision with the sample. These signals are mainly due to secondary electrons (which are the one observed in the final images), backscattered electrons, diffracted backscattered electrons (which are useful to determine crystal structures and the disposition of the phases of the material), x-ray photons, visible light and heat. While secondary electrons are most valuable for showing morphology and topography of the specimen, backscattered electrons are useful to show contrasts in the composition of multiphase sample giving rise to signal related to the atomic number (i. e. the electron number) of the different atoms in the specimen. X-rays are produced by inelastic collisions between the accelerated electrons and electrons in inner atomic orbitals of the sample material. Scanning electron microscope analysis are "non-destructive" in fact, the generated x-rays do not lead to volume loss of the specimen and so it is possible to analyze the same sample repeatedly. The whole column of the microscope operates under high vacuum to prevent air scattering of either the incident beam on the subsequently produced electrons.

ESEM is a particular variation of the SEM technique that differs from the standard method mainly for two aspects. While in SEM the specimen had to be maintained under a vacuum, with ESEM, the work environment is held at the average pressures of 10^{-5} Pa, achieved using differential pumping system along the column, in the way to have progressive different pressure zones. At the sample level, the pressures arrive to about 1000 Pa. The other main difference between SEM and ESEM is that there is no need of metallic layer in front of the insulators, because we can take advantage of a special mechanism to dissipate the charge, generated by incident electrons, due to the presence of gas in the chamber. A high vacuum is required in the SEM to stop electrons scattering, a process that degrades the resolution of the image while with ESEM the free electrons travel through gas particles but not for long, so the probability of strong collisions is low. This affect the probe design and lead to only a slight resolution loss, due to a reduction of the signal to noise ratio with reference to the SEM, but this drawback is usually less important than the benefits.

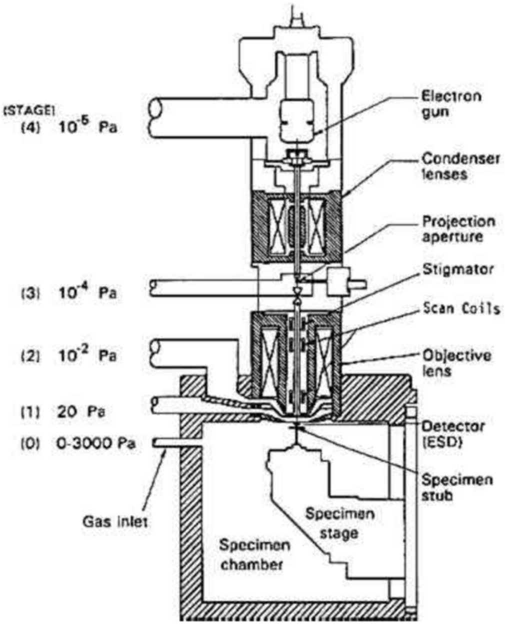

Figure 13 Schematic view of an ESEM microscope.

The gas is not simply passive in the process, but it is really important for the signal detection. As secondary or backscattered electrons are generated, they must travel through the gas particles too. The electrons with the lower energy, have a high probability of strong collisions, leading to the ionization of the gas molecules. Each ionizing collision bring to the emission of an additional electron, leading to a cascade reaction. All the electrons produced are directed towards the detector, induced by an electromagnetic field. The original ESEM detects flows of ionized particles in the gas, but as many manufacturers entered in the market, everyone developed his own methods for the signal detection. The creation of cascade electrons originates obviously positive ions, which drift down towards the sample and compensate the residual charge in the insulator's surface. This mechanism is the one thus insulator coating is not needed anymore to prevent the charging of the machine and so the degradation of the image resolution. The images obtained with this instrument were showed in the filler's characterization paragraph.

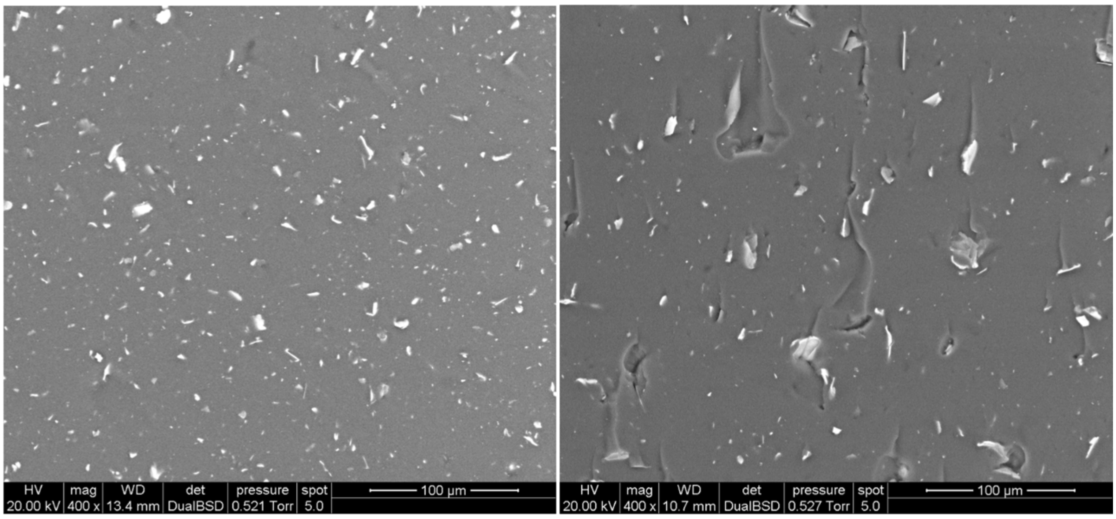

Figure 14 ESEM imges of the mica-epoxy nanocomposite after the tensile test. On the left mica10 3%, on the right mica45 3% where it is easy to notice the cracks propagating from the platelets.

2.1.3 TEM

The TEM, acronym of transmission electron microscopy is a magnifying technique which permit to analyze the material's structure with atomic resolution and contemporarily giving chemical and crystallographic information of sub-micrometric areas of the material. With this technique a high energy electron beam pass through an ultrathin specimen, with a thickness between 50 and 500 nm. The image is obtained from the interaction of the electrons and the of the sample. The electronic beam passes through a complex system of electromagnetic lenses that control the radiation to magnifies the image that is collected in an imaging device that, in the most modern TEM, is a CCD but can also be a fluorescent screen or a photographic film. Here we show some images obtained with the TEM of our university.

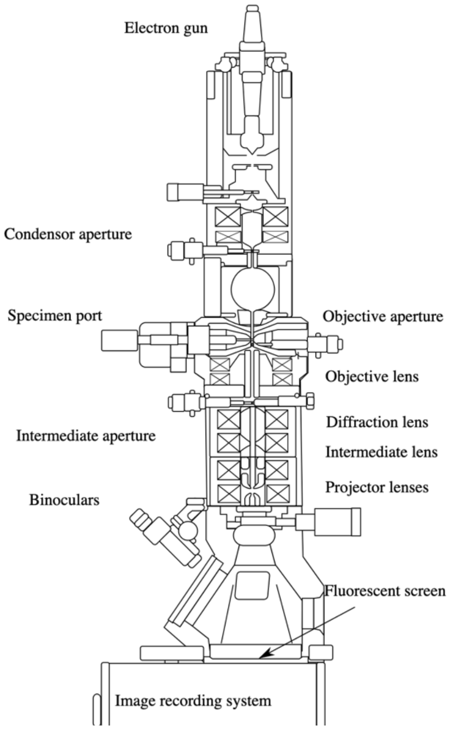

Figure 15 TEM scheme.

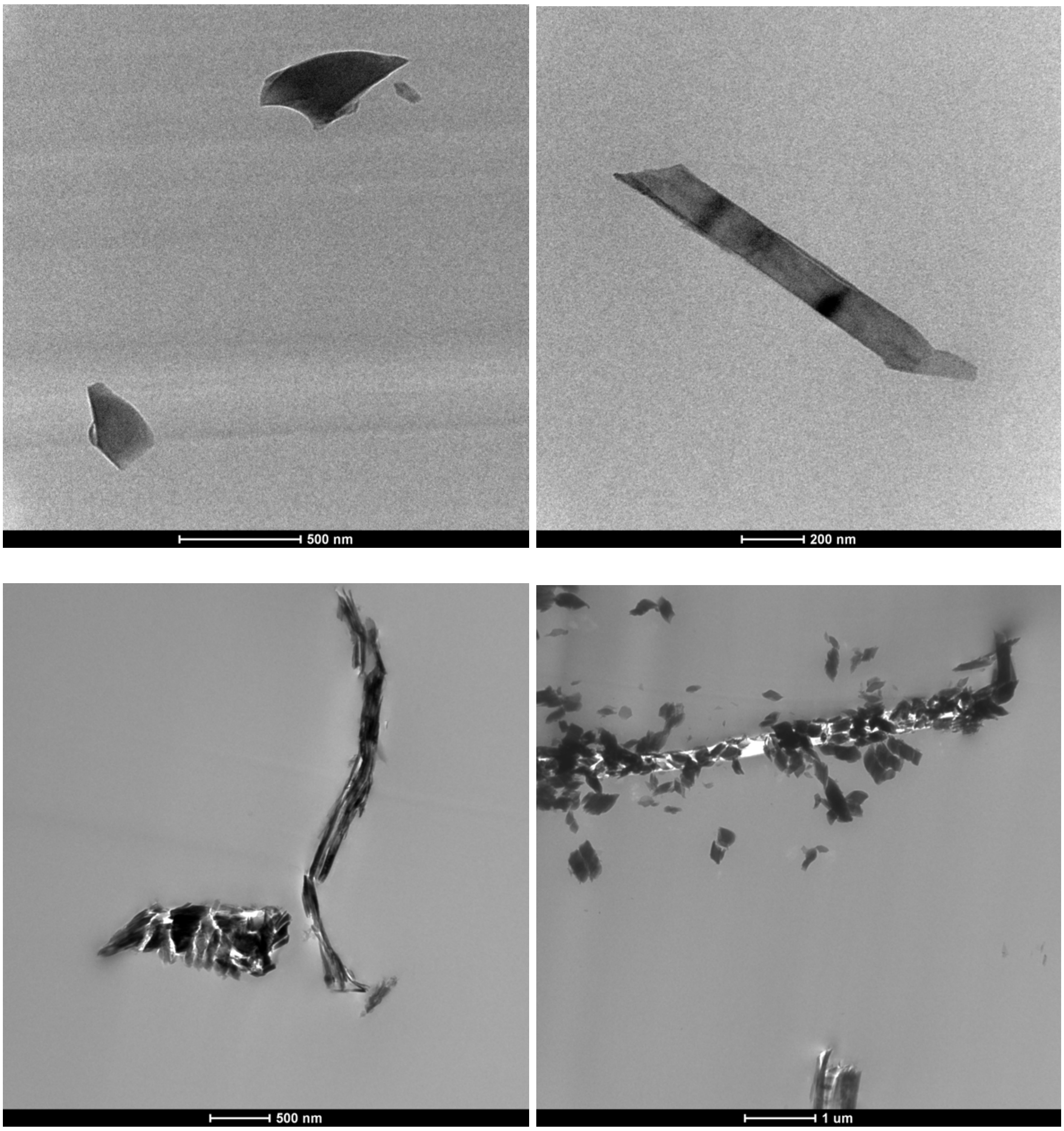

Figure 16 TEM images of mica10 (3%), dispersed into the epoxy matrix. On the top two images we can clearly distinguish the geometry of fully exfoliated platelets. In the two images on the bottom, we can see some platelets aggregation. In the bottom right image is clear that the platelets have moved to reach the fracture, a phenomenon caused by the cut of specimen with the microtome.

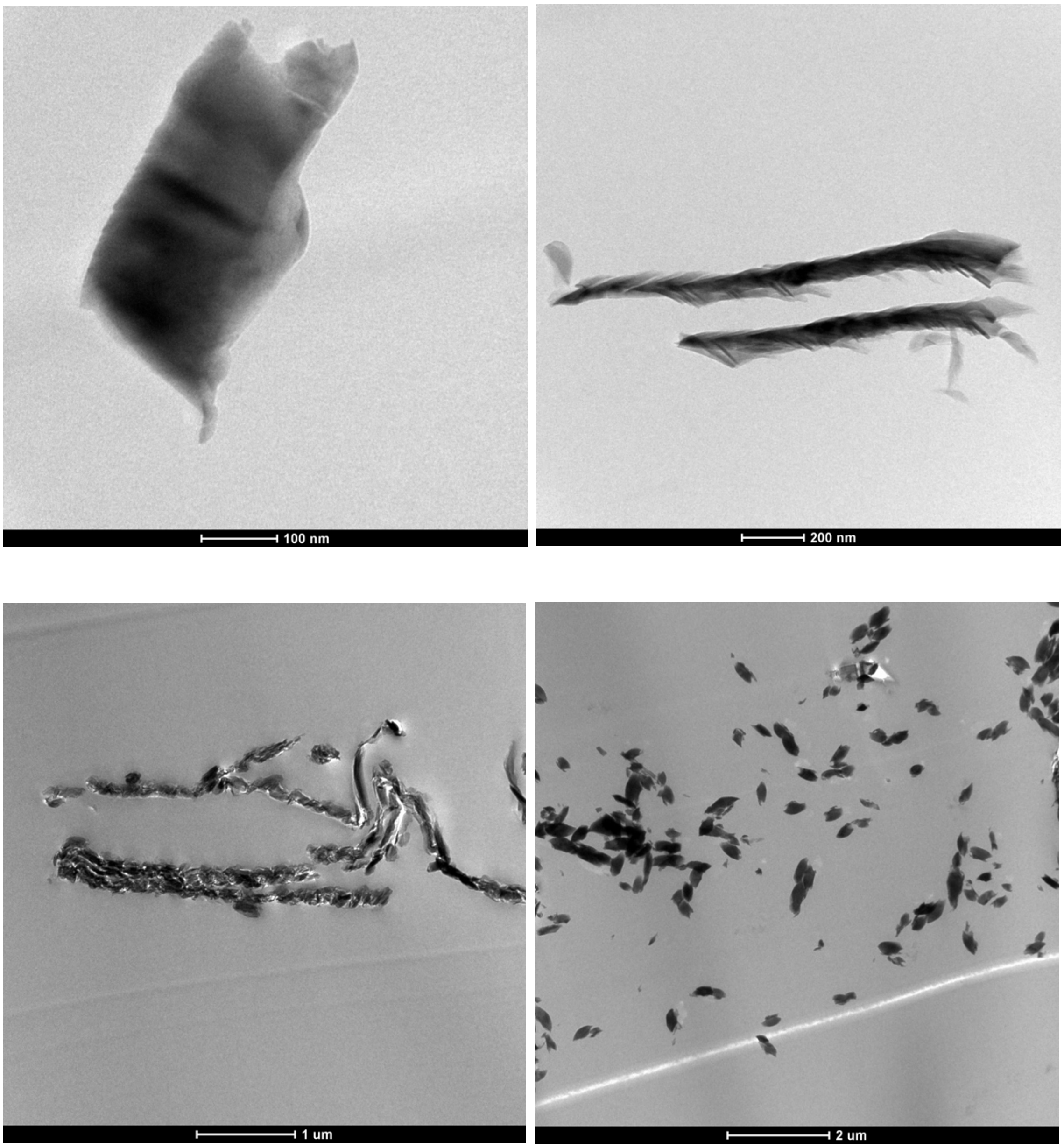

Figure 17 TEM images of mica45 (3%), dispersed in the epoxy matrix. On the top left image, we can. see a single platelet. In the top right and bottom left images, we can see some unique structures that we have seen only with mica45, where the platelets are disposed with a herringbone disposition. In the bottom right image, some particular platelets aggregation.

2.1.4 Thermogravimetry

The thermogravimetric analysis is a powerful tool to study how materials behave at different temperatures. Thermogravimetry is specific to the study the decomposition and oxidation reactions and physical process, such as sublimation, vaporization, and desorption caused by a temperature change. It is especially useful for the study of polymeric materials, including thermoplastics, thermosets, elastomers, composites, films, fibers, coatings, and paints. TGA measurements provide several important information crucial in the process of selection of a material for a particular application. Thermogravimetric techniques are frequently used also to study the melting and crystallization temperature of polymers. The instrument used for this analysis, consists of three different elements: the balance, the furnace, capable of providing a precisely linear heating, a temperature programmer, for measurement and control, and a data recorder.

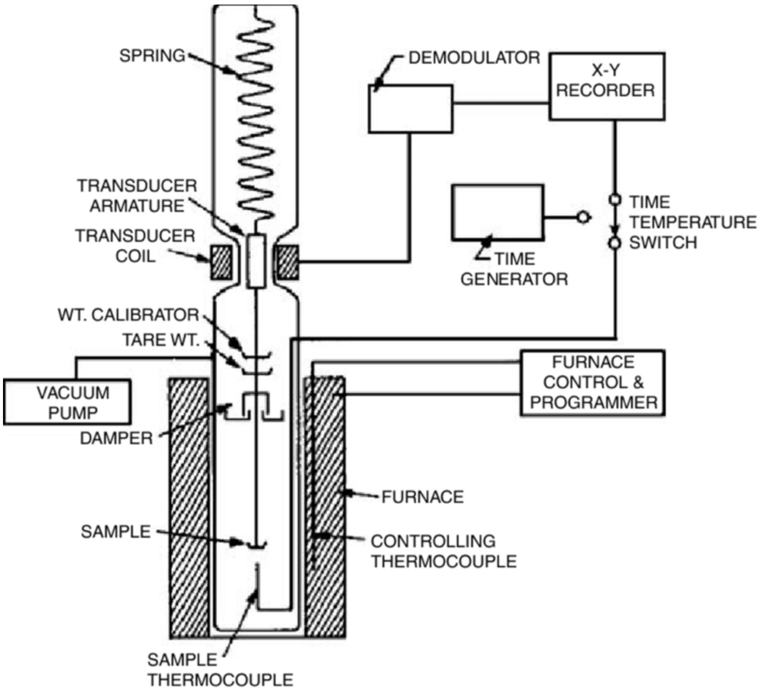

Figure 18 Schematic view of a thermogravimetric analysis machine.

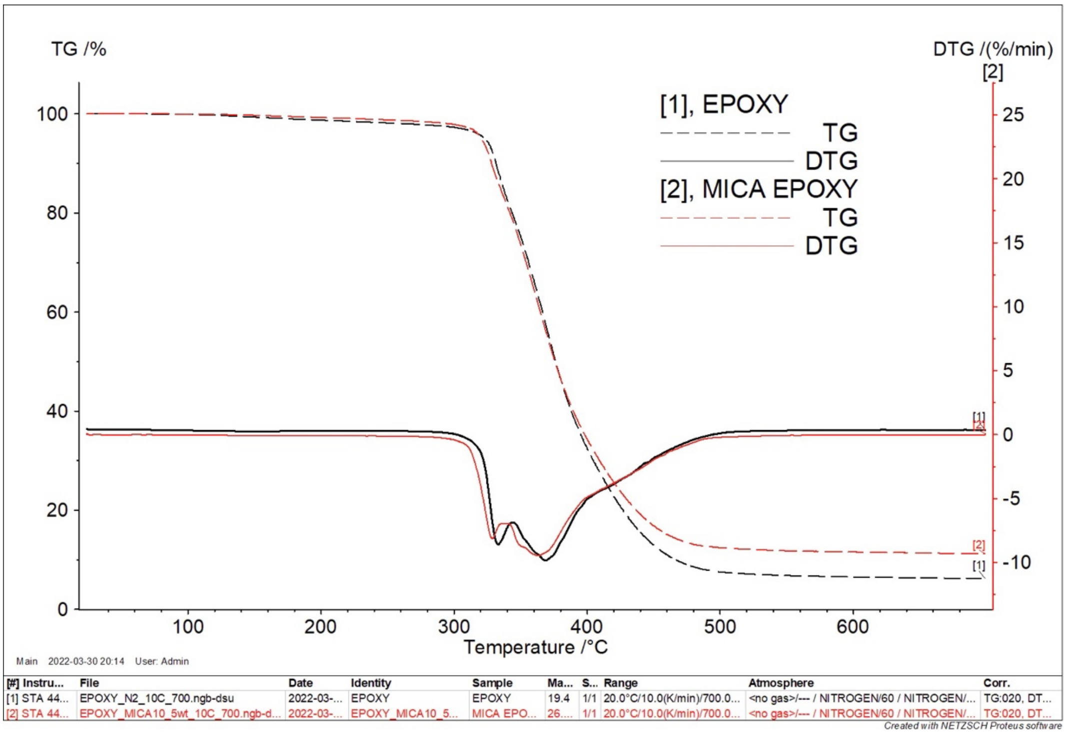

[#] Instru...	File	Date	Identity	Sample	Ma...	S...	Range	Atmosphere	Corr.
[1] STA 44...	EPOXY_N2_10C_700.ngb-dsu	2022-03-...	EPOXY	EPOXY	19.4	1/1	20.0°C/10.0(K/min)/700.0...	<no gas>/--- / NITROGEN/60 / NITROGEN/...	TG:020, DT...
[2] STA 44...	EPOXY_MICA10_5wt_10C_700.ngb-d...	2022-03-...	EPOXY_MICA10_5...	MICA EPO...	26....	1/1	20.0°C/10.0(K/min)/700.0...	<no gas>/--- / NITROGEN/60 / NITROGEN/...	TG:020, DT...

Figure 19 Thermogravimetric analysis of the epoxy resin and the mica10 5% specimen.

Table 5 thermogravimetry results.

	RT-250°C (primarly H_2O and volatiles)	250°C-700°C	Remnant at 699.2°C
EPOXY (19.4 mg weighted)	-1.87%	-91.98%	6.20%
EPOXY/MICA10(5%) (26.18 mg weighted)	-1.27%	-87.59%	11.21%

	T $_{onset}$	DTG	DTG	T @5%mass loss	T @10%mass loss
EPOXY	323.8°C	333.0°C	368.5°C	320.5°C	328.1°C
EPOXY/MICA10(5%)	319.6°C	328.6°C	363.1°C	323.3°C	331.4°C
Δ EPOXY-EPOXY/MICA(5%)	4.2°C	4.4°C	5.4°C	2.8°C	3.3°

Weight loss in % without H_2O and volatiles	Effective mass (no H_2O)	250°C-700°C	Remnant at 699.2°C
EPOXY	19.04 mg	-17.84 mg, 93.7%	1.20 mg, 6.3%
EPOXY+ MICA10(5%)	25.85 mg	-22.93 mg, 88.7%	2.93 mg, 11.3%

Apparently, there are no changes between the test on the epoxy resin and the mica10 5% composite.

2.1.5 FT-IR and ATR

FT-IR is the acronym with which we indicate the Fourier Transform Infrared analysis, one of the most powerful methods of infrared spectroscopy. In this spectroscopic technique, the infrared radiation passes through the sample and so a discrete quantity of radiation is absorbed by the analyzed material. With this procedure we obtain a spectrum that indicates the molecular absorption and transmission of the sample. Every molecular structure has its own infrared spectrum because each one is a unique combination of atoms and so there are no molecules with the same spectrum, making extremely simple recognizing what we are analyzing by comparison with others. IR spectroscopy has been the principal technique for materials analysis in the laboratories of the whole world in the last decade. Each absorption peak corresponds to the vibration's frequencies between the atomic bonds of the analyzed material, according to the relationship:

$$\nu = \frac{1}{2\pi c}\sqrt{\frac{k}{\mu}}$$

Where ν = wavenumber [cm^{-1}]

k = atomic bond's energy

μ = reduced mass = $\frac{m_1 \cdot m_2}{m_1+m_2}$

IR spectroscopy can be utilized for qualitative analysis of every different kind of material and also is possible to determine the amount of the constituent materials by the size of the peaks in the spectrum. With modern software algorithms, infrared spectroscopy is an excellent tool for quantitative analysis of different kind of material.

Fourier Transform Infrared spectrometry was developed to bypass the limitations constraining of dispersive instruments. The biggest problems of these techniques were related to the speed of the scanning process. A solution was developed with the implementation of an interferometer that permit to measure all the frequencies together, rather than individually.

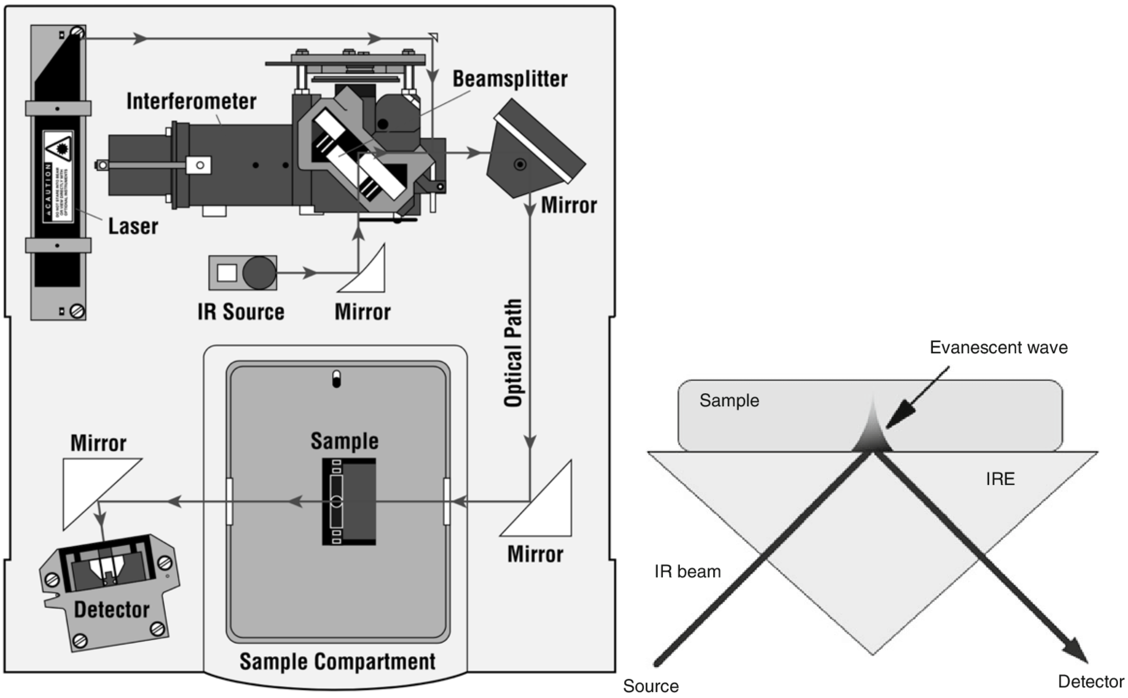

Figure 20 (left) Schematic view of an FT IR machine. (right) Evanescent wave in the ATR.

The interferometer produces a unique type of signal that can be read very quickly by the electronics. Usually interferometers employ a beamsplitter (a dichroic lens) which divides the incoming radiation beam into two separated beams. One beam arrives to flat fixed mirror, the other reflects on a mirror mounted on a mechanism which allows it to stir with a high accuracy, varying its distance from the beamsplitter. The two beams then, are directed back to the beamsplitter where they recombine. The beam travelling in the fixed path always takes the same time while the other travel time depends on how their distance change. The signal which exits the interferometer is the result of these two beams interfering with each other and it is so called interferogram. The analysis requires the plot of the intensity at each individual frequency to make an identification. The measured interferogram signal cannot be interpreted directly because in the "decoding" it is necessary to perform the Fourier transformation of the signal. This transformation is performed by the computer that display then an output understandable by the analyst.

An alternative to FTIR is the attenuated total reflection ATR analysis. With this technique the sample, that can be solid or liquid, is analyzed near the optical element where the radiation is totally internally reflected. The effective path length for the interaction between the sample and the radiation depends on many variables and is usually in the order of a fraction of the radiation wavelength. Because of the small radiation penetration, the ATR technique is perfect to analyze highly absorbing materials or ultra-thin films. Differently from what happens with FTIR, whereby the light must completely pass through the sample, in ATR analysis the thickness of the sample is not relevant. A solid or liquid sample can have thickness of 10 microns or 10 cm and in any case, it is possible to acquire a useful FTIR spectrum. Moreover, ATR sensors are abrasion resistant and capable of tolerating the harsh conditions associated with many chemical reactions. This feature makes ATR an excellent technique for studying many chemical reactions, as the preparation or dilution of the sample is not needed. Additionally, to absorption features, ATR spectra has also reflection characteristics so, to obtain a spectrum totally comparable with a standard FTIR spectrum, is necessary to separate the two contributions. The optical constants of materials, required to compute the reflection contribution, are determined by combining measurements made at different angles of incidence. To do this we need to use the Kramers-Kronig method, based on the interdependence of the optical constants by integral relation and on the use of Fresnel's equations. Here are shown the results of the analysis.

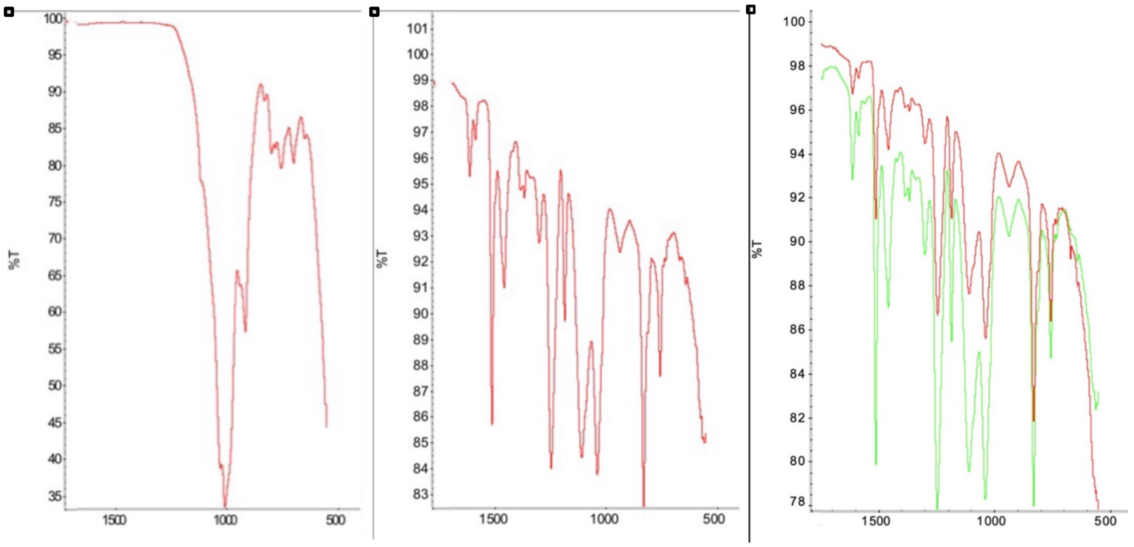

Figure 21 FT-IR analysis of epoxy resin (left), mica10 1% and mica10 5% (green) in comparison with epoxy (right).

With reference to the graphs in figure 21, we can attribute the most intense absorptions to:

1608 cm^{-1} stretching of the C=C aromatic double bonds

1509 cm^{-1} stretching of the C-C aromatic single bonds

1247 cm^{-1} stretching of the C-O-C groups

1181 cm^{-1} stretching of the C-O aromatic bonds

1105 cm^{-1} stretching of the C-O-C groups

1035 cm^{-1} bending of the C-O-C groups

827 cm^{-1} stretching of the epoxydic groups

752 cm^{-1} rocking of the CH_2 groups

Here we can observe that the intense signal of the mica at 1003 cm^{-1} is masked by those of the epoxydic polymer.

2.1.6 Mechanical tests

In addition to the analytic instrumentation for chemical/morphological/physical characterization, we must mention also the mechanical test machines. The two machines, the one for the tensile test and the other for fracture test will be accurately described in the next chapter, in the relative mechanical test section.

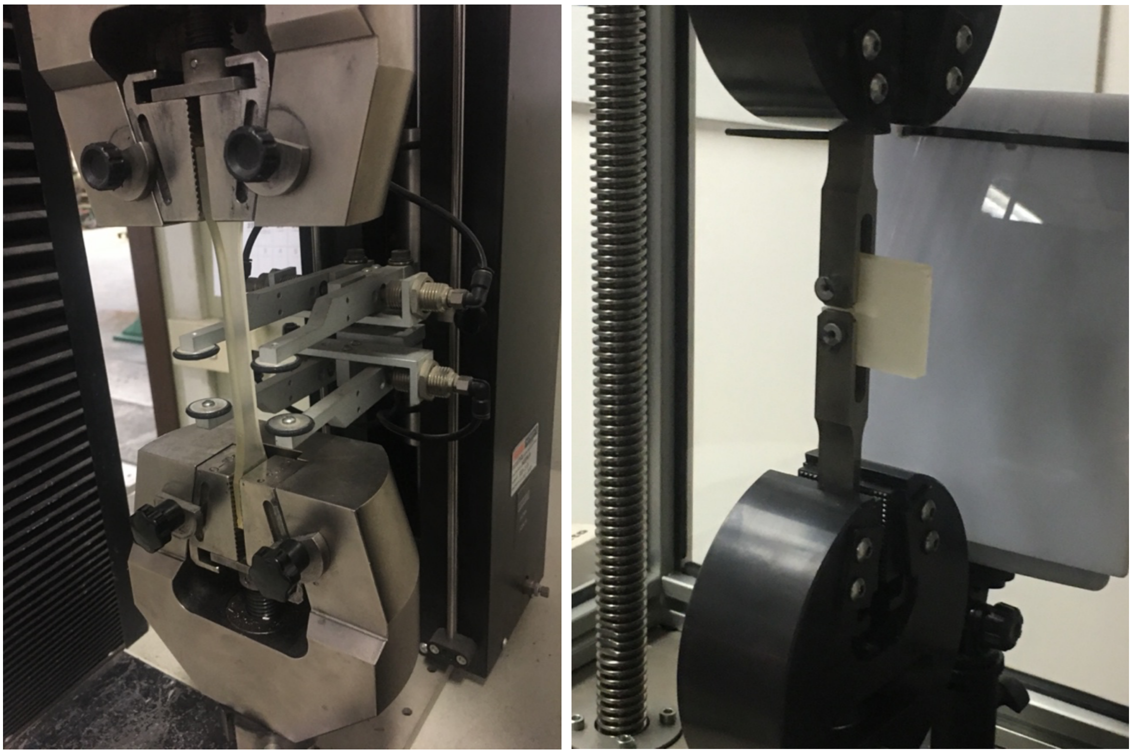

Figure 22 On the left the dogbone specimen during the tensile test, on the right the CT specimen in the fracture test.

2.2 The preparation of the mica-epoxy specimens

The most immersive part of this study has been for sure the preparation of the specimens destined to tests and analysis. In this work we prepared five different sets of specimens, changing the type, and the percentage in weight of the filler. With mica10 we prepared three sets, 1%, 3% and 5%, while with mica45 we prepared only two sets, 1% and 3%, because from previous research 5% of mica45 would probably have led to specimens with bad performance due to excess of reinforcement. A single set of specimens took a day of work to be made, plus the polymerization time. The crafting of the specimens started with the weighing of the epoxy resin, the ammine and the mica. We started pouring the resin in the schlenk flask, that was fixed under the mechanical mixer and then starting the stirring. We slowly added the mica as the mixer is turning. Depending on the percentage of mica the first mixing phase took different times, till we saw that the filler was completely disperse without the presence of aggregations. During this first procedure, the whole flask was immerse in warm water, with a temperature of about 30° C. After the first mixing, we took out the flask from the water and poured the ammine while the mixer worked, then we waited a bit before moving to the second mixing station. This third stage consisted in linking the inlet of the flask to the void pump, while keeping the compound mixed by an electromagnetic mixer. The materials needed to be mixed under vacuum to remove the air which could lead to the formation of bubble in the specimen. All the precise times are collected in the table 5 below.

Table 6 Times required in the different mixing process in the various specimens' preparation.

Specimen	First mechanical	Mechanical+ammine	Magnetic+vacuum
MICA10 1%	15 min	25 min	45 min
MICA10 3%	15 min	25 min	30 min
MICA10 5%	15 min	30 min	30 min
MICA45 1%	20 min	15 min	30 min
MICA45 3%	20 min	15 min	30 min

Figure 23 Photos from our laboratory. On the left, the mechanical mixer, on the right the mixing of the components during the specimens' preparation.

After the mixture seemed to be without bubbles, it was poured in silicone molds, made in house from legit steel countermolds. Then the specimens were left to polymerize for 2 days in controlled temperature room at 20° C and then in an oven at 60° C for 7 hours.

Figure 24 The silicone molds we employed in the specimens' preparation

Here following is shown how the specimens appeared once finished. For every set is specified the composition.

Mica10 1%: 120 g epoxy resin, 40 g ammine, 1.6 g mica

Figure 25 Mica10 1% specimens.

Mica10 3%: 120 g epoxy resin, 40 g ammine, 4,8 g mica

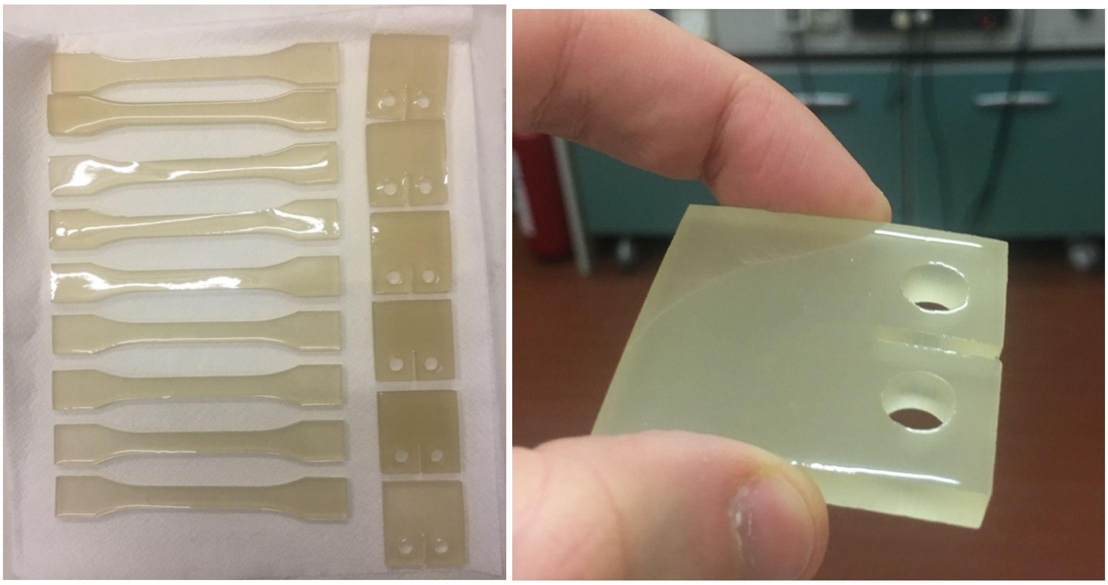

Figure 26 Mica10 3% specimens.

Mica10 5%: 120 g epoxy resin, 40 g ammine, 8 g mica

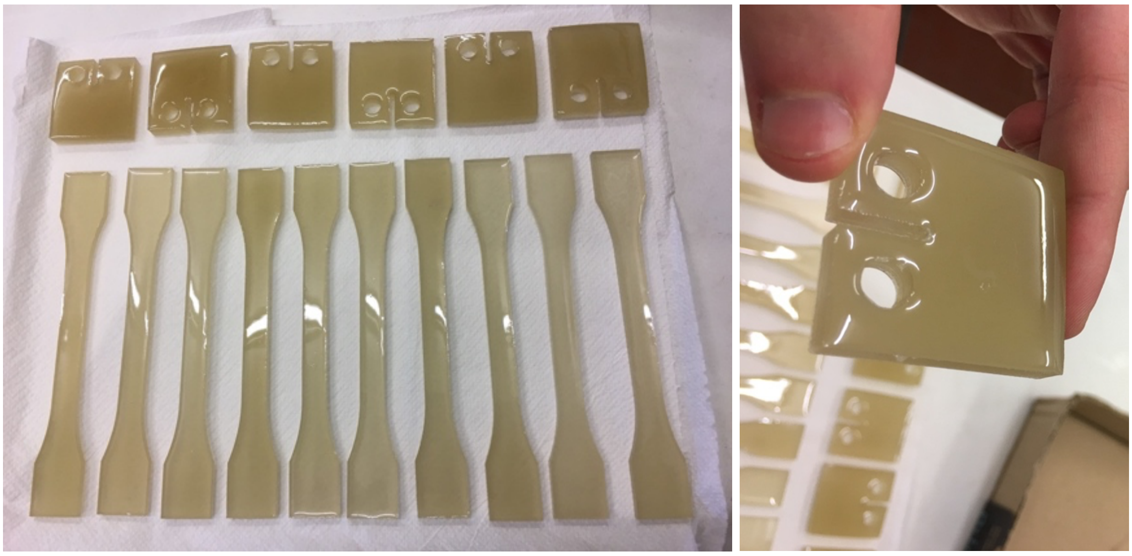

Figure 27 Mica10 5% specimens. The specimens were however semi transparent, but the change of color from the previous sets is appreciable.

Mica45 1%: 120 g epoxy resin, 40 g ammine, 1.6 g mica

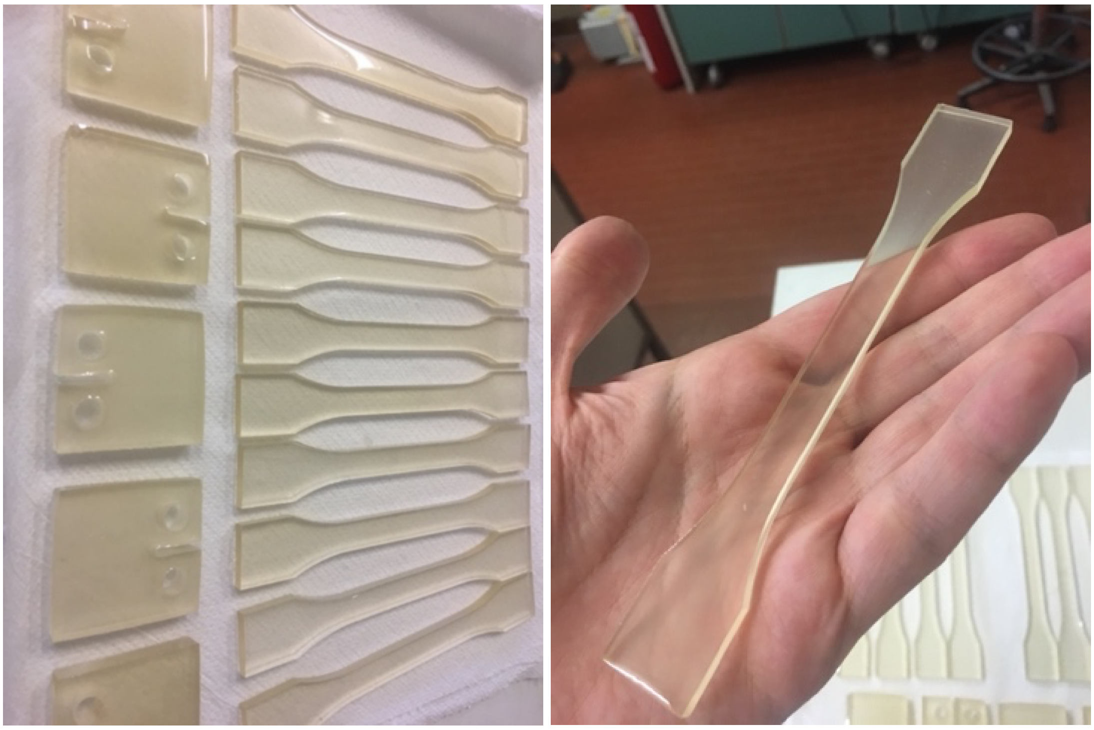

Figure 28 Mica45 1% specimens.

MICA45 3%: 120 g epoxy resin, 40 g ammine, 4.8 g mica

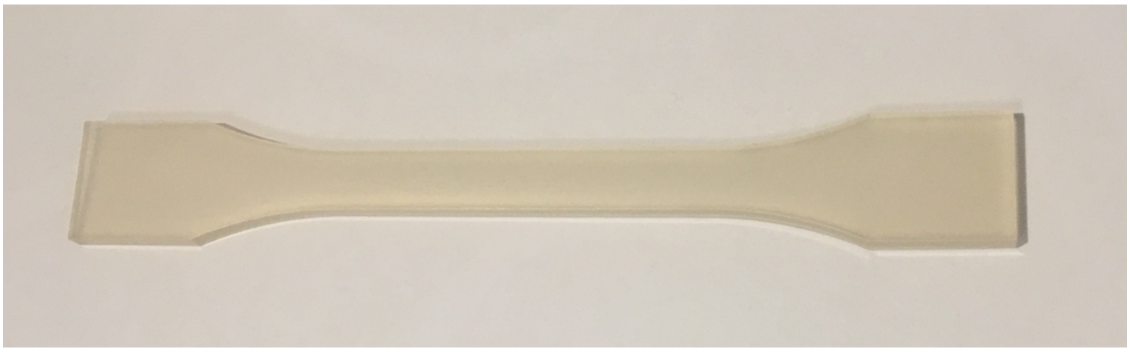

Figure 29 Mica45 3% dogbone specimen.

2.3 Transparency

One of the aspects that amaze the most, is the extraordinary transparence of all the specimens. All sets were transparent, with some slightly yellow reflexes, turning more and more brown in the specimens with a bigger filler percentage. There is no difference, by eye, between specimens with the same amount of filler but mica of different maximum dimension.

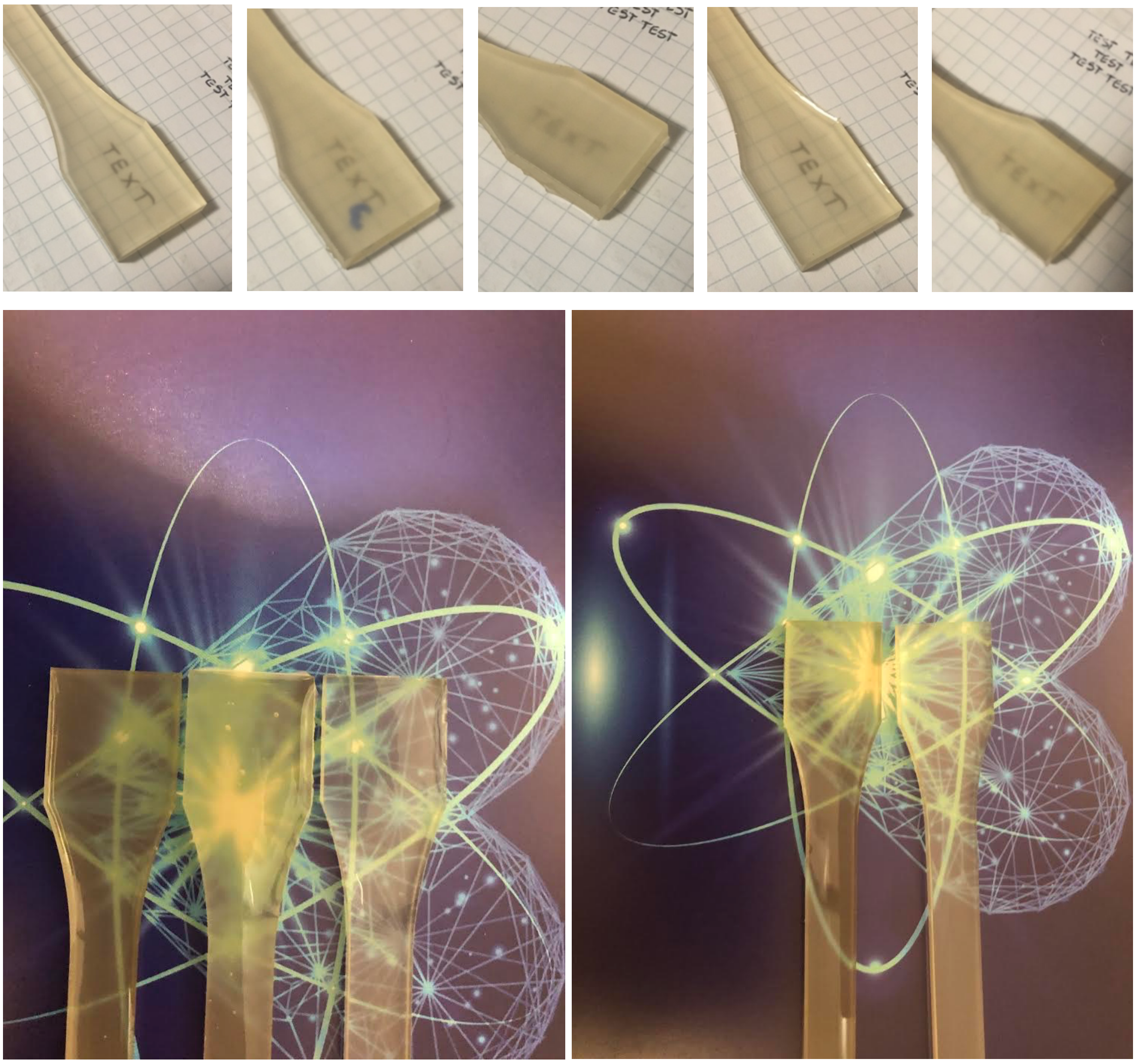

Figure 30 Two different representation, where we can compare the different transparency of the specimens. In both series of images, the disposition of the specimens is, starting from left, mica10 1%, 3%, 5%, mica45 1% e 3%.

CHAPTER 3

Data Analysis

Of course, one of the main purposes of this work is the definition of the mechanical properties of the specimens. We carried out two different mechanical tests: the tensile test and the fracture test. The tests took place in different location, the tensile stress test was made in the DICEA departement laboratories of our university, here in Padova, while the fracture tests were effectuated in Vicenza, always in a laboratory of the university of Padova (DTG department).

3.1 Tensile test

In a tensile test, the specimen is simply gripped at each end and pulled apart. Because the grips hold the specimen by exerting a clamping force, they always inflict some damage to the specimen. To avoid these events the specimens are designed with a narrower section in the center while having wider extremities. This particular shape is usually called "dogbone". It is clear that small cracks lead to the weakening of the specimen, negatively affecting the trial. In our test this happened once, causing a small crack near the tip of the dogbone, but it was so small that it didn't affect the specimen strength.

The whole shape is regulated by ASTM D 638, or the equivalent ISO 527-1, to be sure that the trials give comparable results. Every opposite edge must be as parallel as possible, and the angles must be as near to 90° as possible, in order to be able to measure the width accurately. As we have seen in the previous paragraph, the specimens in our case have been produced with a specific silicone mold that respect the imposed measures (table 6).

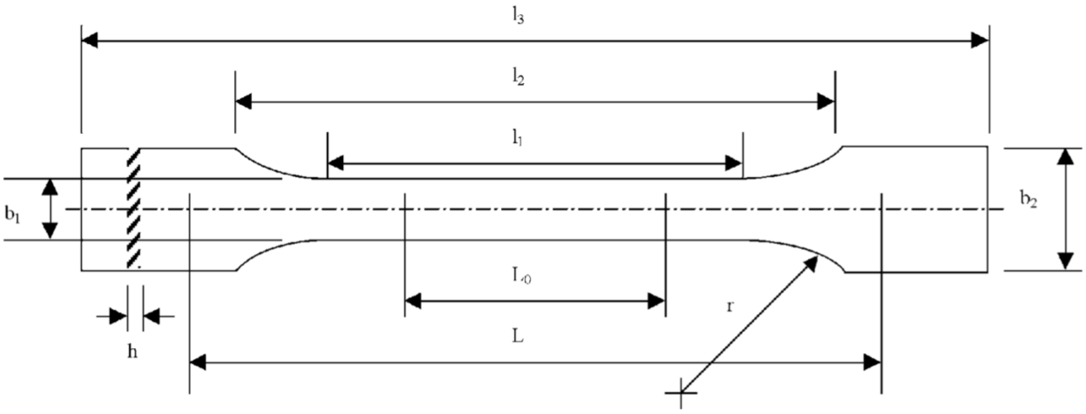

Figure 31 Dogbone specimen technical specification.

Table 7 Tensile test specimen specification.

	Type 1A (mm)	Type 1B (mm)
l_3	≥150	≥150
l_2	104 to 113	106 to 120
l_1	80 ± 2	60 ± 0.5
b_2	20 ± 0.2	20 ± 0.2
b_1	10 ± 0.2	10 ± 0.2
h	4.0 ± 0.2	4.0 ± 0.2
L_0	50.0 ± 0.5	50.0 ± 0.5
L	115.0 ± 1	$l_2 + 5$
r	20 to 25	≥60

The normative impose to test at least five specimens for each sample in the case of isotropic materials.

The test machine, through the dedicate software directly produce the curve of force-crosshead movement or the curve of force-deformation. In the deformation detection, since the specimen is not uniform (dogbone shaped), the stretching will not be uniform along the length of the specimen. As shown in the figure below, we can archive a correct result considering the central part of the dogbone, so to the reference points "A" and "B" of the representation below, setting a known "gage length." The gage length is not really fixed to a certain value, but it is a very important measure we must know accurately. As we will see later a longer gage length leads to more accurate results.

Always referring to the same figure, the specimen tip is held in the grip in turn attached to the fixed crosshead; the other tip (bottom) is pulled by the moving jaw. From the initial points, with the movement of the crossbar we arrive to the configuration of the point "A" and "C." The distance between points "A" to "C" need to be continuously measured to calculate the elongation, and so the strain, in every instant of the test, making possible to trace the curve.

Elongation = stretch (or extension) = $BC = AC - AB$

Tensile strain = elongation/gage length = $\frac{BC}{AB}$

Since BC and AB are both measured with the same units (millimeters or inches) the unity of strain is mm/mm or in./in.. This is however used in compressive testing, flexural testing, and shear testing while in tensile testing the results are typically expressed in per cent elongation:

Per cent elongation = 100 · tensile strain = 100 · $\frac{BC}{AB}$

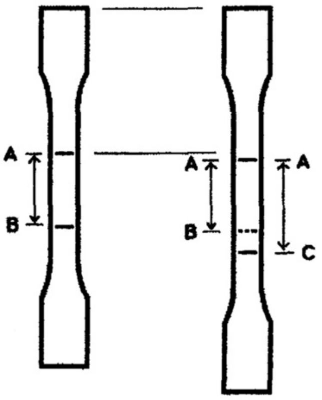

Figure 32 Specimen elongation during the tensile test.

Now for some more technical description we report a section of the ASTM D638-14 normative, to clarify some concept relative to the elaboration of the data.

We can calculate the tensile strength by dividing the maximum load sustained by the specimen in newtons, by the average original cross-sectional area in the gage length segment of the specimen in square meters. The result must be in pascals and report it to three significant figures as tensile strength at yield or tensile strength at break, which ever term is applicable. When a nominal yield or break load, lower than the maximum, is present and applicable, it is often desirable to also calculate, in a similar manner, the corresponding tensile stress at yield or tensile stress at break and report it to three significant figures.

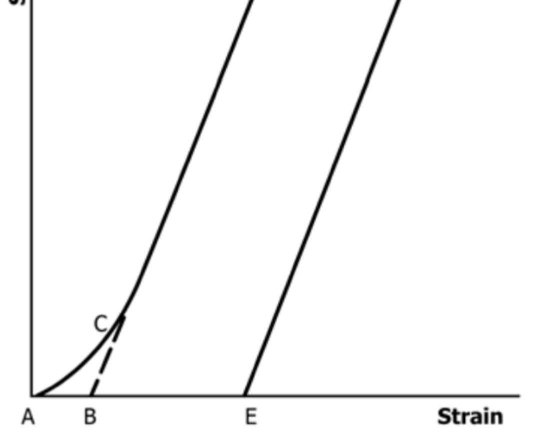

Figure 33 Typical polymeric material strain-stress curve.

To calculate the elastic modulus, we have to extend the initial linear portion of the load-extension curve (see figure 25 above) and dividing the difference in stress corresponding to any segment of section on this straight line by the corresponding difference in strain. All elastic modulus values shall be computed using the average original cross-sectional area in the gage length segment of the specimen in the calculations. The result shall be expressed in pascals (pounds- force per square inch) and reported to three significant figures. With the Matlab script was immediate for each series of tests, to calculate the arithmetic mean of all values obtained, reporting it as the "average value" for the particular property in question, also calculating the standard deviation (estimated) and report it to two significant figures as:

$$s = \sqrt{\frac{X^2 - n\overline{X^2}}{n-1}}$$

s = estimated standard deviation.
X = value of single observation.
n = number of observations.
$\overline{X}$ = arithmetic mean of the set of observations.

In a typical stress-strain curve (Figure 25) there is a so called "toe region", *AC*, that does not represent a property of the material. It is an artifact caused by a take-up of slack and alignment or seating of the specimen. In order to obtain correct values of such parameters as modulus, strain and offset yield point, this artifact must be compensated to give the corrected zero point on the strain or extension axis. In the case of a material exhibiting a region of Hookean (linear) behavior a continuation of the linear (*CD*) region of the curve is constructed through the zero-stress axis. This intersection (*B*) is the corrected zero-strain point from which all extensions or strains must be measured, including the yield offset (*BE*), if applicable. The elastic modulus can be determined by dividing the stress at any point along the line *CD* (or its extension) by the strain at the same point (measured from Point *B*, defined as zero-strain).

The data obtained by the test machine were collected in tables in the .txt format. To elaborate the data, as anticipated, we used a short Matlab script to import directly the tables and calculated directly the young modulus and the tensile strength for each specimen. The specimens were not all perfectly alike because of the production method, whose accuracy was limited by our human eye and so the thickness of the specimens may vary by some tenth of a millimeter. To avoid miscalculation each specimen's thickness was accurately measured with an electronic caliber and taken into consideration in the modulus calculation. For each specimen the data were corrected considering only the data acquired from 0.06 to 0.24 percent of deformation to be coherent with the theory.

In the next pages we report the obtained results.

The first data we have is the elastic modulus of the specimen filled with Mica10.

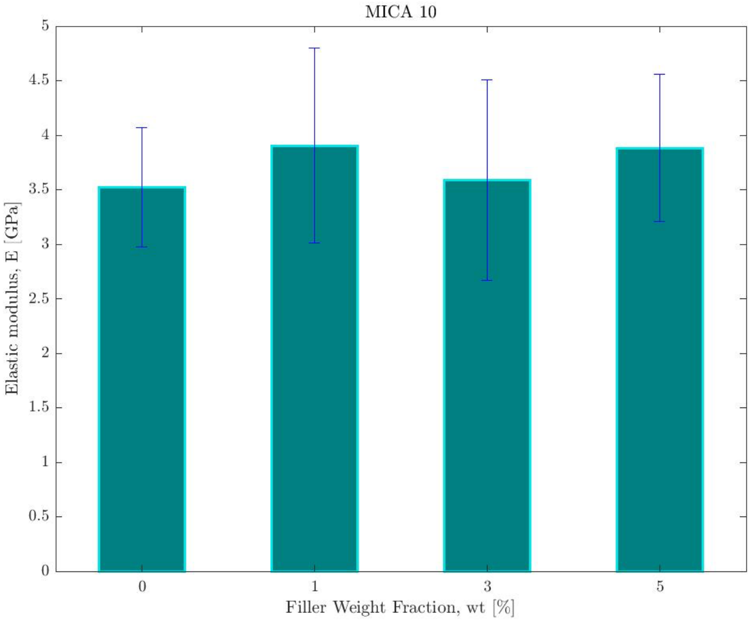

Figure 34 Elastic modulus of mica10 specimens.

The first column represents the value of the young modulus of neat epoxy specimen. In the other columns we find the modulus of the three sets of specimens filled with mica 10, ordered by percentage of filler weight fraction. The precise results are collected in the following table 7.

Table 8 Mica10 tensile test results.

Specimen	Average E [Pa]	Data covariance	Standard deviation
Neat epoxy	3.5239e+09	15.5110	5.4659e+08
1%	3.9044e+09	22.9277	8.9519e+08
3%	3.5848e+09	25.6451	9.1933e+08
5%	3.8828e+09	17.3691	7.7441e+08

We can notice that the average E has increased with the introduction of the filler, but the trend is not linear, in fact the 3% Mica filled specimens have a lower modulus than the 1% and the 5%. This result is not intuitive but follow with good accuracy what usually happen in similar experiments, as the previous one made in our laboratory. The script also provided some statistical data: the covariance, namely the interdependence between the two variable analyzed, and the standard deviation of the data.

As for mica10, we made the same analysis with mica45 filled specimens.

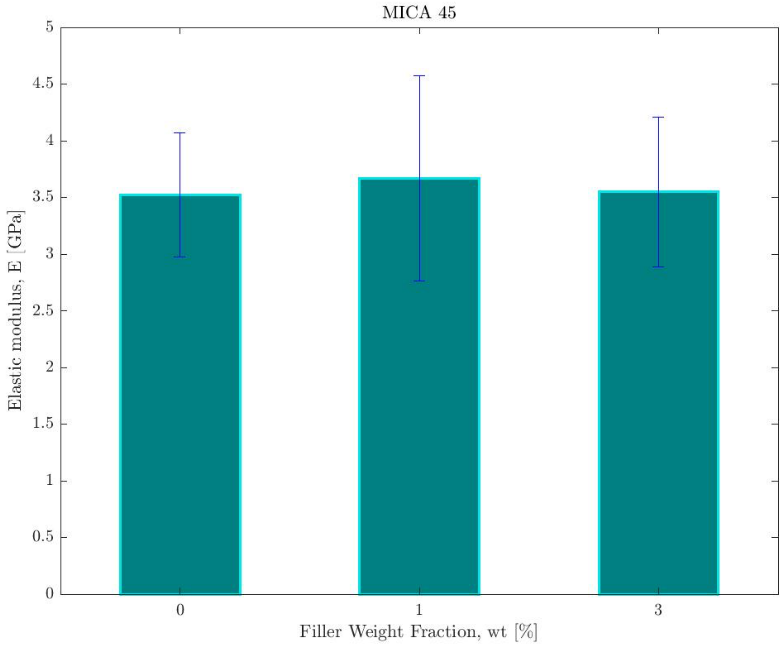

Figure 35 Elastic modulus of mica45 specimens.

The trend of the modulus value is the same that for the Mica 10 specimen. The column "0" represent the neat epoxy specimen. As before the precise values are collected in the table 8 below.

Table 9 Mica45 tensile test results.

Specimen	E [Pa]	Data covariance	Standard deviation
Neat epoxy	3.5239e+09	15.5110	5.4659e+08
1%	3.6679e+09	24.6399	9.0376e+08
3%	3.5482e+09	18.6461	6.6161e+08

Another parameter analyzed in the test is the tensile strength

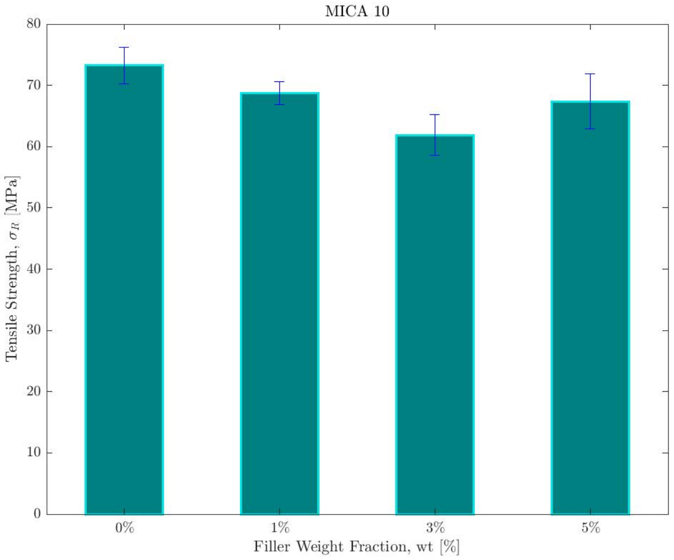

Figure 36 Tensile strenght in mica 10 specimens.

It is known that this type of nanofiller have a negative effect on the tensile strength and our data confirm the theory. The trend of the performance is the same as the young modulus trend, we reach the lowest value with the 3% mica specimen, while 1% and 5% have an almost equal value, slightly inferior to the neat epoxy specimen.

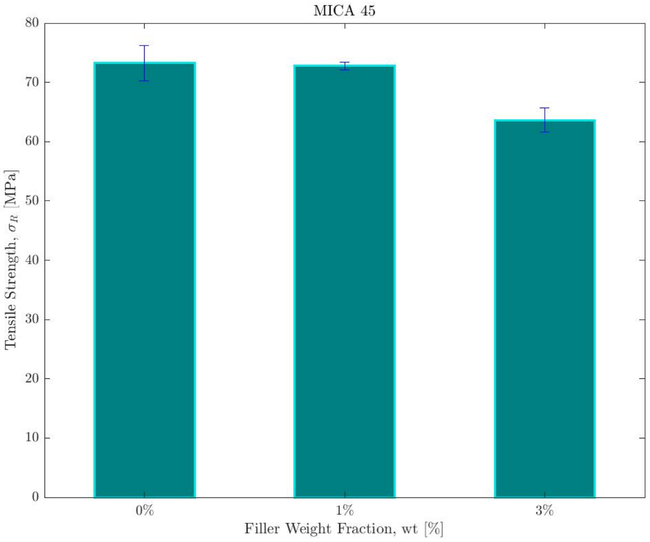

Figure 37 Tensile strenght in mica45 specimens.

The same analysis has been made for mica45. Also in this case the values have almost the same trend of the modulus, with no appreciable changes between 0% and 1% and a decreasing with the 3% charge.

The last result of this test is the strain stress curves. We computed 5 set of curves, one for each specimens set. In this way we have 5 curves in each graph, one for each specimen. The crossbar speed employed in all tests is 2mm/min.

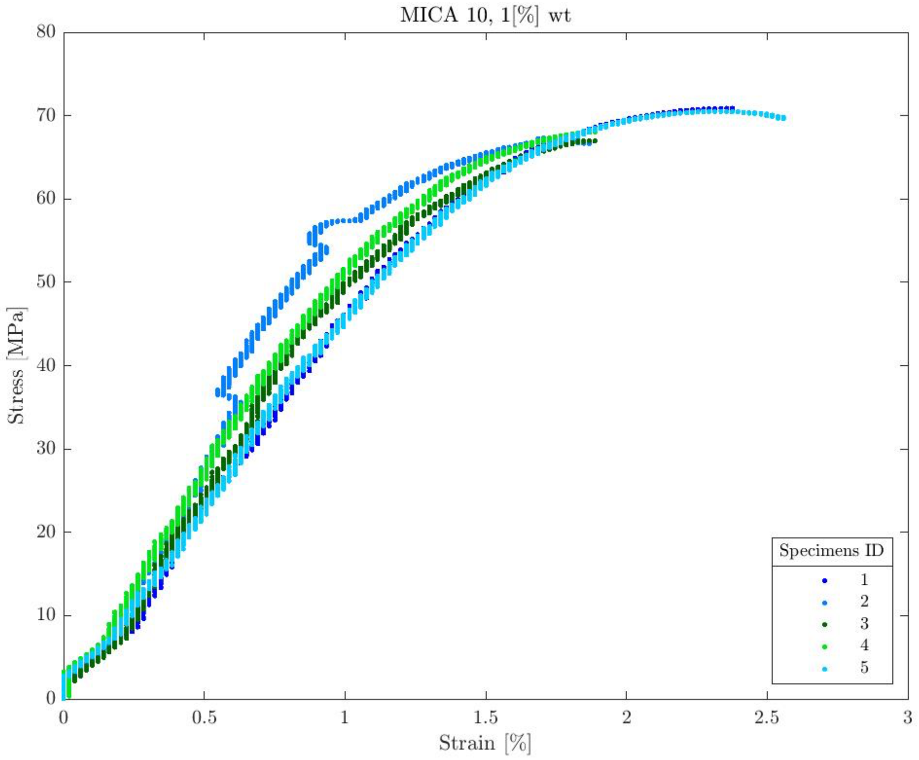

Figure 38 Mica10 1% strain-stress curves.

As we can see the shapes of the curves are really similar to the one showed in the normative, the irregular parts can be attributed to the slipping of the specimen inside the grasps of the machine.

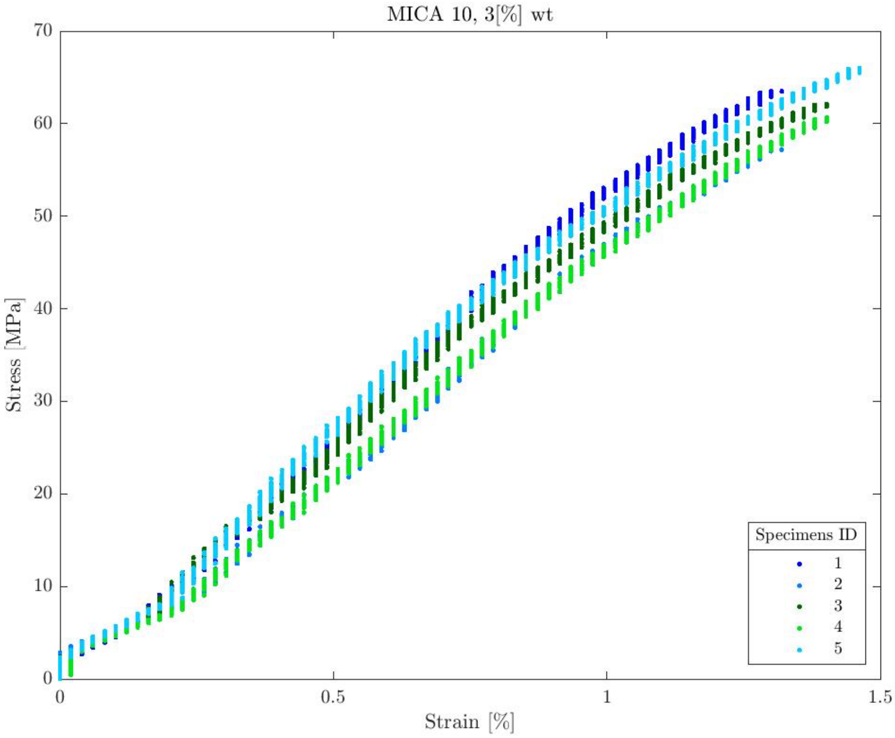

Figure 39 Mica10 3% strain-stress curves

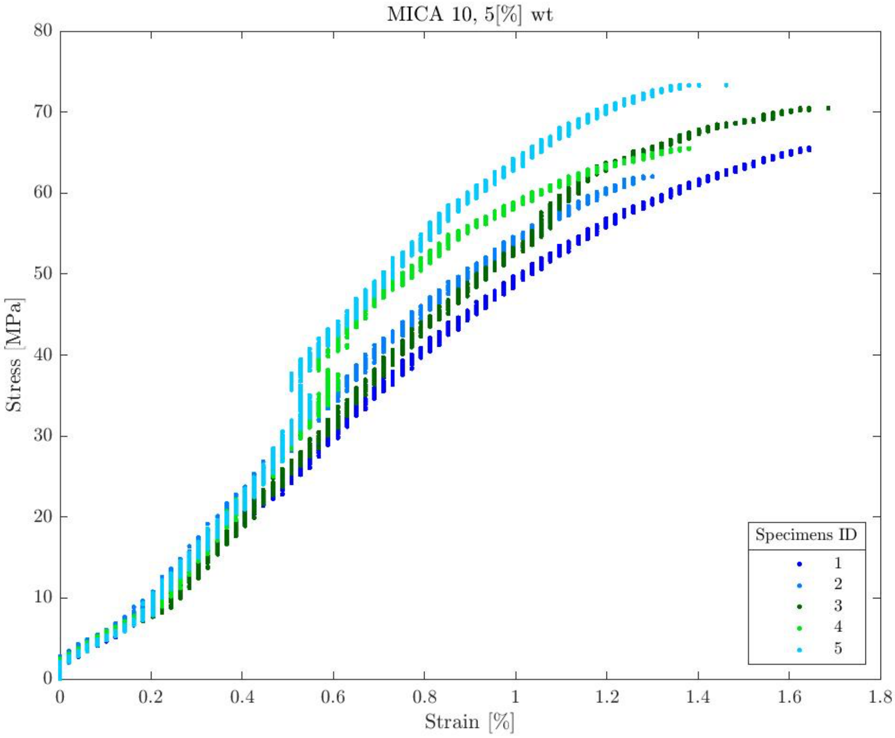

Figure 40 Mica10 5% strain-stress curves

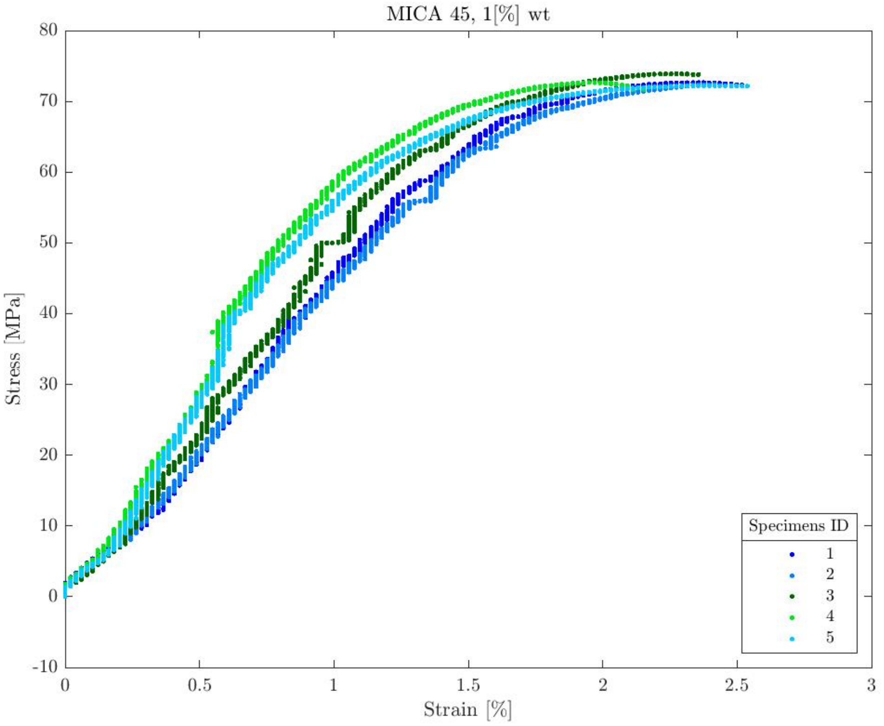

Figure 41 Mica45 1% strain-stress curves

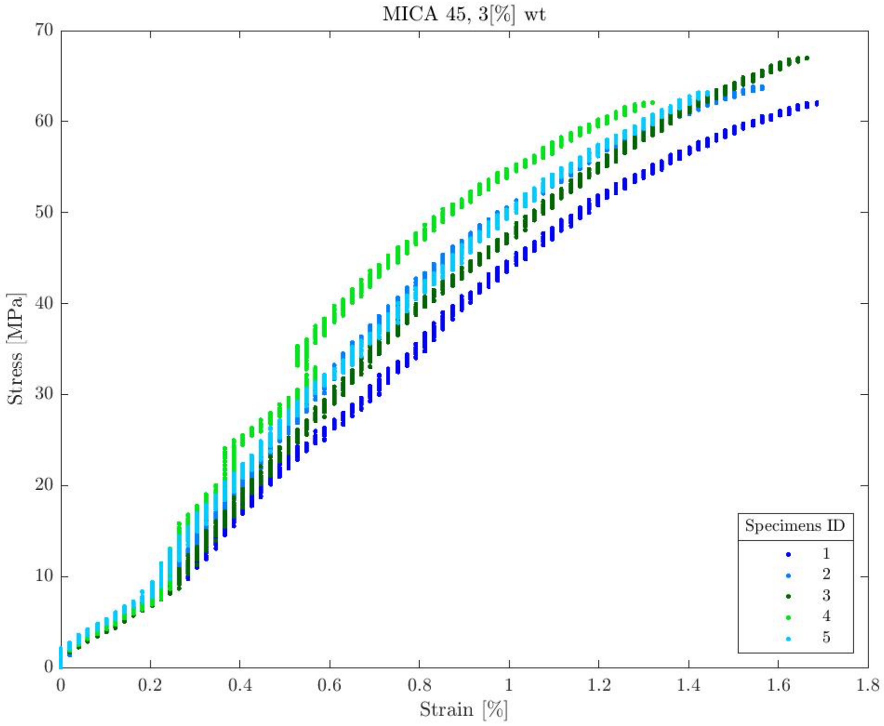

Figure 42 Mica45 3% strain-stress curves

3.2 Fracture test

In this section is reported the normative ASTM D5045 – 14, that describe the standard test methods for plane-strain fracture toughness and strain energy release rate of plastic materials. These test methods are designed to characterize the toughness of plastics in terms of the critical-stress-intensity factor, K_{IC}, and the energy per unit area of crack surface or critical strain energy release rate, G_{IC}, at fracture initiation. Two testing geometries are covered by these test methods, single-edge-notch bending (SENB) and compact tension (CT). In our test we have chosen the last one. The scheme used assumes linear elastic behavior of the cracked specimen, so certain restrictions on linearity of the load-displacement diagram are imposed. A state-of-plane strain at the crack tip is required and the specimen thickness must be sufficient to ensure this stress state. The crack must be sufficiently sharp to ensure that a minimum value of toughness is obtained. The significance of these test methods and many conditions of testing are identical to those of Test Method E399 (for metallic material), and, therefore, in most cases, appear here with many similarities to the metal's standard. However, certain conditions and specifications not covered in this normative, but important for plastics, are included. This protocol covers the determination of G_{IC} as well, which is of particular importance for plastics. These test methods give general information concerning the requirements for K_{IC} and G_{IC} testing. As with Test Method E399, two annexes are provided in the complete normative description which give the specific requirements for testing SENB and CT geometries. Test data obtained by these test methods are relevant and appropriate for the use in engineering design.

These test methods consist in the loading a notched specimen that has been pre-cracked, in either tension or three-point bending. The load corresponding to a 2.5 % apparent increment of crack extension is established by a specified deviation from the linear portion of the record. The K_{Ic} value is calculated from this load by equations that have been established on the basis of elastic stress analysis on specimens. The validity of the determination of the K_{Ic} value by these test methods depends upon the establishment of a sharp-crack condition at the tip of the crack, in a specimen of adequate size, to give linear elastic behavior. To obtain the value of G_{Ic} it is necessary the determination of the energy derived from the integration of the load versus load-point displacement diagram, while making a correction for indentation at the loading points as well as specimen compression and system compliance.

The property K_{Ic} (and G_{Ic}) determined by these test methods characterizes the resistance of a material to fracture in a neutral environment, in the presence of a sharp crack under severe tensile constraint, such that the state of stress near the crack front approaches plane strain, and the crack-tip plastic (or non-linear viscoelastic) region is small compared with the crack size and specimen dimensions in the constraint direction. A K_{Ic} value is believed to represent a lower limiting value of fracture toughness. This value has been used to estimate the relation between failure stress and defect size for a material in service wherein the conditions of high constraint described above would be expected. The K_{Ic} value of a given material is a function of testing speed and temperature. Furthermore, cyclic loads have been found to cause crack extension at K values less than K_{Ic}. Crack extension under cyclic or sustained load will be increased by the presence of an aggressive environment. Therefore, application of K_{Ic} in the design of service components should be made considering differences that may exist between laboratory tests and field conditions. Plane-strain fracture toughness testing is unusual in that sometimes there is no advance assurance that a valid K_{Ic} will be determined in a particular test. Therefore, it is essential that all of the criteria concerning validity of results be carefully considered as described herein. Clearly, it will not be possible to determine K_{Ic} and G_{Ic} if any dimension of the available stock of a material is insufficient to provide a specimen of the required size. In as much as the fracture toughness of plastics is often dependent on specimen process history, the specimen crack orientation (parallel or perpendicular) relative to any processing direction shall be noted on the report. Before proceeding with this test method, reference should be made to the specification of the material being tested. Any test specimen preparation, conditioning, dimensions, or testing parameters, or combination thereof, covered in the relevant ASTM materials specification, shall take precedence over those mentioned in this test method. If there are no relevant ASTM material specifications, then the default conditions apply.

A constant displacement-rate device shall be used such as an electromechanical, screw-driven machine, or a closed loop, feedback-controlled servo-hydraulic load frame. A loading clevis suitable for loading compact tension specimens is shown in figure 35. Loading is possible by means of pins in the specimen holes. An accurate displacement measurement must be obtained to assure accuracy of the G_{Ic} value. For either specimen configurations, the displacement measurement shall be performed using the machine's stroke (position) transducer. The fracture-test-displacement data must be corrected for system compliance, loading-pin penetration (brinelling) and specimen compression by performing a calibration of the testing system. For CT specimens, a clip gauge shall be mounted across the loading pins.

As we anticipated before, for both the SENB an CT geometry, the specimens need to be prepared practicing a sharp notch by machining. Subsequently, a natural crack is initiated by inserting a fresh razor blade and tapping. If a natural crack cannot be successfully initiated by tapping, a sufficiently sharp crack shall alternatively be generated by sliding or sawing a new razor blade across the notch root. The depth of the natural crack generated by tapping must be at least two times longer than the width of the sawed-in slot or the machined notch tip radius The total depth of the notch obtained by machining and the generation of the natural crack is the crack length, a.

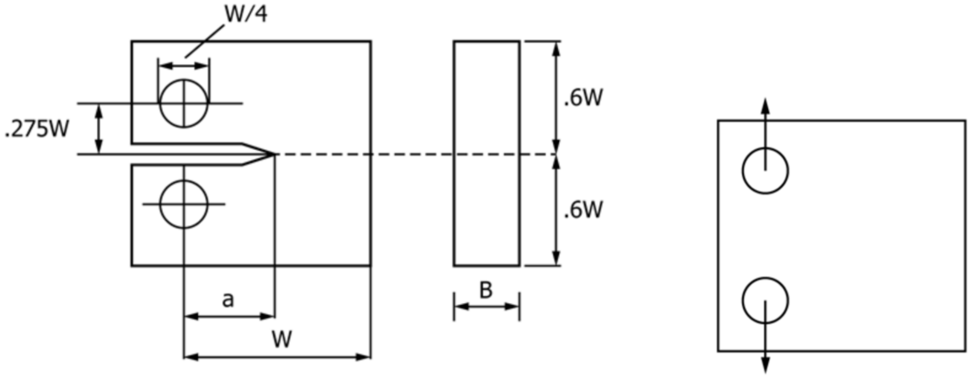

Figure 43 CT specimens' technical specification.

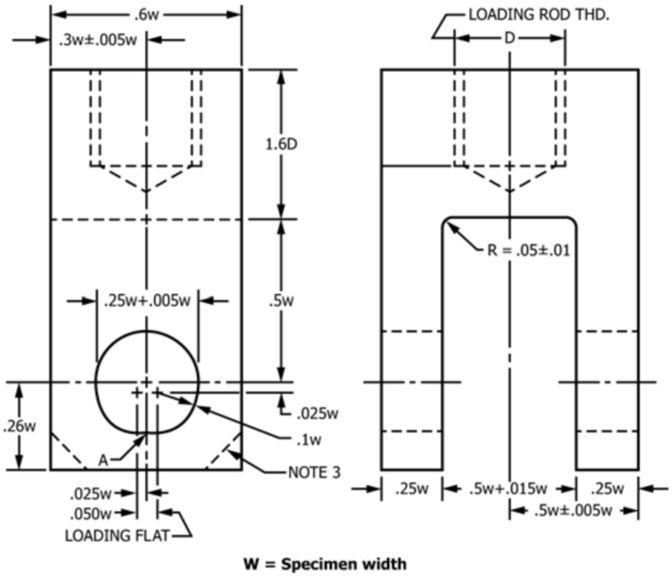

Figure 44 CT specimen loading clevis.

It is recommended that at least three replicate tests have to be performed, for each material condition. Specimen dimensions shall conform to those shown in figure 36. Three fundamental measurements are necessary for the calculation of K_{Ic} and G_{Ic}, namely, the thickness, B, the crack length, a, and the width W. Measure the thickness, B, to 0.1 % accuracy at not less than three positions. Record the average of these three measurements as B. Measure the crack length a, after fracture to the nearest 0.5 % accuracy at the following three positions: at the center of the crack front, and the end of the crack front on each surface of the specimen. Use the average of these three measurements as the crack length, a. Measure the width, W, to within 0.1 % as described in the annex appropriate to the specimen type being tested. Since plastics are viscoelastic materials, it is necessary to specify both the temperature and time scale under which the result was obtained. As a basic test condition, it is recommended that a temperature of 23°C, and a crosshead rate of 1.67×10^{-4} m/s (10 mm/min) be used. Record both loading rate and loading time on the report form. It is recommended that speeds greater than 1 m/s or loading times less than 1 ms should be avoided because of the risk of dynamic effects causing errors, by the way our test were performed with a speed of 2 mm/s, for coherence with other previous tests. When the test is performed and the load versus loading-point displacement curve is obtained, the ideal case is a linear diagram with an abrupt drop of load to zero at the instant of crack growth initiation. In some cases, this occurs and K_Q shall be determined from the maximum load. G_{Ic} is determined as specified before, which necessitates an accurate displacement determination using a displacement transducer. A cross check on the accuracy of G_{Ic} is provided through a corrected compliance parameter.

To establish that a valid K_{Ic} has been determined, it is first necessary to calculate a conditional result, K_Q, which involves a construction on the test record, and to then determine whether this result is consistent with the size of the specimen. Load the specimen and obtain a diagram as shown in figure 37.

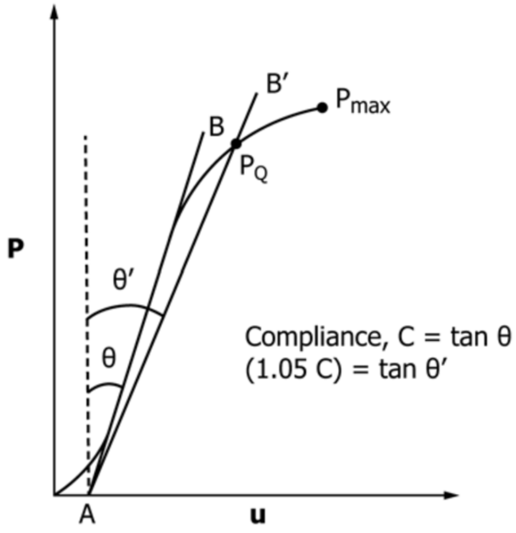

Figure 45 Determination of C and P_Q.

Draw a best straight line (AB) to determine the initial compliance, C, which is given by the reciprocal of the slope of line (AB). Draw a second line (AB') with a compliance 5 % greater than that of line (AB). If the maximum load that the specimen was able to sustain, $P_{\max}$, falls within lines (AB) and (AB'), use $P_{\max}$ to calculate K_Q. If $P_{\max}$ falls outside line (AB) and line (AB'), then use the intersection of line (AB') and the load curve as P_Q. Furthermore, if $\frac{P_{max}}{P_Q} < 1.1$, use P_Q in the calculation of K_Q, while if $\frac{P_{max}}{P_Q} > 1.1$, the test is invalid. For the calculation, a value of a, which is the total crack length after both notching and pre-cracking, but before fracture, is best determined from the fracture surface after testing. An average value is used, but the difference between the shortest and longest length should not exceed 10 %. Take care that it is the original crack which is being observed, since slow growth can occur prior to catastrophic fast fracture. Check the validity of K_Q via the size criteria. Calculate $2.5(\frac{K_Q}{\sigma_y})^2$ where σ_y is the yield stress. If this quantity is less than the specimen thickness, B, the crack length, a, and the ligament $(W - a)$, K_Q is equal to K_{Ic}. Otherwise, the test is not a valid K_{Ic} test. For the recommended specimen dimensions of $W = 2B$

and $\frac{a}{W} = 0.5$, all the relationships we specified in the previous lines are satisfied simultaneously. In fact, the criterion covers two limitations in that B must be sufficient to ensure plane strain, but $(W - a)$ has to be sufficient to avoid excessive plasticity in the ligament. If $(W - a)$ is too small the test will often violate the linearity criteria. If the linearity criterion is violated, a possible option is to increase W for the same $\frac{a}{W}$ and $\frac{S}{W}$ ratios. Values of $\frac{W}{B}$ of up to 4 are permitted. If the test result fails to meet the requirements, it will be necessary to use a larger specimen to determine K_Q. Make a displacement correction for system compliance, loading-pin penetration, and specimen compression, then calculate G_{Ic} from the energy derived from integration of the load versus load-point displacement curve.

The procedure for obtaining the corrected displacement, $u_C(P)$, at load P from the measured displacement, $u_Q\ (P)$, include the use of an uncracked correction specimen prepared from the same material as that being tested. Using the same testing parameters as the actual test, load the specimen to a point at or above the fracture loads observed during actual testing. From the load-displacement curve, determine $u_i(P)$. The corrected displacement is then calculated using $u_C(P) = u_Q(P) - u_i(P)$ for both the specimens' geometries. In practice, it is common to obtain a linear displacement correction curve (up to the fracture loads observed during actual testing). This simplifies the displacement correction to be applied to the fracture test. Initial non-linearity due to penetration of the loading pins into the specimen usually occur during both the calibration test and the actual fracture test. Linearization of the near-zero correction data and the fracture test data can compensate for this initial nonlinearity. The displacement correction must be performed for each material and at each test temperature or rate. Polymers are generally temperature and rate sensitive and the degree of loading-pin penetration and sample compression have been found to vary with changes in these variables. Perform indentation tests in such a way that the loading times are the same as the fracture tests. Since the indentations are stiffer, this will involve lower rates to reach the same loads. In principle, G_{Ic} can be obtained as:

$$G_{Ic} = \frac{(1-\upsilon^2){K_{Ic}}^2}{E}$$

but for plastics, E must be obtained at the same time and temperature conditions as the fracture test because of viscoelastic effects. Many uncertainties are introduced by this procedure and it is considered preferable to determine G_{Ic} directly from the energy derived from integration of the load versus displacement curve up to the same load point as used for K_{Ic} and shown in figure 38.

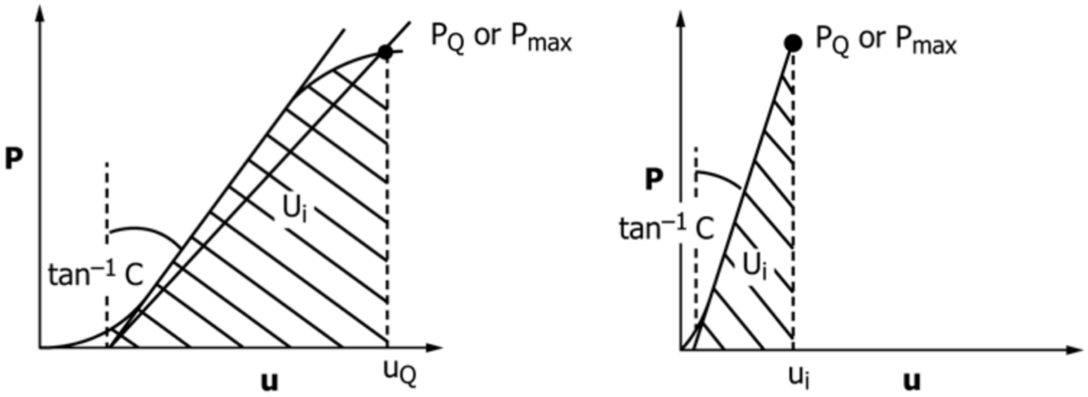

Figure 46 Method of correcting for indentation: deflection in fracture test (left) and deflection in indentation (right).

The energy must be corrected for system compliance, loading-pin penetration, and specimen compression. This is done by correcting the measured displacement values, as shown in the graphs in figure 38. Accordingly, if complete linearity is obtained, one form of the integration for energy is as $U = \frac{1}{2} P_Q[u_Q - u_i]$.

Alternatively, it is possible to use the integrated areas from the measured curve, U_Q, of figure 38 (left) and indentation curves, U_i, (right) in accordance with $U = U_Q - U_i$. With the result obtained, we can now calculate G_Q from U in accordance with the procedure given before.

Now we take a look to the annex of the normative relative to the CT specimens, (skipping the SENB annex).

The standard compact-tension specimen is a single edge-notched plate loaded in tension. The general proportions of this specimen configuration are shown in figure 35. Alternative specimens having the proportion $2 \leq \frac{W}{B} \leq 4$ but with no change in other proportions are acceptable. For generally applicable specifications concerning specimen size and preparation. Both ends of the specimen are held in such a clevis and loaded through pins, in order to permit rotation of the specimen during testing. To provide rolling contact between the loading pins and the clevis holes, these holes are provided with small flats on the loading surfaces. Other clevis designs may be used if it can be demonstrated that they will accomplish the same result as the design shown. These proportions are based on specimens having $\frac{W}{B} = 2$ for $B > 12.7$ mm and $\frac{W}{B} = 4$ for $B < 12.7$ mm.

Achieving as good alignment as possible through careful machining of all auxiliary gripping fixtures is a critical aspect of this test. For a compact-tension specimen measure the width, W, and the crack length, a, from the plane of the centerline of the loading holes (the notched edge is a convenient reference line, but the distance from the centerline of the holes to the notched edge must be subtracted to determine W and a). Measure the width, W, to the nearest 0.025 mm, at not less than three positions near the notch location and record the average value. When assembling the loading train (clevises and their attachments to the tensile machine) we must take care to minimize eccentricity of loading due to misalignments external to the clevises. To obtain satisfactory alignment keep the centerline of the upper and lower loading rods coincident within 0.76 mm during the test and center the specimen with respect to the clevis opening within 0.76 mm.

We can calculate the K_Q in units of MPa·m$^{0.5}$ from the expression:

$$K_Q = (\frac{P_Q}{BW^{0.5}}) \cdot f\ (x)$$

where $(0.2 < x < 0.8)$ and

$$f\ (x) = \frac{(2 + \mathrm{x})(0.886 + 4.64\mathrm{x} - 13.32x^2 + 14.72x^3 - 5.6x^4)}{(1 - x)^{1.5}}$$

where:

P_Q = load
B = specimen thickness
W = specimen width
a = crack length
x = $\frac{a}{W}$

And the value of $f\ (x)$ is given in the table below

For the compact tension specimen, we can calculate G_Q in units of kJ/m^2 from the corrected energy, U, as follows:

$$G_Q = \left(\frac{U}{BW_{\varphi}}\right) = \frac{U\eta_e}{[B(W-a)]}$$

Where the energy-calibration factor, φ, shall be computed from:

$$\varphi = \frac{(1.9118 + 19.118x - 2.5122x^2 - 23.226x^3 + 20.54x^4)(1-x)}{\begin{gathered}(19.118 - 5.0244x - 69.678x^2 + 82.16x^3)(1-x) + \\ 2(1.9118 + 19.118x - 2.5122x^2 - 23.226x^3 + 20.54x^4\end{gathered}}$$

and the values of φ and η_e are given in the table below.

Table 10 Calibration factors for CT specimens.

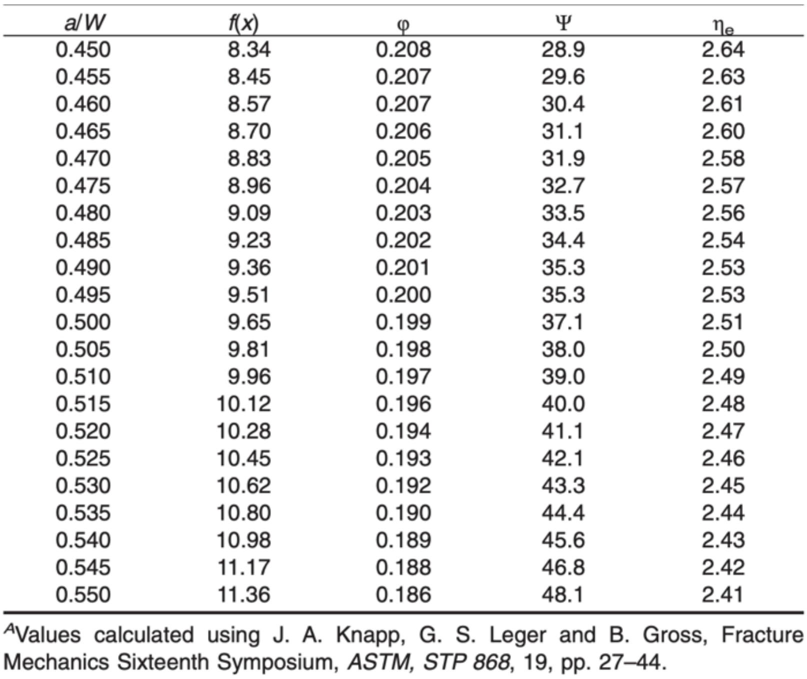

a/W	f(x)	φ	Ψ	η_e
0.450	8.34	0.208	28.9	2.64
0.455	8.45	0.207	29.6	2.63
0.460	8.57	0.207	30.4	2.61
0.465	8.70	0.206	31.1	2.60
0.470	8.83	0.205	31.9	2.58
0.475	8.96	0.204	32.7	2.57
0.480	9.09	0.203	33.5	2.56
0.485	9.23	0.202	34.4	2.54
0.490	9.36	0.201	35.3	2.53
0.495	9.51	0.200	35.3	2.53
0.500	9.65	0.199	37.1	2.51
0.505	9.81	0.198	38.0	2.50
0.510	9.96	0.197	39.0	2.49
0.515	10.12	0.196	40.0	2.48
0.520	10.28	0.194	41.1	2.47
0.525	10.45	0.193	42.1	2.46
0.530	10.62	0.192	43.3	2.45
0.535	10.80	0.190	44.4	2.44
0.540	10.98	0.189	45.6	2.43
0.545	11.17	0.188	46.8	2.42
0.550	11.36	0.186	48.1	2.41

[A] Values calculated using J. A. Knapp, G. S. Leger and B. Gross, Fracture Mechanics Sixteenth Symposium, *ASTM, STP 868*, 19, pp. 27–44.

As for the tensile test, also here the results were given by the laboratory in a table, this time in the Microsoft Excel format. The results have been elaborated as described by the normative, always with the aid of a MATLAB script.

The first interesting outcome of the analysis is the motor position versus load graphs of the fracture test. In the graphs, in the x-axis we have the engine stroke so a reference to how the pin inserted in the specimen has moved, expressed in mm, while in the y-axis we have the applied load, expressed in N. These graphs are almost all equal, with exception for two specimens, and consists in a big peak followed by one or more small peaks. In the exceptions (2nd mica10 1%, 4th mica45 1% and the 2nd mica45 3%) there is only one peak.

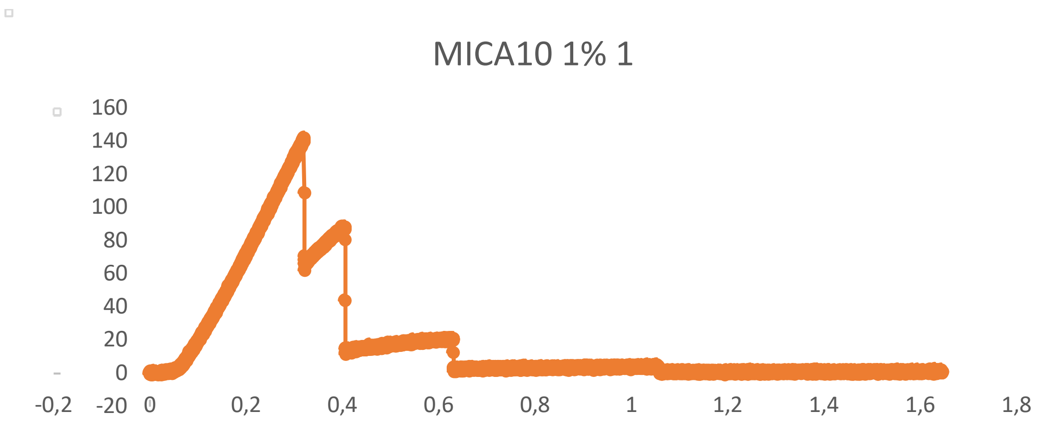

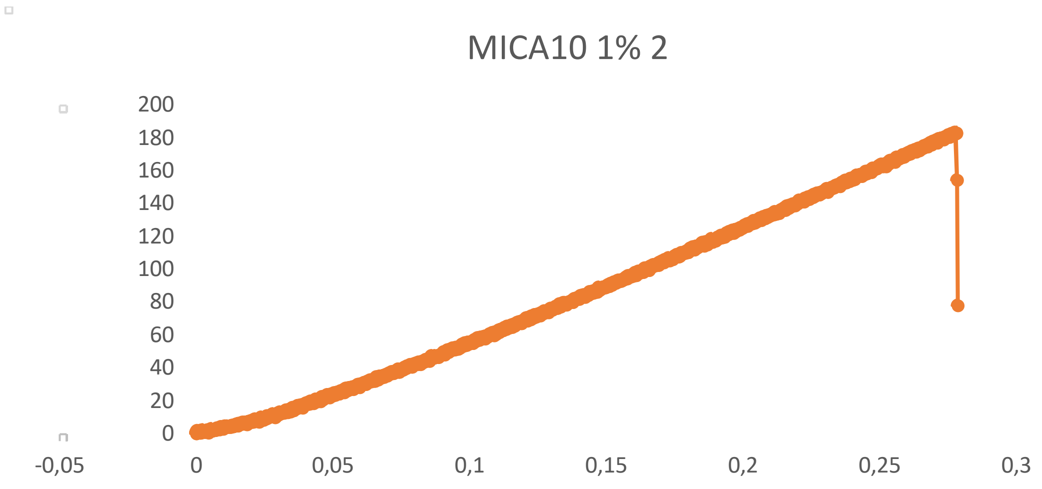

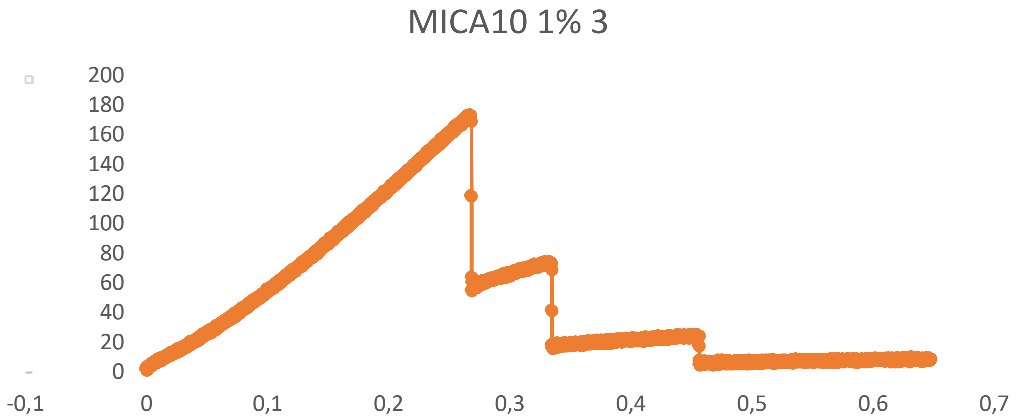
MICA10 1% 3

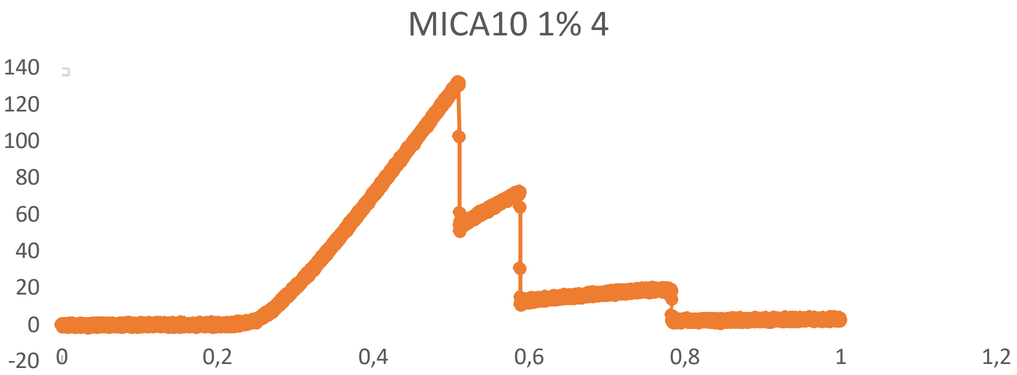
MICA10 1% 4

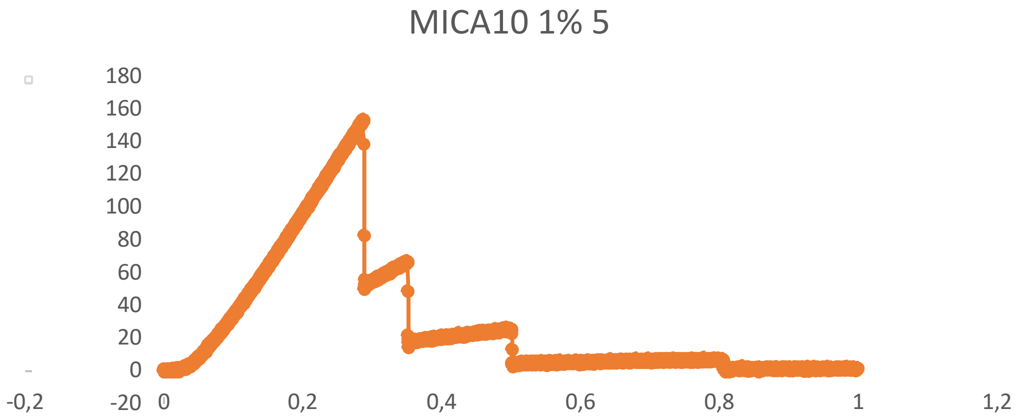
MICA10 1% 5

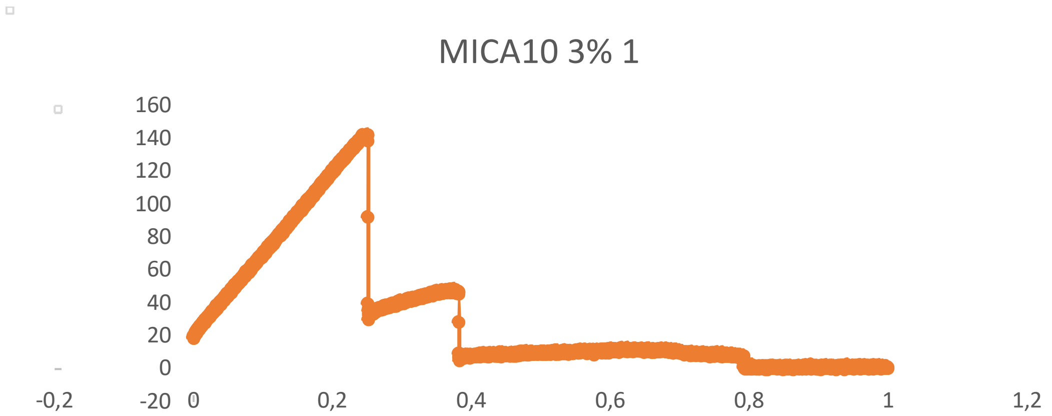
MICA10 3% 1
160
140
120
100
80
60
40
20
0
-20
-0,2
0
0,2
0,4
0,6
0,8
1
1,2

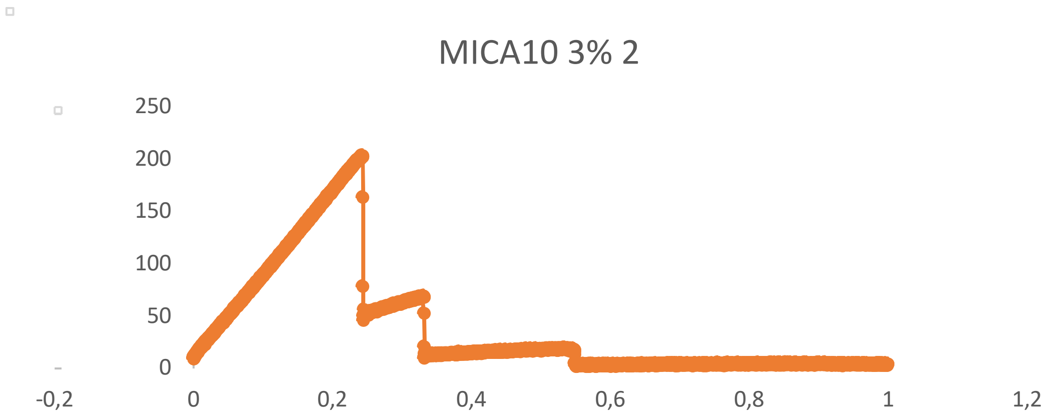
MICA10 3% 2
250
200
150
100
50
0
-0,2
0
0,2
0,4
0,6
0,8
1
1,2

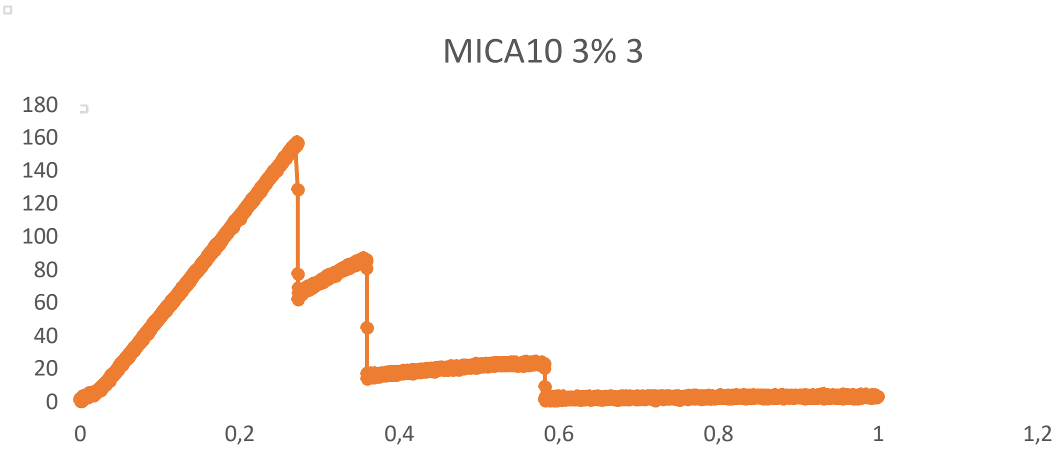
MICA10 3% 3
180
160
140
120
100
80
60
40
20
0
0
0,2
0,4
0,6
0,8
1
1,2

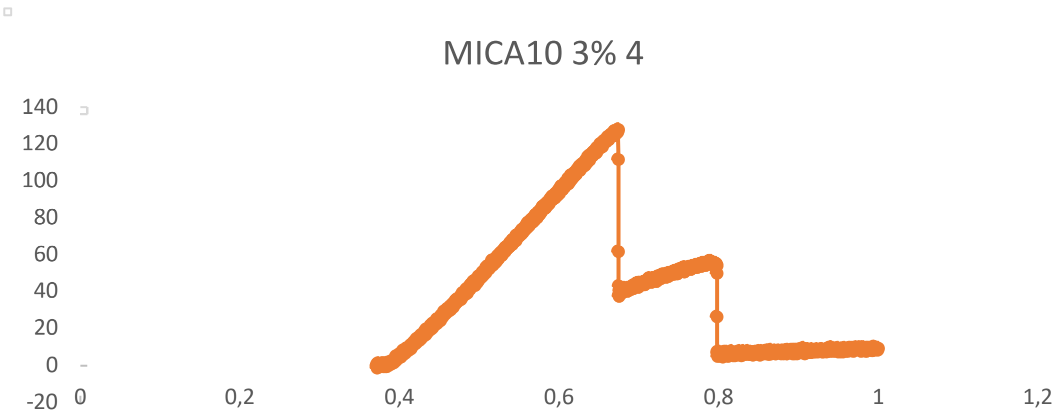
MICA10 3% 4
140
120
100
80
60
40
20
0
-20
0
0,2
0,4
0,6
0,8
1
1,2

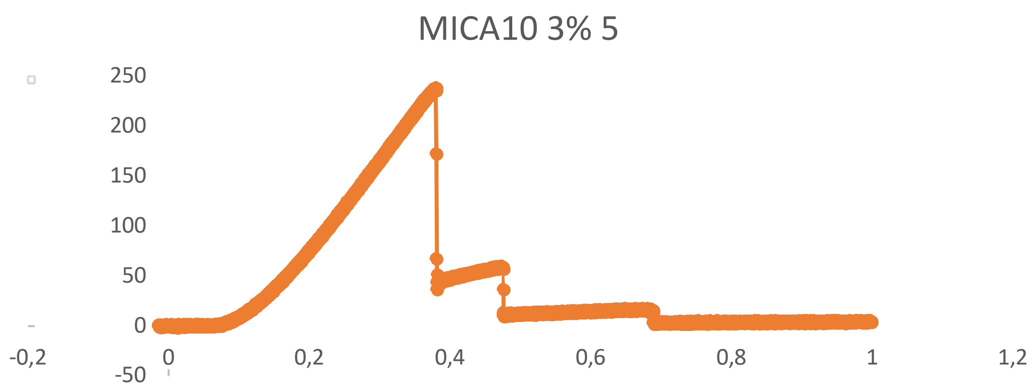
MICA10 3% 5

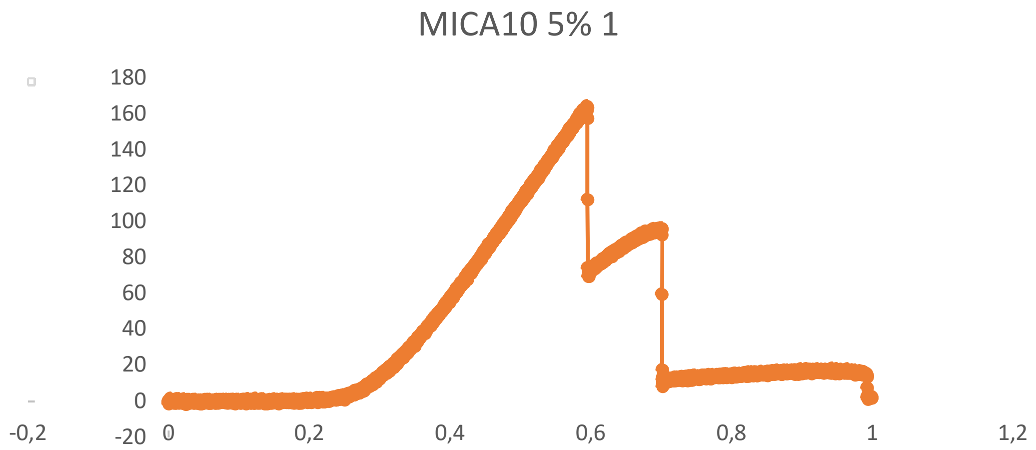
MICA10 5% 1

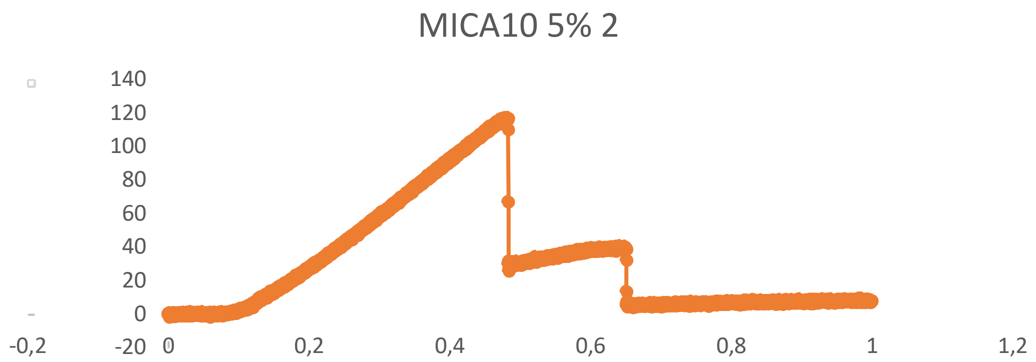
MICA10 5% 2

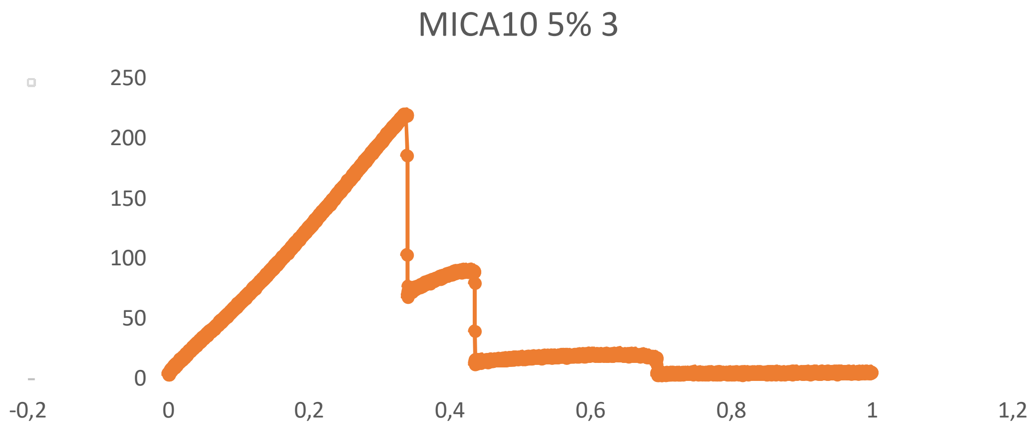
MICA10 5% 3

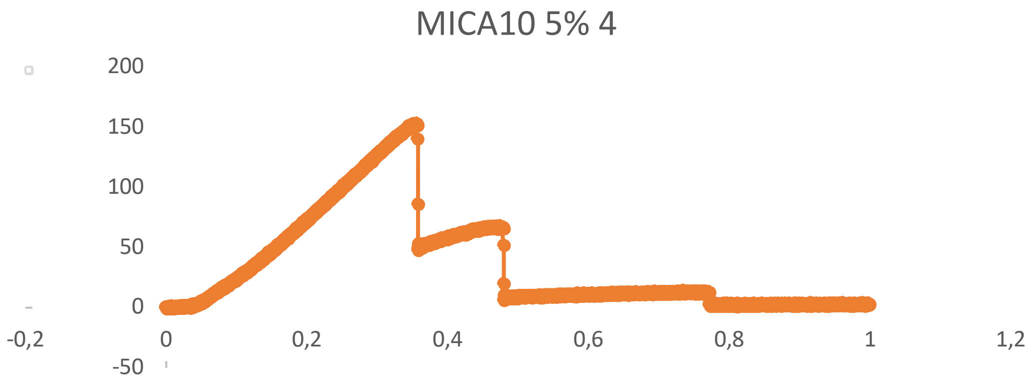
MICA10 5% 4
200
150
100
50
0
-50
-0,2
0
0,2
0,4
0,6
0,8
1
1,2

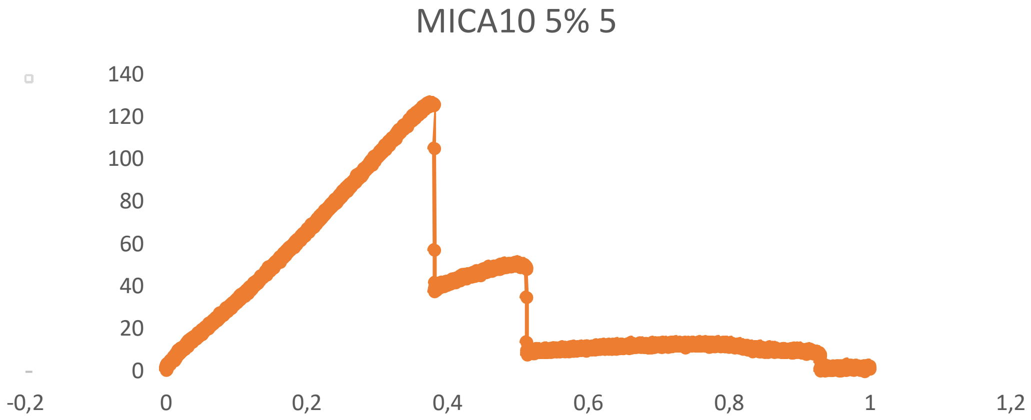
MICA10 5% 5
140
120
100
80
60
40
20
0
-0,2
0
0,2
0,4
0,6
0,8
1
1,2

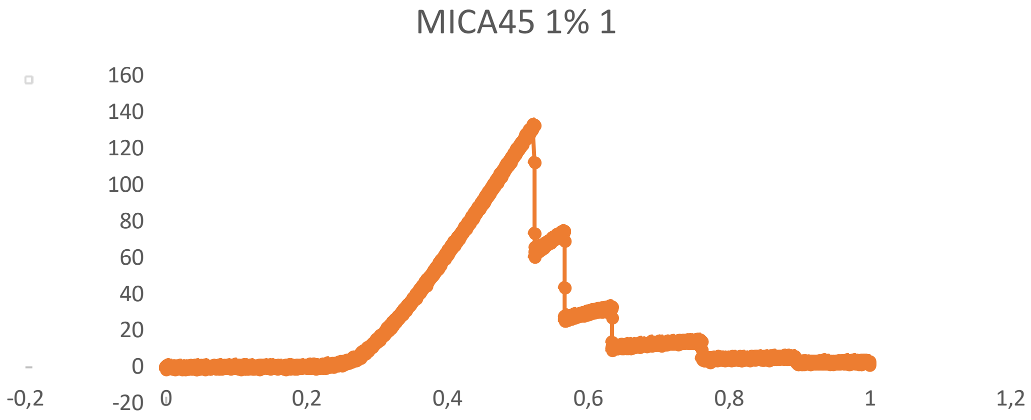
MICA45 1% 1
160
140
120
100
80
60
40
20
0
-20
-0,2
0
0,2
0,4
0,6
0,8
1
1,2

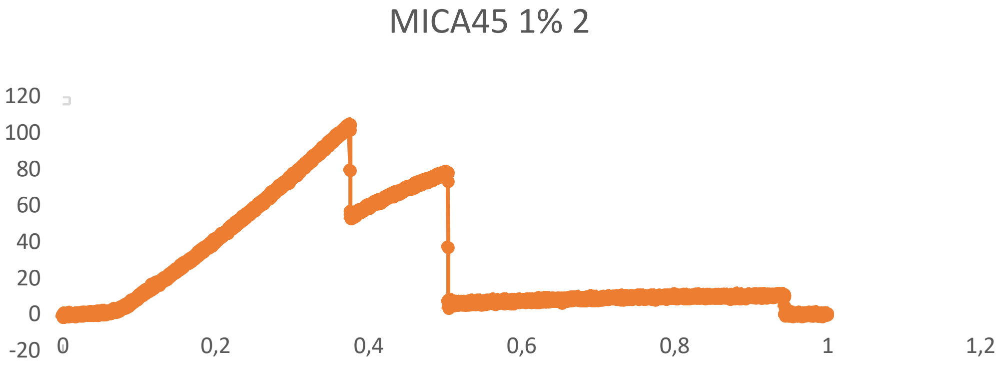
MICA45 1% 2
120
100
80
60
40
20
0
-20
0
0,2
0,4
0,6
0,8
1
1,2

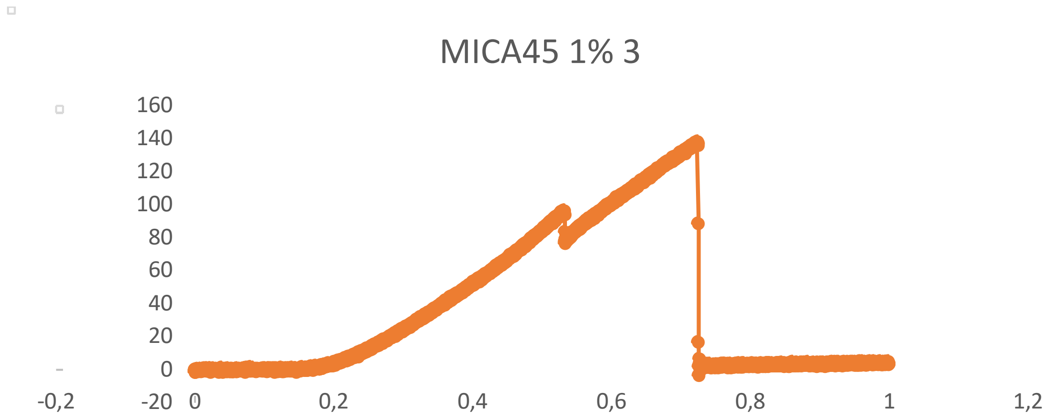
MICA45 1% 3
160
140
120
100
80
60
40
20
0
-20
-0,2
0
0,2
0,4
0,6
0,8
1
1,2

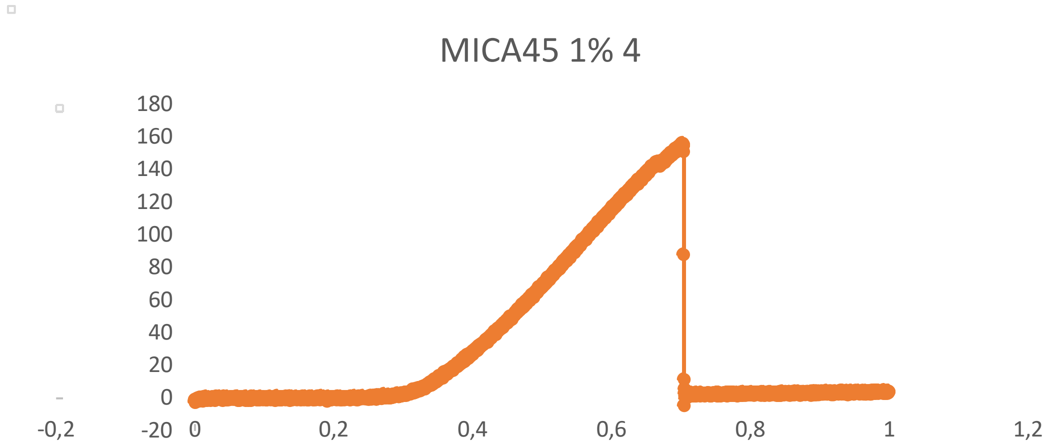
MICA45 1% 4
180
160
140
120
100
80
60
40
20
0
-20
-0,2
0
0,2
0,4
0,6
0,8
1
1,2

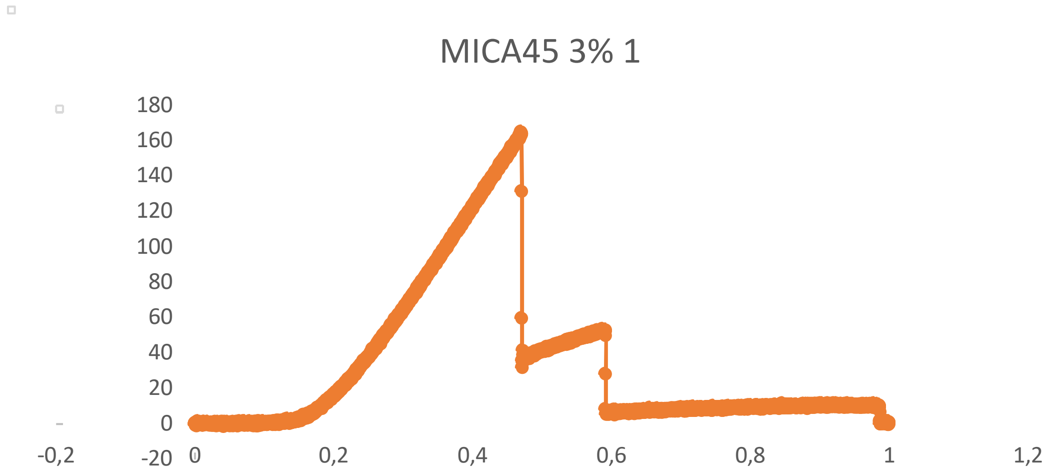
MICA45 3% 1
180
160
140
120
100
80
60
40
20
0
-20
-0,2
0
0,2
0,4
0,6
0,8
1
1,2

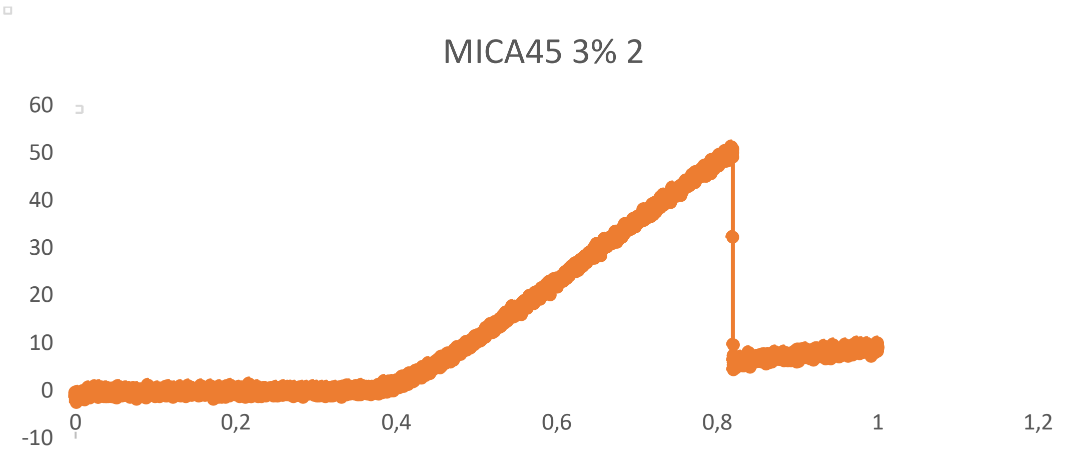
MICA45 3% 2
60
50
40
30
20
10
0
-10
0
0,2
0,4
0,6
0,8
1
1,2

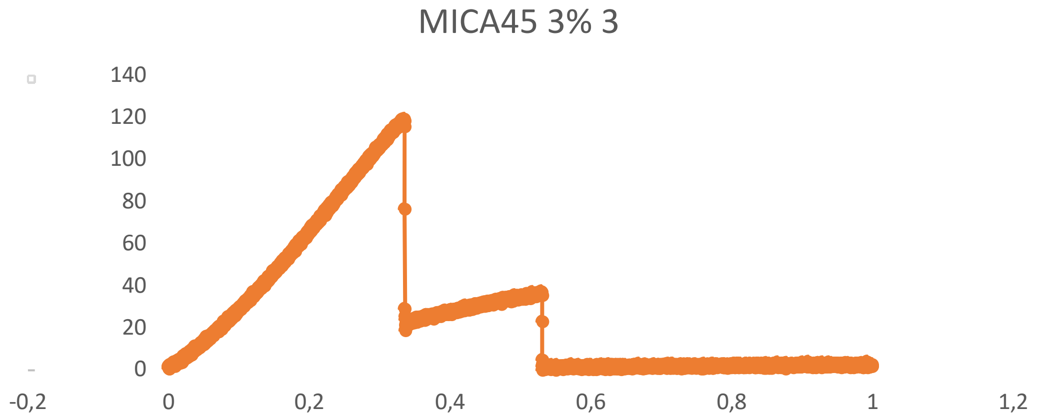
MICA45 3% 3
140
120
100
80
60
40
20
0
-0,2
0
0,2
0,4
0,6
0,8
1
1,2

Here we report some ESEM images of the fracture surface in mica10 5% specimen.

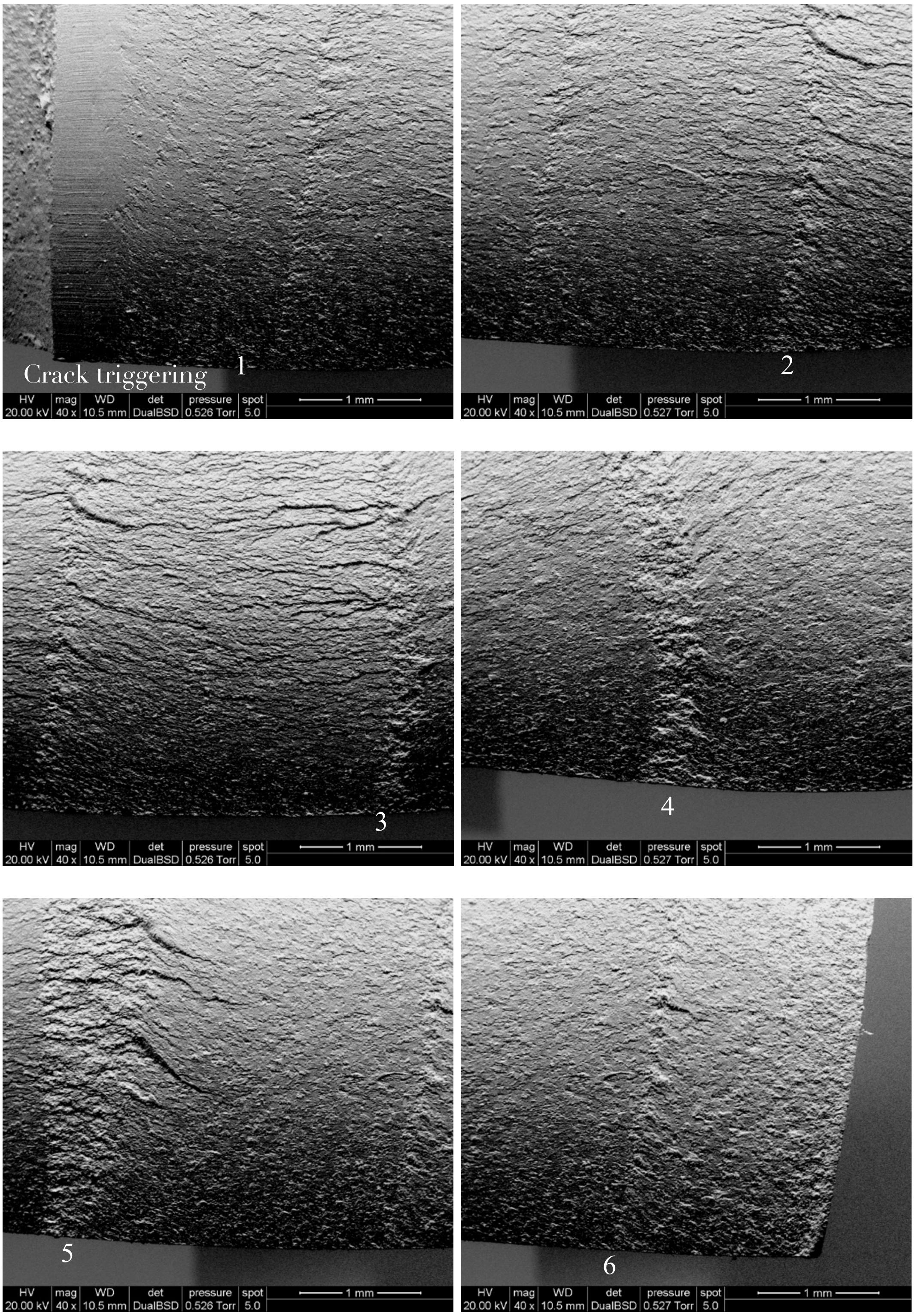

Figure 47 ESEM images of the fracture sequence on a mica10 5% specimen. The numbers correspond to the various wavefront on the same specimen.

An important value analyzed in this test is the fraction toughness, so the parameter K_{Ic}, introduced at the beginning of this paragraph. As always, the results are collected in two graphs, one for each mica type.

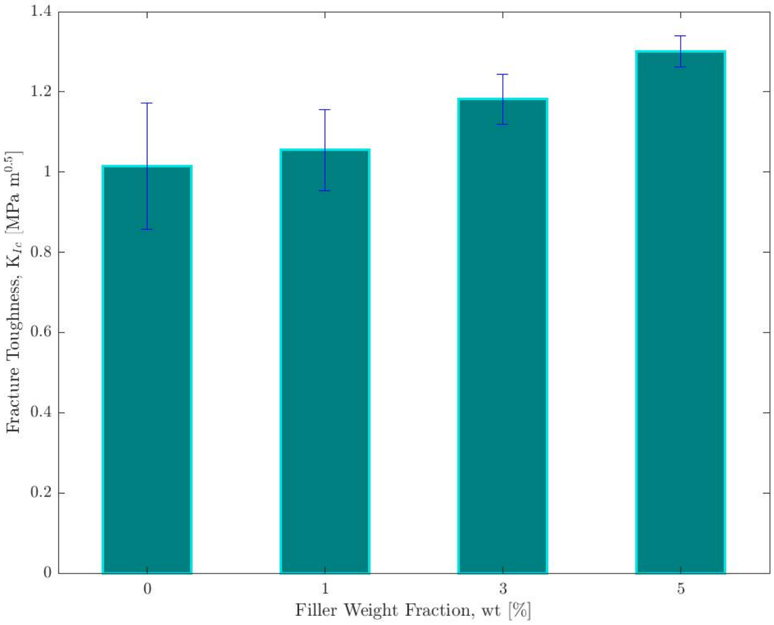

Figure 48 Mica10 fracture toughness.

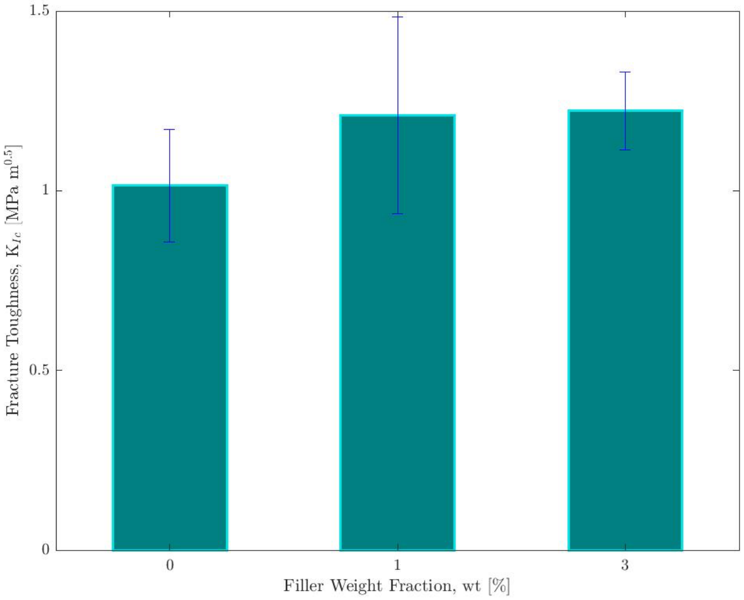

Figure 49 Mica45 fracture toughness.

Both results are good, since they show an increasing in the K_{Ic}, but the mica10 tests are particularly promising, showing a quasi-exponential increasing trend in the performance. For this reason, in the near future, we will try to repeat the test with greater charges to see if this already good performances improve even more. The last result obtained from the tests, is the critical energy release rate, G_{Ic}. In this test, aside the mica10 1%, where the values are almost equal to the neat epoxy test (slightly lower), to a bigger presence of the filler follow an increasing of the property, confirming the K_{Ic} trends.

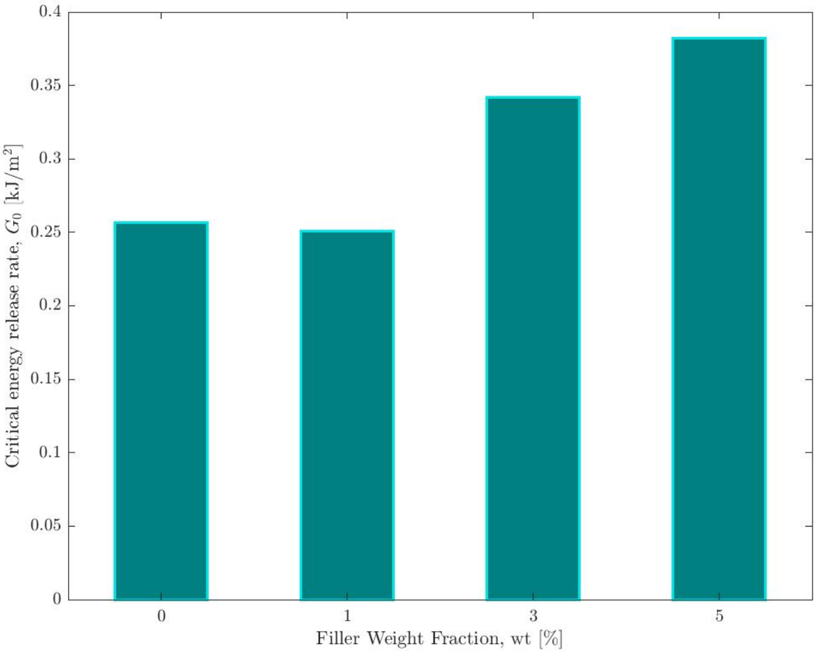

Figure 50 Mica10 critical energy release rate.

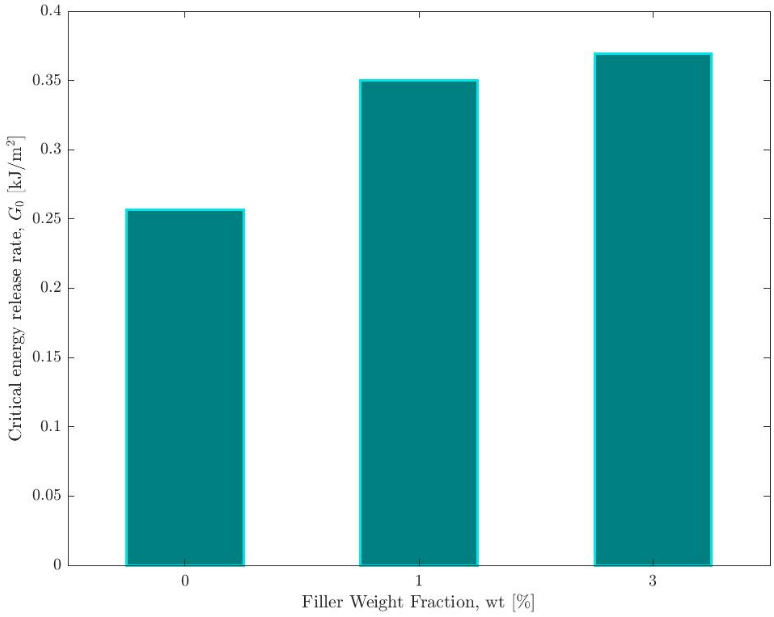

Figure 51 Mica45 critical energy release rate.

The results are collected in the table 10 below, for the value of K_{Ic} , we have also calculated the data covariance and the standard deviation.

Table 11 Fracture test main results.

Specimen	$Average\ K_{Ic}$	K_{Ic} Covariance	K_{Ic} Standard dev	G_{Ic}
Neat epoxy	1.0147	15.4095	0.1564	0.2564
Mica10 1%	1.0553	9.5740	0.1010	0.2506
Mica10 3%	1.1818	5.2807	0.0624	0.3419
Mica10 5%	1.3009	3.0281	0.0394	0.3824
Mica45 1%	1.2101	22.6378	0.2739	0.3503
Mica45 3%	1.2224	8.8931	0.1087	0.3696

Chapter 4

Polymer clay nanocomposite in everyday life and future prospects

As we anticipated polymer clay nanocomposites are studied in a large variety of fields, we can sum up the most important and promising in this paragraph.

Packaging - The packaging industry is probably the most interested industrial sector in the barrier properties of nanoclay-reinforced polymers and to be honest, our studies on micas started on the future prospects of developing a film intended for packaging. The resistance of these materials to water vapor, gases such as nitrogen, oxygen, and carbon dioxide, and aromatic compounds, together with the mechanical properties and the significant thermal resistance, instantly caught the packaging industry attention, also because of the possibility to replace material not so "green" that till now have been unreplaceable. Neat polymers are usually impermeable and harmful to the environment. High-barrier polyamide nanoclay, manufactured by Mitsubishi and Nanocor with the trade name Imperm® is designed to be utilized in the production of multilayer bottles and multilayer films with PET, PA, and PP, and has an extraordinarily low oxygen transfer rate. It has been fully approved for multilayer applications for all types of foods under FDA (the food and drugs administration) Another great example of this nanocomposites is represented by nano seal, developed by NanoPack Inc. which is a water-based coat consisting of nano-vermiculite polyvinyl alcohol nanocomposites approved for indirect food contact for the use with dry and moderately dry food packaging applications.

Automotive – Like every other industrial sector, nowadays one of the drivers for the development of new products and technologies is the environmental sustainability. Polymer-clay nanocomposites in the automotive industry, with their low costs and high sustainability and performance, are interesting candidates to replace many materials employed in the this sector. The first example in this area has already been mentioned: The 1990s timing-belt cover made by integrated organo-modified nanoclay in polyamide-nylon 6 developed by Toyota Motors. The timing belt is a part of a classic combustion engine which control the timing of the engine's valves. This component performed better than the originals, made by common plastic, thanks to its good stiffness, excellent heat stability and lack of wrapping, also reducing the vehicle weight. Mitsubishi adopted nylon 6 nanocomposites engine covers made by Unitika Co. for their GDI engines in the same years Toyota introduced its timing belt (Panchuck, M. 2020).

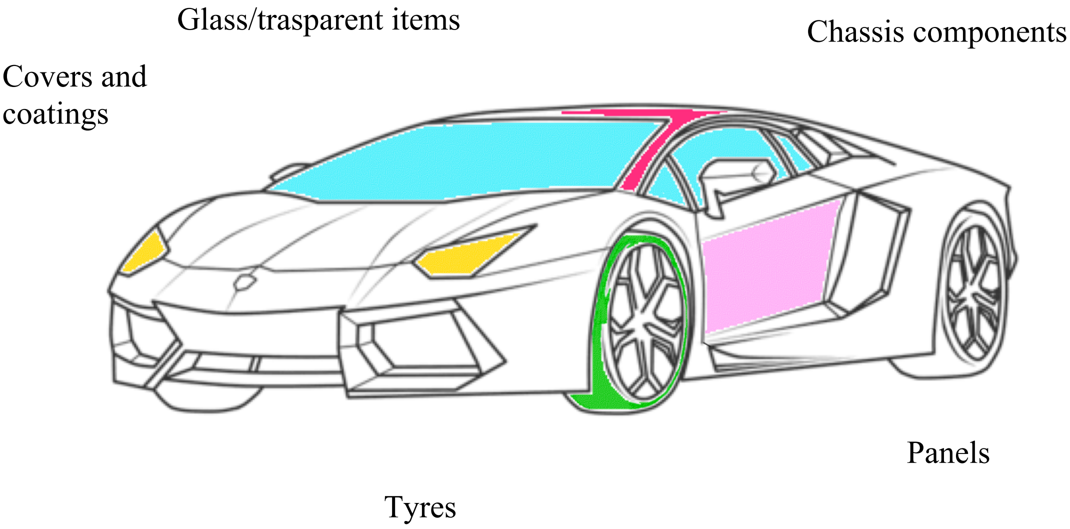

Figure 52 Car polymer clay nanocomposite's application.

Also some external parts of vehicles have been manufactured with polymer clay nanocomposites. GM and its partners Basell, Southern Clay Products, and Blackhawk Automotive Plastics introduced thermoplastic olefin (TPO) combined with nanoclay, that with just the 2.5% weight percent of nanoclay, was lighter but as rigid as the vehicle parts filled with 10 times the quantity of standard unmodified clay (Gul, S. 2016). Pirelli Tire announced in 2007 the use of a base compound containing polymer clay nanocomposites in P Zero tires designed for high and ultrahigh performances. Higher stiffness, better handling/comfort trade-off, no decay, and dynamic modulus stability with temperature were claimed. Compared to aramid reinforced fibers, the new ones showed better isotropic behavior and better ultimate properties in lateral and longitudinal directions. in 2009 Molded Fiber Glass Companies (MFG, Ashtabula, Ohio) developed Nano-filled sheet molding compounds (SMC) where modified nanoclay was added to thermoset resin to build the Chevrolet Corvette Z06 and Pontiac Solace rear floor. In the drawing above (Figure 43) we can take a look at some of the automotive component where polymer–clay nanocomposites are utilized or are being studied for a future use (Galimberti, M. 2013).

Flame Retardant materials - In recent years, polymer/layered silicate nanocomposites have attracted great attentions since they show significant improvement in decreasing the flammability. Polymer clay nanocomposites has already been used in flame retardant application in a great variety of fields, such as the textile and aerospace industry (Sanchez-Olivares, G. 2014) in the making of upholstery material. Also, the electronic industry gain advantages from this property of clay nanocomposites, to produce fire resistant wires and cables through the employment of nanoclay mixed halogenated or non-halogenated flame retardants (Cogen, J.M.). The interior footwell heater vent and center console in some Volkswagen and Chevrolet cars, are made of epoxy-clay laminates for their flame retardant properties.

Tissue engeneering and drug delivery - Polymer–clay nanocomposites are also finding place in the biomedical sector where they may help replacing tissues or even organs. The ability to cross the stomach and the intestine and the ability of absorbing a variety of toxins instantly, made think to a possible employement in tissue engeneering. Nanoclay can't be absorbed by the digestive system and in many cases can be dissolved by the gastric acids (Zhu, J.2001). Despite this, the medical field is one of the most delicate, and so, the implementation of clay nanocomposite still requires research. One of the most promising studies aim to use MMT modified 5-aminovaleric acid as material for replacing bone tissue (Ambre, A.H. 2010). As pore geometry, pore membrane morphology and connection between pores of nanostructured materials are critical for growth, cell implantation, emigration, mass transit, and tissue formation, these materials have been proven to be useful for these applications (Ma, P.X. 2004). Nanoclay-reinforced polymers are also used in drug delivery systems, which is a major medical application. With "drug delivery" we intend a technique that provide the construction of nano-structures, such as capsules, with which transport substance (drugs), and releasing them with extreme accuracy, passing through cell membranes. The high biocompatibility and low toxicity of nanoclays, make them an ideal material for this application, by the way nanoclay's toxicity is a critical aspect to study, since many studies shown that high doses cause the cellular death (Choy, J.H. 2007).

The design of a drug delivery system includes loading a specific concentration of medication into a specified delivery system and releasing the medicine at the desired pace to the target site. Many efforts have been made to manage the distribution and release of medicine for Alzheimer's disease by adsorption or intercalation of medicines in montmorillonite clay (Yang, J 2001)). Nanoclay are also being studied for other application in the biomedical field, such as additive, lubricants and other active materials in pharmaceutical formulation.

Footwear – nanoclay reinforced TPU has been tested for shoe soles to influence the friction and wear characteristics. Different nanoclays, modificated with different organic components, such as octadecyl ammonium and bis(2-hydroxyethyl) alloylmethylammonium), were tested at about 5 mass%. In the tests were observed a lower friction coefficient and higher resistance to wear (Sorrentino, A. 2007).

Other Applications – Another application where polymer nanoclay composites materials are employed is water treatment. The effective cation exchange process, stability, high aspect ratio, high fluctuation, adsorption ability are incredibly interesting characteristics useful to purify water (Guo, F. 2018). Several nanoclay composites have been developed for the removal of different pollutants from hydrous solutions and they have been demonstrated to be beneficial in the removal of both organic and inorganic pollutants (Kara, A.2016).

These nanocomposites are also used in Lithium-ion batteries. Self-supported polymer gel electrolytes (PGEs) based on polymer clay nanocomposite, vinylidene fluoride with up to 4 wt.% loading of the modified clay, has been developed, and their electrochemical properties in lithium-ion batteries are being investigated (Prasanth, R. 2013). Young Min Jeon et al. fabricated a UV-crosslinked electrolyte made from a polymer clay nanocomposite made of ethoxylated trimethylolpropane triacrylate solvated polyvinyl-dene fluoride-co-hexafluoropropylene (ETPTA/PVDF–HFP) as a matrix and Cloisite20A (modified nanoclay). The presence of this modified nanoclay enhance the ionic conductivity, significantly increasing the number of lithium cations, leading to better performance of the battery both during charge and discharge (Jeon, Y.M. 2020).

Conclusions

polymer clay nanocomposites are for sure one of the most interesting materials for many applications but much more work is required to solve some critical aspects. The lack of knowledge on nanofiller mechanical performances, since performing mechanical tests on nanomaterials is still impossible, is one of the main reasons which prevents their spread, but through modelling and simulation, with the huge computing power improvements of our processors, it's just a matter of time for having some good results. Much work must be done to characterize the properties of the interphase region, which features and mechanism, are still cloudy. The process of nanoclays dispersion into epoxy matrix, as we have seen in the workshop, is a critical aspect as a fully exfoliated morphology is quite difficult to obtain in a polymeric matrix. We have seen in this last chapter that nanocomposites with their superior mechanical, thermal, barrier, and flame-retardant properties, compared with micro or classical composites are suitable to be applicated in various industrial sectors, , by the way it's not easy to replace materials that we know from centuries, and whose manufacturing technology and every other aspect has no more secret, with a relatively completely new conception of material, in which some properties are still a mystery.

With regards the test with our micas nanocomposites, the result obtained have followed the expectation in many aspects: the elastic modulus moderately grew with the filler percentage, till the maximum percentage of filler employed. The tensile strength data were the worst result, because the values decrease with the presence of mica, even if only by a little. The fracture test gave us extremely good results, showing a continuous improvement of both Kic and Go, suggesting us that we could improve the results even more with a higher percentage of filler, in particular with mica10. Another great result has been the extraordinary transparency of the specimens, an aspect that increases the possible applications of this material, such as the possibility to use it in the production of transparent films or boxes useful for packaging.

Literature and sitography

A comprehensive review on analysis of nanocomposites: from manufacturing to properties characterization, M. Vinyas *et al.* 2019.

Analyzing the influence of particle size and stiffness state of the nanofiller on the mechanical properties of epoxy/clay nanocomposites using a novel shear-stiff nano-mica Martin Heinz Kothmann, Mazen Ziadeh, Go¨khan Bakis, Agustin Rios de Anda, Josef Breu, Volker Altsta¨dt. May 2015.

An insight into mechanical properties of polymer nanocomposites reinforced with multidimensional filler system: A state of art review, Nitesh Dhar Badgayan, Santosh Kumar Sahu, Sutanu Samanta¸ Rama Sreekanth P S, 2018.

An Investigation of Mechanical and Thermal Properties of Polypropylene Clay Nanocomposites Containing Different Nanoclays, Sundaresan Arunachalam, Markus Gottfried Battisti, Chinnaswamy Thangavel Vijayakumar, Walter Friesenbichler Macromol, 2015.

An Investigative Study on the Progress of Nanoclay-Reinforced Polymers: Preparation, Properties, and Applications: A Review. *Polymers* 2021, Abulyazied,D.E.Ene,A.

An overview of multifunctional epoxy nanocomposites, Hongbo Gu, Chao Ma, Junwei Gu, Jiang Guo, Xingru Yan, Jiangnan Huang, Qiuyu Zhang and Zhanhu Guo 12th May 2016.

A review on polymer–layered silicate nanocomposites S. Pavlidou, C.D. Papaspyrides, 25 July 2008.

ASTM Designation: D638 – 14, Standard Test Method for Tensile Properties of Plastics.

ASTM Designation: D5045 – 14, Standard Test Methods for Plane-Strain Fracture Toughness and Strain Energy Release Rate of Plastic Materials.

A technical review on epoxy-clay nanocomposites: Structure, properties, and their applications in fiber reinforced composites, Omid Zabihi, Mojtaba Ahmadi, Saeid Nikafshar, Karthik Chandrakumar Preyeswary, Minoo Naebe, 27 September 2017.

Effect of clay minerals structure on the polymer flame retardancy intumescent process, Simone Pereira da Silva Ribeiro, Leonardo dos Santos Cescon, Rodrigo Quilelli Correa Rocha Ribeiro, Alexandre Landesmann, Luciana Rocha de Moura Estevão, Regina Sandra Veiga Nascimento.

Effect of filler particle shape on plastic-elastic mechanical behavior of high-density poly(ethylene)/mica and poly(ethylene)/wollastonite composites, Lubomír LapčíkDavid

Maňas, Barbora Lapčíková, Martin Vašina, Michal Staněk, Klára Čépe, Jakub Vlček, Kristian E. Waters, Richard W. Greenwood, Neil A. Rowson.

Electrical Insulation Properties of Nanocomposite Epoxy Resin and Application to Mica Insulation, Takahiro Mabuchi, Yin Xiaohong, Advanced Technology R&D Center, Mitsubishi Electric Corporation Amagasaki, Hyogo, JAPAN, 2020.

Epoxy Nanocomposites with Highly Exfoliated Clay: Mechanical Properties and Fracture Mechanisms.

Epoxy layered-silicate nanocomposites, Chenggang Chen, Mohammad Khobaib, David Curliss.

Experimental Characterization and Modeling Stiffness of Polymer/Clay Nanocomposites within a Hierarchical Multiscale Framework, A. Mesbah, F. Za¨ıri, S. Boutaleb, J. M. Gloaguen, M. Na¨ıt-Abdelaziz, S. Xie, T. Boukharouba, J. M. Lefebvre, 5 April 2009.

Fabrication and PD-initiated Breakdown of Simulated Mica Tape Insulation Containing Epoxy Nanocomposites, Tomonori Iizuka, Xuping Liu, Jun Mai, Kohei Tatsumi, Toshikatsu Tanaka, Takahiro Mabuchi, Xiaohong Yin, Takahiro Umemoto and Hirotaka Muto.

Few-Layer Clayenes for Material and Environmental Applications, Wenyan Huang, Sridhar Komarneni, Christopher Gorski, Young Dong Noh, April Doroski, Yan Dong, Jianfeng Ma, Aron M. Griffin, Dongjiang Yang, Xiaoqiang Xue, Hongjun Yang, and Bibiao Jiang, February 7, 2020.

Force-Induced Self-Assembly of Supramolecular Modified Mica Nanosheets for Ductile and Heat-Resistant Mica Papers, Hongkun Jiang, Lei Jiang, Peng Zhang, Xinyue Zhang, Ning Ma, and Hao Wei, April 21, 2021.

Handbook of Polymer Testing Book, Zainab Raheem, July 2019.

Introduction to Fourier Transform Infrared Spectrometry, Thermo Nicolet corporation 2001.

Investigation of advanced mica powder nanocomposite filler materials: Surface energy analysis, powder rheology and sound absorption performance, Lubomír Lapcík, Martin Vasina, Barbora Lapcíkova, Eva Otyepkova, Kristian Edmund Waters.

Mechanical and Rheological Studies on Polyethylene Terephthalate-Montmorillonite Nanocomposites, A. Sanchez-Solis, I. Romero-Ibarra, M.R. Estrada, F. Calderas, O. manero, June 2004.

Mechanical Properties of Nanoclay and Nanoclay Reinforced Polymers: A Review Roham Rafiee, Reza Shahzadi, 10 January 2018.

Mechanical behaviour of epoxy/silica nanocomposites: Experiments and modelling, M. Zappalorto, A. Pontefisso, A. Fabrizi, M. Quaresimin, 27 January 2015.

Mica-Based Multilayer Nanocoating as a Highly Effective Flame Retardant and Smoke Suppressant, Abbas Fahami, Jungyu Lee, Simone Lazar, and Jaime C. Grunlan, December 2020.

Multifunctional Cu^{21}-montmorillonite/epoxy resin nanocomposites with antibacterial activity, Alessandra Bartolozzi, Roberta Bertani, Elisa Burigo, Alberto Fabrizi, Francesco Panozzo, Marino Quaresimin, Fabio Simionato, Paolo Sgarbossa, Sergio Tamburini, Michele Zappalorto, Federico Zorzi.21 November 2016.

Multifunctional nanocomposites with enhanced mechanical and anti-microbial properties, R.Bertani, M.Quaresimin, M.Zappalorto, A.Pontefisso, F.Simionato, A.Bartolozzi 22-26 June 2014.

Multifunctional Epoxy/Nanocomposites Based on Natural Moroccan Clays with High Antimicrobial Activity: Morphological, Thermal and Mechanical Properties, M. Monsif, A. Zerouale, N. Idrissi Kandri, R. Bertani, A. Bartolozzi, B. M. Bresolin, F. Zorzi, F. Tateo, M. Zappalorto, M. Quaresimin, and P. Sgarbossa Published, 22 November 2019.

Nacreous aramid-mica bulk materials with excellent mechanical properties and environmental stability, Xiao-Feng Pan, Huai-Ling Gao, Kai-Jin Wu, Si-Ming Chen, Tao He, Yang Lu, Yong Ni, and Shu-Hong Yu, January 22, 2021.

Polymer and ceramic nanocomposites for aerospace applications Vivek T. Rathod, Jayanth S. Kumar, Anjana Jain, 29 August 2017.

Polymer Nanocomposites for Aerospace Applications: Characterization by James Njuguna and Krzysztof Pielichowski, 2004.

Polymer-clay Nanocomposites, Preparations and Current Applications: A Review Farman Ali, Hayat Ullah, Zarshad Ali, Fazal Rahim, Fahad Khan and Zia Ur Rehman, May 17, 2016.

Polymer nanotechnology: Nanocomposites, D.R. Paul, L.M. Robeson, 4 April 2008.

Polystyrene-Based Composites with Aluminosilicate Inclusions of Different Shapes O. A. Moskalyuk, I. V. Semenova, V. E. Yudin, Y. M. Beltukov, N. N. Saprykina, and V. Yu. Elokhovskii, June 14, 2018.

Preparation and Characterization of PAEK based Polymer Nanocomposites in the Presence of MMT Clay as Nanofiller to Study Tensile and Impact Properties, Rinul M. Dhajekar, Bhagwan F. Jogi and Shripad R. Nirantar, May 2018.

Preparation, morphology and thermal/mechanical properties of epoxy/nanoclay composite, Lei Wang, Ke Wang, Ling Chen, Yongwei Zhang, Chaobin, 30 December 2005.

Principali prove meccaniche su materiali polimerici R. Pantani. [ppt]

Processing of Mica/Epoxy Nanocomposites by Ultrasound Mixing, Amar Boukerrou, Jannick Duchet, Said Fellahi, Henry Sautereau, 17 January 2007.

Process-structure-property relationship in polymer nanocomposites, Amir Asadi, Kyriaki Kalaitzidou, 2018.

Properties of polyethylene-layered silicate nanocomposites prepared by melt intercalation with a PP-g-MA compatibilizer, Joong-Hee Lee, Daeseung Jung, Chang-Eui Hong, Kyong Y. Rhee, Suresh G. Advani, 17 March 2005.

Review on polymer nanocomposite for ballistic & aerospace applications Vidya, Laxman Mandal, Balram Verma, Piyush K. Patel, 14 february 2020.

Synthesis and characterization of novel polymer/clay nanocomposites based on poly (butylene 2,5-furan dicarboxylate), Lazaros Papadopoulos, Zoi Terzopoulou, Antonios Vlachopoulos, Panagiotis A. Klonos, Apostolos Kyritsis, Dimitrios Tzetzis, George Z. Papageorgiou, Dimitrios Bikiaris, 23 March 2020.

Strain-stress curves, David Roylance, August 23, 2001.

Study of Morphological and Mechanical Performance of Amine-Cured Glassy Epoxy–Clay Nanocomposites, A. Mouloud, R. Cherif, S. Fellahi, Y. Grohens, I. Pillin 22 August 2011.

Tensile, dielectric, and thermal properties of epoxy composites filled with silica, mica, and calcium carbonate, C. L. Poh, M. Mariatti, M. N. Ahmad Fauzi, C.H.Ng, C.K.Chee, T.P.Chuah. 23 January 2014.

Tensile properties of nanosilica/epoxy nanocomposites Aidah Jumahat, Costas Soutis, Shahrul Azam Abdullah, Salmiah Kasolang, International Symposium on Robotics and Intelligent Sensors 2012.

Tensile testing of epoxy-based thermoset system prepared by different methods Ankur Bajpai, Bernd Wetzel, 10 july 2019.

The Basics of Testing Plastics: Mechanical Properties, Flame Exposure, and General Guidelines Stephen Burke Driscoll, October 2004.

The influence of the interface between mica and epoxy matrix on properties of epoxy-based dielectric materials with high thermal conductivity and low dielectric loss, Hailin Mo, Genlin Wang, Fei Liu and Pingkai Jiang, 23rd June 2016.

Thermogravimetric Analysis of Polymers H.M. Ng Norshahirah mohamad saidi Rameshkasi Kasi Ramesh T Subramaniam, November 2018.

The use of environmental scanning electron microscopy for imaging wet and insulating materials, athene m. donald Cavendish Laboratory, University of Cambridge, Madingley Road, Cambridge, UK. nature materials, vol.2, august 2003.

https://www.britannica.com/science/mica

https://serc.carleton.edu/research_education/geochemsheets/techniques/SEM.html

https://serc.carleton.edu/research_education/geochemsheets/techniques/XRD.html

https://www.intechopen.com/chapters/62742